Department of Physics and Astronomy

Heidelberg University

Master thesis

in Physics

submitted by

Paul Hill

born in Koblenz

2021

Towards Physics of the Fractional Quantum Hall Effect in Rotating Few-Fermion Systems

This Master thesis has been carried out by Paul Hill

at the

Physikalisches Institut Heidelberg

under the supervision of

Prof. Selim Jochim

Zusammenfassung:
Kalte Atome bieten eine einzigartige Möglichkeit Vielteilchen-Quantensystem verschiedenster Art im Labor zu simulieren und zu untersuchen. Insbesondere im Regime kleiner, zweidimensionaler Systeme weniger Teilchen erlaubt die wiederholte Messung der Position der verschiedenen Teilchen einen Zugang zu der vollen Vielkörper-Wellenfunktion des präparierten Quantenzustands. Die experimentelle Simulation solcher Systeme ist vor allem auch deswegen interessant, da eine theoretische Beschreibung häufig nur sehr schwer möglich ist. Auf der einen Seite enthalten sie zu viele Teilchen, als mit herkömmlichen numerischen oder gar analytischen Methoden zu erfassen wäre, auf der anderen Seite sind sie aber zu klein, um eine statistische Beschreibung im thermodynamischen Limes zu ermöglichen. Der erste Teil dieser Arbeit befasst sich daher mit neuen numerischen Methoden in dem Versuch, mit der Entwicklung derzeitiger Experimente Schritt zu halten. Im Gegensatz dazu befasst sich der zweite Teil mit der experimentellen Umsetzung eines erst kürzlich vorgeschlagenen experimentellen Protokolls zur Erzeugung stark korrelierter Zustände des fraktionellen Quantenhalleffekts. Diese Zustände zeichnen sich durch einen hohen Gesamtdrehimpuls aus. Zu deren Präperation soll der dazu notwendige Drehimpuls durch den Einsatz rotierender optischer Fallen in das System transferiert werden. Der Aufbau der benötigten optischen Instrumente und auch die Fortführung der bestehenden numerischen Arbeit hin zu einer Beschreibung des Systems unter realistischen experimentellen Bedingungen sind Hauptbestandteil des zweiten Teils dieser Arbeit.

Abstract:
Cold atoms provide an exciting opportunity to simulate and investigate various many-body quantum systems in the laboratory. Especially in the regime of small, two-dimensional systems of small particle number the repeated measurement of the position of the different particles provides access to the full many-body wavefunction of the prepared quantum state. The experimental simulation of such systems is especially interesting, since a theoretical description is often times very hard to achieve. On the one hand they contain too many particles for conventional numerical or even analytical methods to handle, on the other hand they are too small to allow for a statistical description in the thermodynamic limit. In the first part of this thesis new numerical methods are explored trying to keep up with advances of current experiments.
On the contrary, the second part deals with the experimental realization of a recently proposed experimental protocol for the creation of strongly correlated states of the fractional quantum Hall effect. These states are characterized by a high total angular momentum. For their preparation the necessary angular momentum will be transferred into the system by using rotating optical traps. Setting up the needed optical devices and continuing the existing numerical work, in order to describe the system under realistic experimental condition will be the major subject of the second part of this thesis.

Contents

1 Introduction **8**

2 Fundamental Physics of Ultracold Atoms **10**
2.1 Scattering Theory . . . 10
2.1.1 Partial-wave analysis . . . 12
2.1.2 Low energy scattering . . . 13
2.1.3 Pseudopotentials . . . 14
2.1.4 Scattering of identical particles . . . 15
2.2 Interacting particles in a harmonic trap . . . 16
2.3 Properties of ^{6}Li . . . 18
2.3.1 The Feshbach-resonance of ^{6}Li . . . 20
2.4 Preparing an ultracold Fermi gas . . . 21

3 Numerical Study of interacting atoms in a 2D-trap **24**
3.1 Renormalization of the coupling constant for the two particle-problem 24
3.2 The Hamiltonian in second quantization . . . 29
3.3 Quanty - a many body code . . . 30
3.4 The two-particle problem revisited . . . 31
3.5 Precursor of the Higgs Mode . . . 33

4 Rotating Traps: A path to Quantum Hall Physics **35**
4.1 The Quantum Hall Effect in a nutshell . . . 35
4.2 The Rotating Harmonic Trap . . . 37
4.2.1 Perturbations: Opening an adiabatic path to the LLL . . . 40
4.2.2 Switching on Interactions: Renormalization in the Lowest Landau Level . . . 41
4.2.3 Fractional Quantum Hall States . . . 43
4.2.4 Detection . . . 48
4.3 The Rotating Gaussian Trap and other experimental caveats . . . 49
4.3.1 Realistic Traps using Laguerre-Gaussian Laser Beams . . . 49
4.3.2 Exact single-particle spectrum . . . 52
4.3.3 How deep is deep enough? . . . 55
4.3.4 Adiabatic Passage in the Gaussian Trap . . . 57
4.4 Implementation and Experimental Methods . . . 61
4.4.1 Optical Design: Lenses and Aberrations . . . 61
4.4.2 The Spatial Light Modulator . . . 69
4.4.3 Optical Setup . . . 79

5 Conclusion and Outlook **86**

A Additional Figures **89**

B Bibliography **91**

1 Introduction

With the realization of the first Bose-Einstein condensates in vapors of bosonic rubidium and sodium atoms in 1995[Anderson et al., 1995][Davis et al., 1995], interest in the field of ultracold atoms has grown explosively. In the following years substantial effort was made to push the investigated systems beyond mean field physics in the hope to find signals of strong interactions and correlations. A further milestone on this rode was achieved in 1999 with the first demonstration of Fermi degeneracy[DeMarco and Jin, 1999]. Both fermionic and bosonic gases soon proved to be highly tunable and clean systems capable of providing an excellent environment for the simulation of several important models from many-body physics. Since their early days ultracold atoms hence have been used to address physics of strongly correlated matter. Prominent success stories are for example the observation of the BEC-BCS crossover [Regal et al., 2004][Zwierlein et al., 2004] which can be used to describe high temperature superconductors [Leggett, 1980][Nozières and Schmitt-Rink, 1985] and the simulation of important models like the Hubbard, Heisenberg and Haldane model by means of an optically created periodic potential landscape.
While early experiments were limited to run with a large number of particles recent experimental advances now allow for the deterministic preparation of small systems down to single atoms. Accompanied with the development of new tools to resolve the atomic cloud on a single particle level, this opened up the path to investigate many-body phenomena outside of the thermodynamic limit. Such mesoscopic systems pose an inherent challenge to our current understanding being too large to be exactly solvable and yet to small to be describable on the mean field level. In very recent experimental work precursors of typical many-body phenomena like quantum phase transitions [Bayha et al., 2020] and cooper pairing [Holten et al., 2021a] could be observed in surprisingly small systems of 6 to 12 particles. Exploring new numerical tools [Haverkort et al., 2012] to keep up with these recent experimental advances will be the first part of this thesis.
Besides investigating the transition from few- to many-body physics, systems of small particle number promise to be an excellent platform for the realization of fractional quantum Hall states. In contrast to experiments conducted in semiconductors, where the fractional quantum Hall effect originally appears, which are often times limited to the study of bulk properties, ultracold atoms offer the exciting opportunity to probe the states locally, thereby accessing particle correlations directly. A number of quantum gas experiments were already performed with the purpose of preparing a fractional quantum Hall state and probing its correlations [Schweikhard et al., 2004][Zwierlein et al., 2005][Gemelke et al., 2010]. However, so far quantum Hall physics could only be accessed in a mean field regime. Interestingly, the problem

was mostly one of size and it is argued that clear signals of the fractional quantum Hall effect are only observable in systems of few particles. A novel approach to this problem was explored in [Palm, 2018], investigates the realization of fractional quantum Hall states with filling fraction $\nu \leq 1$ in a system of a few ^{6}Li atoms. By using a single optical rotating microtrap a target fractional quantum Hall state is prepared deterministically. Subsequently releasing the atoms from the trap and imaging them after a time of flight [Bergschneider et al., 2018] gives access the modulus of the full few-body wavefunction from which correlations can be extracted. The second and mayor part of this thesis will be devoted to following up on this proposal. Besides implementing the optical setup in our current experiment an additional effort is made to numerically study the system under realistic experimental conditions.

Outline

This thesis will be outlined as follows. In chapter 2 we will discuss some of the physical fundamentals about ultracold atoms in general and ^{6}Li in particular. We will then turn towards the theoretical description of our current experimental system consisting of interacting atoms in a two-dimensional trap in chapter 3. Here also the numerical approach used throughout this thesis will be introduced. After testing this approach in a system with known analytical solution we will consider the recent experimental observation of the precursor of a quantum phase transition for which the excitation spectrum will be computed.
A mayor part of this thesis will be devoted to chapter 4 which deals with the implementation of the rotating trap proposal aiming at the observation of fractional quantum Hall states. Finally, we conclude in chapter 5.

2 Fundamental Physics of Ultracold Atoms

In this chapter we want to familiarize ourselves with the most important ingredients and concepts needed to understand the physics of small mesoscopic systems of ultracold atoms. Throughout this thesis a major focus will be put on the interactions between the atoms and hence we will devote a substantial part of this chapter to the discussion of scattering theory and the s-wave interactions emerging at ultracold temperatures. Typically for systems of small particle number the level spacing of the trapping potential poses a relevant energy scale with respect to the comparatively low Fermi-energy. As a consequence it is the interplay of interactions and the level spacing in the trap that determines much of the ongoing physics. We quickly touch this subject discussing two interacting particles in a harmonic trap where we will also see how a quasi two-dimensional regime can be realized by a harmonic trap that is considerably tighter in one dimension. Finally, we will discuss the properties of ^{6}Li, the atom of choice, especially focusing on its Feshbach resonance and how systems of few ^{6}Li-atoms can be prepared deterministically.

2.1 Scattering Theory

We begin with a discussion of scattering theory starting on very general grounds. To this end let us investigate the Schrödinger equation of one particle interacting with a potential $\hat{V}$

$$E\,|\psi\rangle = (\hat{H}_0 + \hat{V})\,|\psi\rangle\,, \tag{2.1}$$

where $\hat{H}_0 = \frac{\hat{p}^2}{2\mu}$ is the Hamiltonian of the free particle with mass μ. Seeking scattering, i.e. unbound, states we restrict ourselves to solutions with $E > 0$ (assuming that $V(r) \to 0, r \to \infty$). Given a Green's operator $\hat{G}_0(E)$ fulfilling

$$(E - \hat{H}_0)\hat{G}_0(E) = \mathbb{1} \tag{2.2}$$

we get a formal solution to eq. (2.1) by

$$|\psi\rangle = |\psi_0\rangle + \hat{G}_0(E)\hat{V}\,|\psi\rangle\,, \tag{2.3}$$

where $|\psi_0\rangle$ is any solution to the free problem ($\hat{V} = 0$). Since we expect to recover the free solution $|\boldsymbol{k}\rangle$ in the limit $\hat{V} \to 0$, we choose $|\psi_0\rangle = |\boldsymbol{k}\rangle$ with $E = \frac{\hbar^2 k^2}{2\mu}$, leaving us with a whole family of solutions $|\psi_{\boldsymbol{k}}\rangle$.

To proceed we need to solve eq. (2.2) which is most conveniently done in k-space. Introducing small $i\epsilon$-terms to avoid poles on the real line yields several possible solutions depending on the location of the shifted poles. Most importantly one finds

$$\hat{G}_0^{\pm}(k) = \frac{2\mu}{\hbar^2}\int \frac{d^dq}{(2\pi)^d}\frac{|\boldsymbol{q}\rangle\langle\boldsymbol{q}|}{k^2-q^2\pm i\epsilon} = \frac{1}{E-\hat{H}_0\pm i\epsilon}, \tag{2.4}$$

being termed the retarded ($^+$), advanced ($^-$) Greens operator, respectively [1]. With the $\hat{G}_0^{\pm}$ at hand we now obtain an expression for the scattering solutions (2.3), known as the famous Lippmann-Schwinger equation:

$$|\psi_{\boldsymbol{k}}\rangle^{\pm} = |\boldsymbol{k}\rangle + \frac{2\mu}{\hbar^2}\int \frac{d^dq}{(2\pi)^d}\frac{|\boldsymbol{q}\rangle T^{\pm}_{\boldsymbol{q},\boldsymbol{k}}}{k^2-q^2\pm i\epsilon}, \quad T^{\pm}_{\boldsymbol{q},\boldsymbol{k}} = \langle\boldsymbol{q}|\,\hat{V}\,|\psi_{\boldsymbol{k}}\rangle^{\pm}. \tag{2.5}$$

We may now choose a Green's function according to the boundary conditions we're interested in. As is discussed in Weinberg [2005][2], wavepackets formed with the scattering states $|\psi_{\boldsymbol{k}}\rangle^{\pm}$ (also termed in- and out-states) evolve like free wavepackets in the distant past or future, respectively, i.e.

$$e^{-i\hat{H}t}\int g(\boldsymbol{k})\,|\psi_{\boldsymbol{k}}\rangle^{\pm} \xrightarrow{t\to\mp\infty} e^{-i\hat{H}_0t}\int g(\boldsymbol{k})\,|\boldsymbol{k}\rangle\,.$$

Because we are interested in the scattering of an incoming particle off the potential, we naturally choose the retarded solution. Nevertheless, the advanced solution is of importance as it allows for a convenient definition of the S-matrix, $S_{\boldsymbol{k}',\boldsymbol{k}} = {}^{-}\langle\psi_{\boldsymbol{k}'}|\psi_{\boldsymbol{k}}\rangle^{+}$, connecting the theory to experimental observables like the cross section.

Let us now proceed by going to position-space, making the above statements more explicit. Expressing the Lippmann-Schwinger equation on a basis of position eigenstates $|\boldsymbol{x}\rangle$, where $\langle\boldsymbol{x}|\boldsymbol{k}\rangle = e^{i\boldsymbol{k}\cdot\boldsymbol{x}}$, yields

$$\psi^{\pm}_{\boldsymbol{k}}(\boldsymbol{x}) = e^{i\boldsymbol{k}\cdot\boldsymbol{x}} + \frac{2\mu}{\hbar^2}\int d^dy\mathcal{G}^{\pm}_k(|\boldsymbol{x}-\boldsymbol{y}|)V(\boldsymbol{y})\psi^{\pm}_{\boldsymbol{k}}(\boldsymbol{y}). \tag{2.6}$$

The Green's functions $\mathcal{G}^{\pm}_k(r)$ are obtained by evaluating the corresponding Green's operators in the position basis. We merely state the result for the interesting cases of two [Adhikari, 1986] and three dimensions

$$\mathcal{G}^{\pm}_{0,k}(r) \equiv \frac{\hbar^2}{2\mu}\langle\boldsymbol{x}|\hat{G}^{\pm}_0(k)|\boldsymbol{y}\rangle = \begin{cases} -\frac{i}{4}H^{\pm}_0(kr) & \text{in 2D} \\ -\frac{1}{4\pi r}e^{\pm ikr} & \text{in 3D} \end{cases}, \quad r = |\boldsymbol{x}-\boldsymbol{y}|. \tag{2.7}$$

Here $H^{\pm}_0$ are the Hankel-functions of the first and second kind, respectively.

In order to describe the scattering process, one usually just cares about the evolution

[1] The other possible solutions resulting from this procedure can be expressed in terms of the $\hat{G}^{\pm}_0$. Since they correspond to a stationary wave, they are not relevant for our current discussion.

[2] A less abstract discussion can be found in Bartelmann et al. [2014].

of the incoming wavepacket after the scattering event, when the particle has long left the interaction region. Thus, we finally state eq. (2.6) evaluated at large arguments

$$\psi_k^{\pm}(r,\theta) \xrightarrow{r\to\infty} \begin{cases} e^{ikx} + \sqrt{i/(kr)} f^{\pm}(k,\theta) e^{\pm ikr} & \text{in 2D} \\ e^{ikx} + f^{\pm}(k,\theta) e^{\pm ikr}/r & \text{in 3D} \end{cases}, \tag{2.8}$$

where without loss of generality we chose $\boldsymbol{k} \parallel \hat{\boldsymbol{e}}_x$ and $\theta = \measuredangle(\boldsymbol{x}, \hat{\boldsymbol{e}}_x)$. Furthermore, we introduced the scattering amplitude $f(k,\theta)$ given by

$$f^{\pm}(k,\theta) = -\frac{\mu}{\sqrt{2\pi}^{d-1}\hbar^2} \int d^d y \; e^{\mp i\boldsymbol{k'}\cdot\boldsymbol{y}} V(\boldsymbol{y}) \psi_k^{\pm}(\boldsymbol{y}) \sim T^{\pm}_{\boldsymbol{k'},\boldsymbol{k}}, \quad \boldsymbol{k'} = k\boldsymbol{x}/r. \tag{2.9}$$

We observe that for both the two and three dimensional case the scattering solution asymptotically looks like a superposition of an incoming plane wave and an outgoing or incoming spherical wave, depending on whether one chooses the retarded or advanced solution, respectively. The outgoing spherical wave can be interpreted as a scattered wave originating in the scattering center and describes the effect of the interaction with the potential as seen from a large distance. This fits our previous observation that the retarded solution corresponds to an incoming free particle scattering off the potential.
Finally, we note that the form of eq. (2.8) in two dimensions differs to the three dimensional case by a factor of $\sqrt{i/k}$. As pointed out by [Adhikari, 1986] this factor ensures the correct analytic properties of the scattering amplitude $f(k,\theta)$.

2.1.1 Partial-wave analysis

Throughout the rest of this thesis we will only deal with the important subclass of scattering potentials obeying rotational symmetry, i.e. $V = V(|\boldsymbol{x}|)$. In such cases it is convenient to expand the scattering solutions in terms of angular momentum eigenfunctions, simplifying the Schrödinger equation to an ODE for the radial coordinate.
Further assuming that V drops to zero sufficiently fast, we approximate $V(r) = 0, r \geq R$ for some large radius R. In that region the radial Schrödinger equation reduces to the well-known Bessel equation and we can immediately write down a general solution in terms of (spherical) Hankel functions of the first and second kind. The expansion of the scattering wavefunction for $r \geq R$ is then given by

$$\begin{aligned} &\text{(2D)} \quad \psi_k(r,\theta) = \sum_{m=0}^{\infty} i^m \frac{\epsilon_m}{2} \cos(m\theta) \left[H_m^-(kr) + e^{2i\delta_m} H_m^+(kr) \right] \\ &\text{(3D)} \quad \psi_k(r,\theta) = \sum_{l=0}^{\infty} i^l (2l+1) P_l(\cos\theta) \frac{1}{2} \left[h_l^-(kr) + e^{2i\delta_l} h_l^+(kr) \right]. \end{aligned} \tag{2.10}$$

Here h_l are the spherical Hankel functions, $P_l(x)$ are the Legendre-polynomials and $\epsilon_m = 2 - \delta_{m0}$. Further $l \in \mathbb{N}$ labels states with total angular momentum $L^2 =$

$\hbar^2 l(l+1)$ in three dimensions, while $m \in \mathbb{Z}$ labels the angular momentum eigenstates in two dimensions, i.e. with angular momentum $M = \hbar m$. Note that we already fixed the constants of integration such that the expansion eq. (2.10) matches the asymptotic form eq. (2.8) at large radii. The only remaining degrees of freedom are the so called scattering phases δ_l which are taken to be real in order to satisfy the conservation of probability (reflecting the coherence of the scattering process). The scattering phases depend on the energy as well as the concrete scattering potential V and are fixed via matching the expansion eq. (2.10) with the inner solution for $r < R$ at R.
The partial waves asymptotically behave like $\sim \cos(kr + \delta_l(k) + \text{const}_l)$. Hence, when viewed from a large distance, the effect of the interaction with the potential is either to pull the partial waves towards the center ($\delta > 0$) or to push them away ($\delta < 0$) as compared to the free evolution. We therefore call the interaction either attractive or repulsive.
Lastly, by again considering the asymptotic behavior of eq. (2.10), we can relate the scattering amplitude to the partial waves as

$$f(k,\theta) = \begin{cases} \sqrt{\frac{2}{\pi}} \sum_m \epsilon_m f_m(k) \cos m\theta, f_m = e^{i\delta_m(k)} \sin \delta_m(k) & \text{in 2D} \\ \sum_l (2l+1) f_l(k) P_l(\cos\theta), f_l = \frac{1}{k} e^{i\delta_l(k)} \sin \delta_l(k) & \text{in 3D} \end{cases} . \tag{2.11}$$

2.1.2 Low energy scattering

We have seen in eq. (2.9) that the scattering amplitude is directly given by the on-shell T-matrix, the analytic structure of which it therefore inherits. This allows one to derive a number of important theorems, most prominently the optical theorem. In the context of ultracold atoms the low-energy or effective range expansion of the scattering phases is of great interest as it allows to greatly simplify the theoretical description of the scattering process. For a large class of potentials it can be shown that the 3D scattering phases omit an analytic expansion $k^{2l+1} \cot \delta_l(k) = c_{l0} + c_{l1} k^2 + O(k^4)$, which allows us to write the 3D scattering amplitudes as [Joachain, 1975]

$$f_l(k) = \frac{1}{k \cot \delta_l(k) - ik} = \frac{k^{2l}}{c_{l0} + c_{l1} k^2 + O(k^4) - ik^{2l+1}}. \tag{2.12}$$

In the $k \to 0$ limit, which is the typical situation for ultracold atoms, only the $l = 0$ (or s-wave) channel can acquire a finite value. Since all other scattering amplitudes go to zero, the scattering becomes isotropic. This is the quantum analogue of the classical angular momentum blockade which prevents a particle with angular momentum to penetrate deeply into a central potential.
Defining the (s-wave) scattering length $a = -\frac{1}{c_{00}} = \lim_{k\to 0} -\frac{\tan \delta_0(k)}{k}$ and effective range $r_{\text{eff}} = 2c_{01}$, the scattering wavefunction takes on the following simple form

$$\psi_k(r,\theta) \approx e^{ikx} + \frac{-a}{1+ika} \frac{e^{ikr}}{r}, \quad r \geq R, \tag{2.13}$$

provided $|r_{\text{eff}}k| \ll 1$. Note that the scattering amplitude a can be either positive or negative depending on whether the potential is repulsive or attractive, respectively. A similar story holds in two dimensions where one finds [Randeria et al., 1990] $\cot\delta_0 = \frac{1}{\pi}\ln(E/E_a) + O(E/\epsilon_R)$, with $\epsilon_R = \frac{\hbar^2}{2\mu R^2}$. E_a is parameterizing the low energy scattering off a given potential and has units of energy. By introducing the 2D-scattering length as $E_a = \frac{\hbar^2}{2\mu a^2}$ one finds $\cot\delta_0 = \frac{2}{\pi}\ln(ka) + O(k^2/\epsilon_R)$. This matches the definition of Idziaszek and Calarco [2006] in which the authors relate the 2D-scattering length to the 3D case in the experimentally accessible quasi-2D regime in a harmonic trap. The scattering solution in two dimensions then becomes

$$\psi_k(r,\theta) \approx e^{ikx} + \frac{\pi i}{2\ln(ka) - i\pi} H_0^+(kr), \quad r \geq R. \tag{2.14}$$

Note that in contrary to its three dimensional counterpart the 2D-scattering length is always positive.

2.1.3 Pseudopotentials

We have seen that in the $k \to 0$ limit the scattering process is effectively described by only one parameter, the s-wave scattering length. Intuitively, this can be anticipated, as the deBroglie-wavelength of the scattering particle is too large to resolve the details of the potential. When compared to the length scale of the scattering solution, $\frac{1}{k}$, the size of the potential becomes arbitrarily small, i.e. $kR \ll 1$, and we are tempted to ignore the actual form of $\psi_k(r)$ inside the potential completely. Extending the $r \geq R$ solution to all of space one observes the following diverging behavior of the wavefunction as $r \to 0$, where the three-dimensional case is known as the Bethe-Peierls boundary condition [Bethe and Peierls, 1935]

$$\psi_k(r) \sim \begin{cases} \ln(re^{\gamma}/2a) & \text{in 2D} \\ \\ (\frac{1}{r} - \frac{1}{a}) & \text{in 3D} \end{cases}. \tag{2.15}$$

In fact, enforcing these boundary conditions yields the approximative low energy solutions discussed so far as exact scattering solutions for the free Hamiltonian. Beyond the scattering solution, one finds a single bound state for arbitrary scattering length in two dimensions and for positive scattering length in three dimensions. The bound state has energy $E_b = -\frac{\hbar^2}{2\mu a^2}$ in two and three dimensions [Whitehead et al., 2016][3][Giorgini et al., 2008] and its spatial extension is given by the scattering length. Note that the bound state only yields an accurate, physical description if the scattering potential actually hosts at least one shallow bound state.
Finally, it is also possible to enforce the boundary condition eq. (2.15) by means of a

[3]Note that Whitehead et al. [2016] use a different definition of the 2d-scattering length $\tilde{a}$ which is matched by identifying $\tilde{a} = 2ae^{-\gamma}$.

regularized delta function or a simple delta function $g\delta^{(d)}(\vec{r})$ with appropriate renormalization of the coupling constant g. Such potentials are termed pseudopotentials or, since they involve delta functions, contact interactions.

2.1.4 Scattering of identical particles

The potential scattering discussed so far is easily extended to describe the scattering between particles interacting via a potential $V(|\boldsymbol{x}_1 - \boldsymbol{x}_2|)$. Like in the classical case the problem can be separated into a free motion of the center-of-mass coordinate and an interacting problem for the relative coordinate $\boldsymbol{x} = \boldsymbol{x}_1 - \boldsymbol{x}_2$. The latter is formally equivalent to the case of potential scattering, where only the mass of the particles m_1 and m_2 has to be replaced by the reduced mass $\mu = \frac{m_1 m_2}{m_1+m_2}$.
Interesting consequences arise when the scattering takes place between identical particles. The total wavefunction (including additional degrees of freedom like spin) has to fulfill the (anti)-symmetry condition

$$\Psi(\boldsymbol{x}_1, \boldsymbol{x}_2) = \pm\Psi(\boldsymbol{x}_2, \boldsymbol{x}_1), \tag{2.16}$$

where the positive sign is picked for bosonic and the negative sign for fermionic particles. This condition translates to

$$\psi(\boldsymbol{x}) = \pm\psi(-\boldsymbol{x}) \tag{2.17}$$

for the relative wavefunction ψ. Taking a scattering solution $\psi_k(\boldsymbol{x})$ the symmetrization condition is straightforward to implement via

$$\psi_{\pm,k}(\boldsymbol{x}) = \frac{1}{\sqrt{2}}\left(\psi_k(\boldsymbol{x}) \pm \psi_k(-\boldsymbol{x})\right). \tag{2.18}$$

The partial waves of the solutions (2.10) have parity $(-1)^m$, $(-1)^l$ under the transform $\boldsymbol{x} \to -\boldsymbol{x}$ (or $\theta \to \pi - \theta$) and hence all even angular-momentum channels vanish in $\psi_{-,k}$, all odd channels in $\psi_{+,k}$, respectively . This has especially drastic consequences for fermions in the low energy regime. If there is no other degree of freedom left, the radial wavefunction has to be antisymmetric and thus the s-wave scattering is suppressed completely. Particularly, this means that fermionic particles of like spin do not interact at low energies.

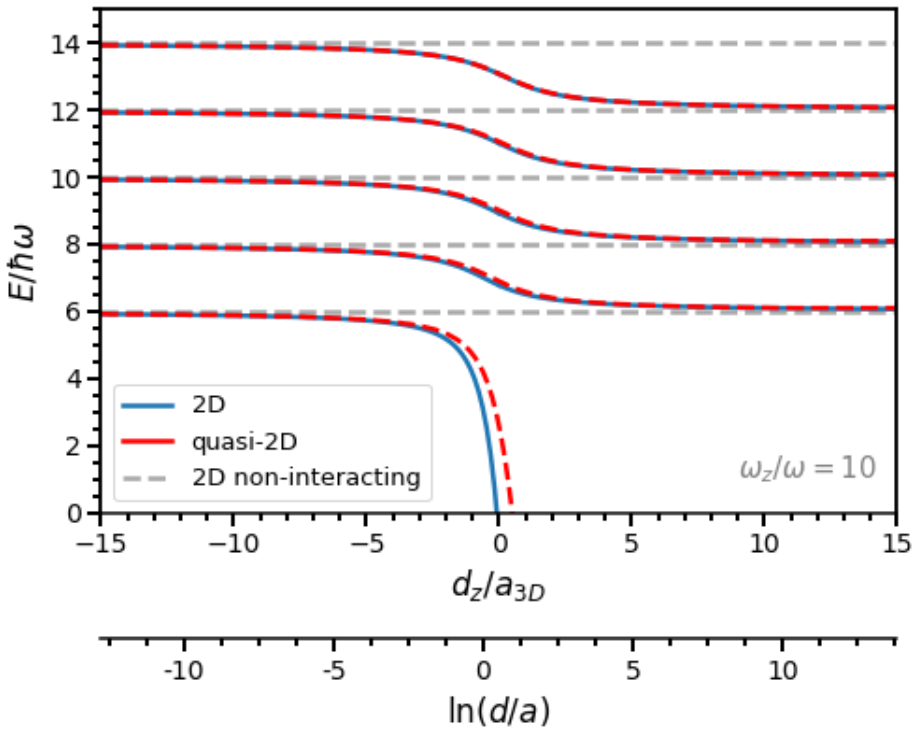

Figure 2.1: **Energy spectrum in quasi-2D**
Comparing the exact quasi-2D energy spectrum with the pure 2D-approximation in a pancake trap with aspect ratio $\omega_z/\omega = 10$. The energy is plotted as a function of the inverse 3D-scattering length (in units of the relative axial harmonic oscillator length d_z) and the corresponding 2D interaction parameter (2D-scattering length in units of the relative 2D harmonic oscillator length d), respectively. Only the relative motion states are depicted. The pure 2D-solution is shifted to match the 3D vacuum energy of the quasi-2D solution.

2.2 Interacting particles in a harmonic trap

So far we have only studied the scattering properties of particles in free space. However, the experimental reality looks different, as particles are confined in usually harmonic, or close to harmonic, traps. This significantly alters the inter-particle scattering leading to a series of bound states instead of a continuous scattering spectrum. Still assuming the validity of the low energy description, analytic results have been derived for two particles in anisotropic harmonic traps for different dimensions. We merely state the results here as a more detailed discussion is given later in the context of numerical methods anyway. Busch et al. [1998] find the radial ($m = 0$) energy spectrum [4] for two interacting particles in an isotropic two-dimensional har-

[4] I.e. after separating the problem in center-of-mass and radial coordinates as will be laid out later. Moreover, only states of zero relative angular momentum are coupled by the contact

monic trap to be given by

$$\psi\left(\frac{1}{2}-\frac{E}{2\hbar\omega}\right)=2\ln(d/a)=2\ln(\sqrt{2}l_0/a), \tag{2.19}$$

where ψ is the Digamma function, $l_0=\sqrt{\hbar/m\omega}$ and $d=\sqrt{2}l_0$ are the harmonic oscillator length in the full and the relative system, respectively, a is the 2D-scattering length describing the inter-particle scattering, m is the particles mass and ω is the trapping frequency.
Experimentally, a two-dimensional trap can be realized by making the trapping frequency along one axis, say the z-axis, ω_z much larger than along the remaining axes. Starting from an arbitrarily shaped three dimensional harmonic trap Idziaszek and Calarco [2006] have identified this quasi-2D regime. They relate the 2D-scattering length to the 3D-scattering length by

$$a\approx\frac{d_z}{\sqrt{2}}\exp\left(\frac{1.938}{2}-\frac{\sqrt{\pi}d_z}{2a_{3\mathrm{D}}}\right), \tag{2.20}$$

with the relative axial harmonic oscillator length $d_z=\sqrt{2\hbar/m\omega_z}$. The 2D-description is found to be valid provided that $|E-\hbar\omega|/\hbar\omega_z\ll 1$ holds.
The energy spectrum of the relative motion in a quasi-2D pancake-shaped trap is depicted in Fig. 2.1. In comparison to the exact quasi-2D solution [Idziaszek and Calarco, 2006] the pure 2D-solution with the 2D-scattering length given by eq. (2.20) and the non-interacting spectrum for states with zero relative angular momentum are plotted. Firstly, we observe that the non-interacting solution is recovered in the limit $a_{3\mathrm{D}}\to 0^-$, corresponding to a vanishing interaction potential between the atoms. Furthermore, the ground state energy is well-described on the entire negative branch $a_{3\mathrm{D}}<0$. On the other hand, for positive 3D-scattering lengths, the true ground state energy is only well-approximated in the regime $a_{3\mathrm{D}}/d_z\gg 1$. This can be understood intuitively as follows. For positive scattering lengths the scattering potential becomes sufficiently deep to host a two-body boundstate (the dimer- or halo-molecule-state), the spatial extension of which is given by the 3D-scattering length. The 2D-approximation now breaks down once the size of the dimer becomes smaller than the axial-confinement of the trap and the molecule-states recovers its three dimensional nature. Alternatively, and perhaps more rigorously, the same statements can be derived by looking at the approximation of the ground state $\frac{E_0-E}{\hbar\omega_z}\approx 0.288e^{\sqrt{\pi}d_z/a_{3\mathrm{D}}}$, valid for $|E-E_0|/\hbar\omega_z\ll 1$ [Idziaszek and Calarco, 2006]. As stated above, this is exactly the regime in which we expect the pure 2D-description to be valid.
As long as one is just interested in a few of the lowest excited states, the system might nevertheless be accurately described as 2D in the regime $0<a_{3\mathrm{D}}/d_z\ll 1$. While it may seem odd in the beginning to simply ignore the deeply bound dimer-state, this situation is actually of great experimental relevance. Namely, when the

interaction. The spectrum of the uncoupled states is omitted for clarity.

ultracold gas is prepared on the positive branch of the Feshbach-resonance ($a_{3\mathrm{D}} > 0$) the overlap between the 'warm' gas and the molecular-ground state is too small to significantly populate the latter during the cooling process. If the experimental situation allows us too neglect the dimer-state beyond some binding energy on the scale of the level spacing $\hbar\omega$ we expect the pure 2D-description of the bound state and the lowest excited states to be accurate in the regime $|a_{3D}/d_z| \ll 1$.

2.3 Properties of ^{6}Li

All experiments carried out in our group work with ^{6}Li. With its three protons, neutrons and electrons this isotope behaves fermionic in nature. Two of the three electrons fill the $1s$-shell and hence the electronic ground state is determined by the remaining valence electron in the $2s$ level, resulting in orbital angular momentum $L = 0$ and total electronic angular momentum $J = 1/2$ from the electrons spin. Fig. 2.2A shows the level structure of ^{6}Li, in particular it shows the optical D_1 and D_2 transitions at around 671 nm between the ground state and excited manifolds and the hyperfine splitting due to coupling of the angular momentum J of the electron to the spin $I = 1$ of the nucleus. Fig. 2.2B shows the splitting of the hyperfine levels in an external magnetic field. Beyond 100 G the splitting is well described by the Paschen-Back effect as the coupling of the magnetic field to the spin of the electron and the nucleus become stronger the spin-orbit coupling. In this limit the three lowest states are given by $|-\frac{1}{2}, 1\rangle, |-\frac{1}{2}, 0\rangle$ and $|-\frac{1}{2}, -1\rangle$, labeled by the z-projection of electronic and nucleus spin, respectively. Experiments are usually performed in the region of $[250, 1000]$ G using two of these three states which allows the system to be formally described as a spin-1/2 system. The splitting of ~ 80 MHz between the states, corresponding to ~ 3.8 mK, is much larger than the typical temperature of the gas reached during cooling of less than 1 µK [Klemt, 2021], and hence any thermal effects altering the nuclear spin state of the atoms can be safely neglected. Furthermore, protocols between all six states $|1\rangle$-$|6\rangle$ can be implemented experimentally via direct radio-frequency transitions [Klemt, 2021] or alternatively, by optical Raman-transitions via states in the excited manifold [Abbas, 2021].

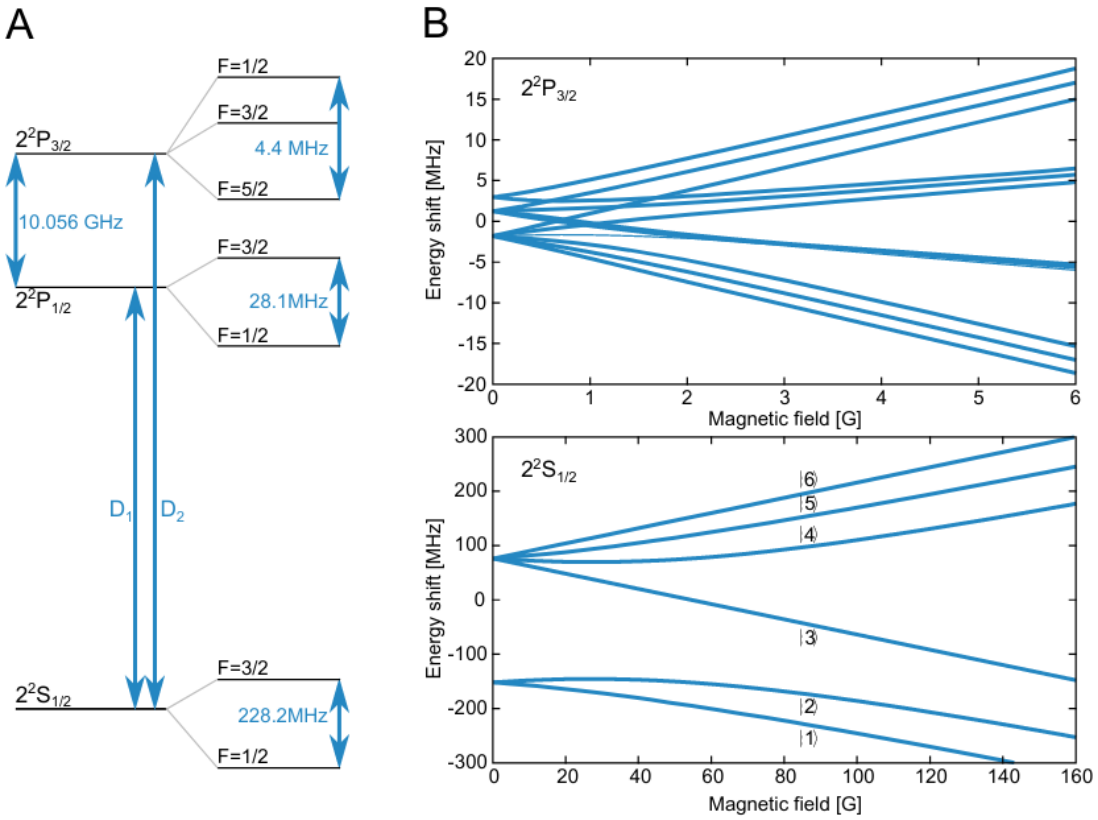

Figure 2.2: **Hyperfine spectrum of ^{6}Li and Zeeman splitting**
A - Hyperfine level structure of ^{6}Li at zero magnetic field. The experimentally relevant states are hosted in the ground state $2^2S_{1/2}$-manifold. The optical D_1 and D_2 at around 671 nm are used for cooling, trapping and imaging the Lithium gas. **B** - The hyperfine manifolds split further in the presence of a magnetic field. The experimentally relevant states are the three lowest states $|1\rangle$, $|2\rangle$, $|3\rangle$. Beyond 100 G they enter the Paschen-Back regime and are split by 80 Mhz $\sim$ 331 neV $\sim$ 3.8 mK. Taken from [Klemt, 2021].

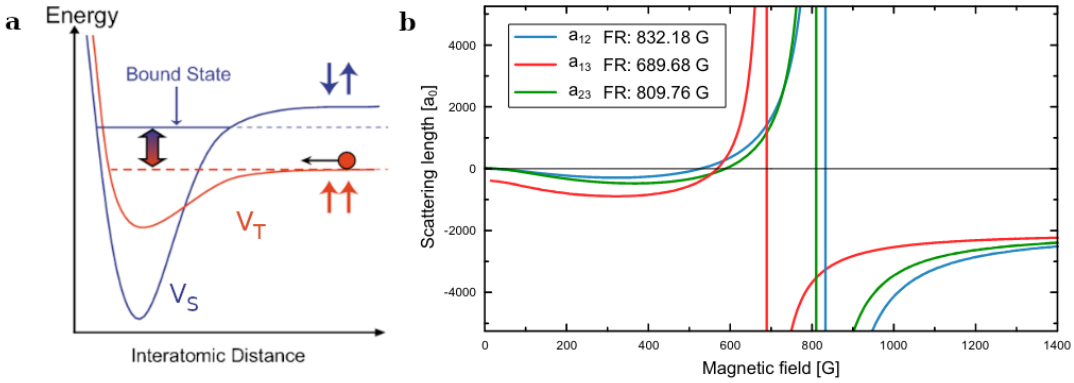

Figure 2.3: **Feshbach resonance of ^{6}Li**
a - A sketch of the inter-atomic potential of ^{6}Li. The potential strongly depends on the spin-wavefunction of the colliding atoms valence electrons which can either be in a spin-triplet (V_T) or spin-singlet (V_S). Due to the external magnetic field the potentials are shifted depending on the total spin-projection of the electrons. Note that the arrows only indicate the electron spins! Taken and adapted from [Ketterle and Zwierlein, 2008]. **b** - The Feshbach resonance of ^{6}Li occurs when the bound state becomes energetically accessible which is accompanied by a pole in the scattering length. For each mixture of the states $|1\rangle - |3\rangle$ the inter-atomic potentials look slightly different, giving rise to different scattering lengths and resonances. Taken from [Klemt, 2021].

2.3.1 The Feshbach-resonance of ^{6}Li

At low temperatures the scattering properties of the Lithium atoms can effectively be described by only one parameter, the s-wave scattering length. Luckily, the scattering process is often times sensible to external magnetic fields and even exhibits scattering resonances, where the scattering length quickly runs over a large range of negative and positive values. These so called Feshbach-resonances allow one to tune the interaction between the atoms from non-interacting to strongly attractive or repulsive, making them ideal candidates for quantum simulation. An extensive discussion of this subject can be found in [Chin et al., 2010] and we merely want to recap a few important results here.
Like the level structure, the inter-atomic potential of Lithium is greatly influenced by its valence electron. When two atoms collide, their valence electrons can be in a symmetric spin triplet or an antisymmetric spin singlet state. Since the electronic wavefunction has to be antisymmetric in total, the spatial part of the wavefunction correspondingly has to be of opposite symmetry. In the triplet state the antisymmetric spatial wavefunction has a knot whenever the position of the two electrons coincides and hence the electrons tend to avoid each other. This leads to less screening of the positively charged nuclei, i.e. stronger repulsion and a in total less attractive

(Born-Oppenheimer)-potential $V_T(R)$ for the atomic separation R as compared to the singlet-case. Both the singlet potential $V_S(R)$ and the triplet potential $V_T(R)$ are depicted in Fig. 2.3a. From Fig. 2.2B we see that the spin -1/2-states ($|1\rangle$-$|3\rangle$) and spin +1/2-states ($|4\rangle$-$|6\rangle$) get shifted in energy at non-zero magnetic field. The triplet and singlet potentials get shifted correspondingly depending on their total spin z-projection. While the singlet-channel is not directly accessible due to its large energy shift it is nevertheless coupled to the experimentally relevant $\downarrow\downarrow$-triplet state via the hyperfine interaction [Ketterle and Zwierlein, 2008]. Note that in contrary to the triplet potential, the singlet potential hosts a bound state rather close to the energy of the colliding atoms. All of this significantly impacts the scattering process which now has to be described using a coupled-channel model. However, since the energy of the singlet-channel is too high it always remains closed, i. e. the incoming atoms can never scatter into states with different electronic spins. Furthermore, the bound state remains a forbidden exit state for two-particle scattering due to conservation of momentum and hence the scattering process remains coherent in nature and can still be described by the s-wave scattering length. [5] Fig. 2.3b shows the scattering length for varying magnetic field. Note that the scattering length has a pole where it quickly runs through $-\infty$ and $+\infty$ when the bound state is tuned very close to the energy of the incoming atoms. Shortly after the resonance at positive scattering lengths the bound state is energetically accessible and its energy is given by that of a shallow bound state in a pseudopotential $\frac{\hbar^2}{ma^2}$ as discussed previously. Beyond this point the bound state becomes essentially too deeply bound to significantly impact the scattering process anymore. In this regime the relation $E = \frac{\hbar^2}{ma^2}$ is rendered useless.

2.4 Preparing an ultracold Fermi gas

A cloud of ^{6}Li-atoms is initially loaded into a magneto-optical trap (MOT) where it is laser-cooled to around a few hundred µK. At this point the recoil energy introduced by the photons scattering off the atoms dominates their thermal motion and cooling essentially stops. This requires non-resonant techniques to be used where photon-scattering becomes suppressed. To this end we employ a optical dipole trap (ODT) of infrared laser-light at 1064 nm. The electric component of the strong light field induces a dipole moment $\boldsymbol{p}$ which subsequently interacts with the laser field via the potential $V \sim -\boldsymbol{p} \cdot \boldsymbol{E}$. This can be treated semiclassically yielding the trapping potential [Grimm et al., 2000]

$$V(\boldsymbol{x}) = -\frac{3\pi c^2}{2\omega_0^3}\left(\frac{\Gamma}{\omega_0 - \omega_L} + \frac{\Gamma}{\omega_0 + \omega_L}\right) I(\boldsymbol{x}). \tag{2.21}$$

[5] If energetically accessible two particles can in principle scatter into the molecular bound state in the presence of a third particle, making the scattering incoherent. However, at the experimental conditions we are going to consider such three-particle processes are very unlikely and thus we shall neglect them entirely.

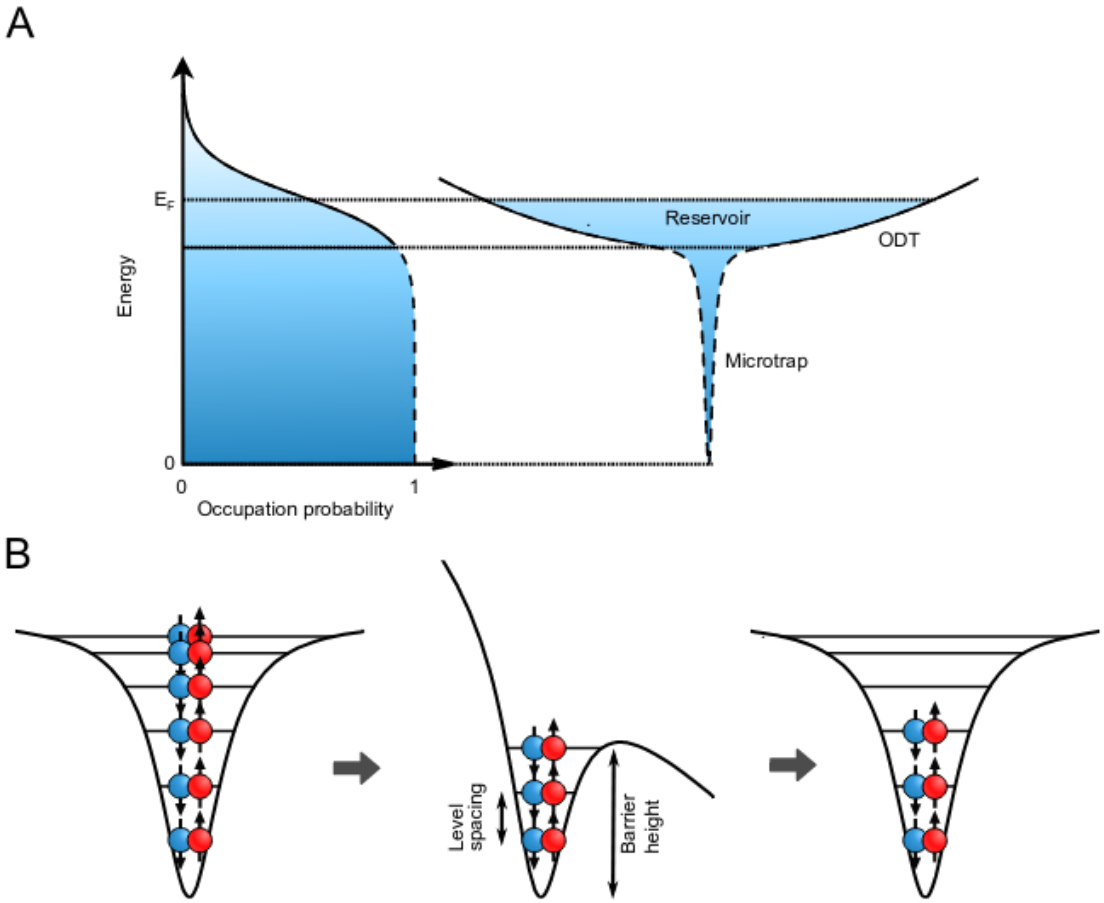

Figure 2.4: **Deterministic preparation of few-particles**
A - Additional to the ODT a smaller but much deeper *microtrap* is switched on. On the left side the occupation probability of the gas in the ODT is shown, which corresponds to $T/T_f \sim 0.5$. The *microtrap* gets completely filled with atoms from the surrounding reservoir. Switching off the ODT hence results in highly degenerate gas with $T/T_f \sim 0.05$ in the *microtrap*. **B** . Adding a magnetic field gradient to the trap leads to spilling of atoms from the trap. In this way samples of small atom number can be prepared. Taken from [Klemt, 2021].

Here ω_0 is the frequency of the optical transition (the D_2 line) and Γ is its linewidth. Furthermore, ω_L is the frequency of the ODT-laser and $I(\boldsymbol{x})$ is the light fields intensity distribution. Introducing the detuning $\Delta = \omega_0 - \omega_L$ we see that for red-detuned light, i.e. $\Delta > 0$, the atoms experience an attractive force towards the intensity maxima of the laser field. Since the photon-scattering rate scales as Δ^{-2}, it is favorable to choose a large detuning. This suppresses the photon-scattering effectively, while the same trap depth can be maintained by cranking up the laser power accordingly. Once the atoms are transferred from the MOT to the ODT, the laser power can be decreased again. This leads to the evaporation of hot atoms from the trap which finally allows us to reach temperatures of around 100 nK [Serwane et al., 2011].

To increase the degeneracy of the Fermi gas another much narrower laser beam is shone into the ODT. This creates an additional small but very deep *microtrap* which as indicated in Fig. 2.4B gets completely filled with atoms from the ODT. Since all states in the microtrap are filled with almost certainty, switching off the ODT leaves us with a highly degenerate Fermi gas with $T/T_f \sim 0.05$. In a final step, a magnetic field gradient is applied, which deforms the microtrap as depicted in Fig. 2.4B. As a consequence all atoms above a certain energy level escape from the trap allowing us to prepare systems of few atoms (down to only two atoms) with fidelities above 90 % [Serwane et al., 2011].

One last ingredient is needed to go from the cigar-shaped microtrap into the 2D-regime. By using a standing wave dipole trap thin pancake-shaped layers of high light intensity can be created [Petzold, 2016]. Such traps are designed to have a high aspect ratio ω_z/ω_r of around 100, with $\omega_z \approx 2\pi \cdot 30$ kHz. These layers are then to be oriented perpendicular to the microtrap (or the rotating trap later on). Due to the weak radial confinement of the pancake-trap the microtrap will control the radial trapping frequency of the combined trap, while the z-confinement is set by the pancake-trap.

3 Numerical Study of interacting atoms in a 2D-trap

Analytic solutions for the problem of interacting cold atoms in a harmonic trap are available only for two particles. We therefore make an attempt to solve the problem numerically, at least for a few particles.
Again assuming the atoms to be sufficiently cold, we neglect any higher angular momentum-scattering, and incorporate the s-wave interaction via a simple delta function. We further adopt a purely two-dimensional model, for which the Hamiltonian becomes

$$H = \sum \left(-\frac{1}{2}\Delta_i + \frac{1}{2}\boldsymbol{x}_i^2 \right) + g \sum_{i<j} \delta^{(2)}(\boldsymbol{x}_i - \boldsymbol{x}_j), \tag{3.1}$$

where we expressed energies in terms of $\hbar\omega$ and lengths in terms of the harmonic oscillator length l_0. Furthermore, g is the coupling constant carrying units of energy times length squared (i.e. $g_{SI} = g\hbar\omega l_0^2$). Note that this Hamiltonian is unphysical, since it is not bounded from below. However, it turns out that working on a finite Hilbert space and carefully choosing the bare coupling constant g in terms of e.g. the 2D-scattering length, allows one to obtain meaningful results in the limit of the Hilbert space dimension going to infinity. Since using numerical methods forces us to truncate the infinite Hilbert space anyway, this approach to incorporating the s-wave scattering seems natural.
Let's firstly lay out the renormalization procedure in detail be revisiting the two particle problem.

3.1 Renormalization of the coupling constant for the two particle-problem

In the two particle case it's convenient to introduce center-of-mass and relative coordinates as

$$\boldsymbol{X} \equiv \frac{1}{2}(\boldsymbol{x}_1 + \boldsymbol{x}_2), \quad \boldsymbol{x} \equiv \boldsymbol{x}_1 - \boldsymbol{x}_2. \tag{3.2}$$

Eq. (3.1) then reads

$$H = \underbrace{-\frac{1}{4}\Delta_{\boldsymbol{X}} + \boldsymbol{X}^2}_{H_{com}} + \underbrace{-\Delta_{\boldsymbol{x}} + \frac{1}{4}\boldsymbol{x}^2 + g\delta^{(2)}(\boldsymbol{x})}_{H_{rel}}. \tag{3.3}$$

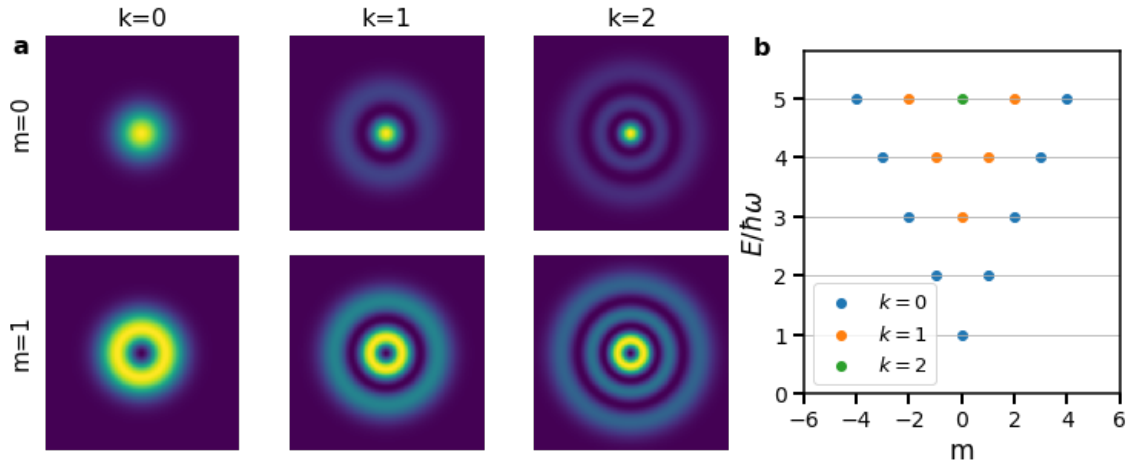

Figure 3.1: **States and spectrum of the 2D isotropic-harmonic oscillator** **a** - Probability density for a few low laying eigenstates of the two-dimensional isotropic harmonic oscillator. m labels angular momentum. The number of nodes of the wavefunction is given by the primary quantum number k. **b** - The energy spectrum of the two-dimensional isotropic harmonic oscillator. The eigenstates form shells of equal energy. The n-th shell ($n = 2k + |m| = 0, ...$) contains $n + 1$ states.

Since the center-of-mass motion is non-interacting, we neglect it for the remainder of this section. Further re-expressing $\boldsymbol{x}$ and g in terms of the relative oscillator length $d = \sqrt{2}l_0$, leaves us with the effective one-particle Hamiltonian

$$H = \frac{1}{2}(-\Delta_{\boldsymbol{x}} + \boldsymbol{x}^2) + g\delta^{(2)}(\boldsymbol{x}). \tag{3.4}$$

Next we want to expand the Hamiltonian on the angular momentum eigenbasis of the 2D-harmonic oscillator. The eigenfunctions in units of the corresponding harmonic oscillator are given by

$$\begin{aligned} &\psi_{km}(r,\theta) = \langle r,\theta|k,m\rangle \equiv R_{km}(r)\phi_m(\theta) \\ &R_{km} = \sqrt{\frac{2k!}{(k+|m|)!}} r^{|m|} L_k^{|m|}(r^2) e^{-\frac{1}{2}r^2}, \quad \phi_m(\theta) = \frac{1}{\sqrt{2\pi}} e^{im\theta}, \end{aligned} \tag{3.5}$$

where m runs over all integers, k over all non-negative integers and $L_k^m(x)$ are the generalized Laguerre-polynomials. (3.5) are simultaneous eigenfunctions of the angular momentum operator $\hat{M} = -i\hbar\frac{\partial}{\partial\theta}$ with eigenvalue $\hbar m$ and the 2D-isotropic harmonic oscillator with eigenenergy $E = \hbar\omega(2k + |m| + 1)$. Furthermore, they form an orthonormal basis of the Hilbert space of square-integrable functions on $\mathbb{R}^2$. Some of these eigenstates and the energy spectrum are depicted in Fig. 3.1.
Using these wavefunctions we can write the Hamiltonian as

$$H = \sum_{\substack{k=0 \\ m=-\infty}}^{\infty} (2k + |m| + 1) \left|k,m\right\rangle \left\langle k,m\right| + \frac{g}{\pi} \sum_{\substack{k=0 \\ k'=0}}^{\infty} \left|k,0\right\rangle \left\langle k',0\right|. \tag{3.6}$$

We observe that the problem separates again, since only the zero angular momentum modes interact. This is just as expected since the centrifugal barrier completely hides the zero-range contact interaction.
Again neglecting the non-interacting part we may now attempt to solve for the eigenvalues by the ansatz $|\psi\rangle = \sum_k c_k |k, 0\rangle$. Acting on the Hamiltonian and projecting out a single state yields

$$(E - 2k - 1)c_k = \frac{g}{\pi} \sum_{k'} c_{k'}. \tag{3.7}$$

Dividing by $(E - 2k - 1)$ and summing over k finally leaves us with

$$\frac{\pi}{g} = \sum_k \frac{1}{E - 2k - 1}, \tag{3.8}$$

which unfortunately is terribly divergent. We deal with this by first regularizing the sum by cutting it off at K_c, allowing us to write eq. (3.8) as

$$\frac{2\pi}{g} = \psi(-\epsilon/2) - \psi(K_c + 1 - \epsilon/2), \tag{3.9}$$

where $\psi(x)$ is once more the Digamma-function and $\epsilon = E - 1$. While this doesn't change anything about the divergent behavior we might already recognize the first term as the left hand side of eq. (2.19). What if we could just cancel the remaining term in the $K_c \to \infty$ limit ? Indeed, we so far haven't attributed any physical meaning to the coupling constant g and might as well just try to push the divergence here. Observing that $\psi(N + x) - \psi(N + y) \sim \mathcal{O}(1/N)$ [1] as $N \to \infty$, we find that any kind of replacement $2\pi/g \to 2\pi/g_0 - \psi(K_c + 1 + x)$ will cancel the divergence in eq. (3.9). Putting everything together and using eq. (2.19) we find that the bare coupling constant (in relative harmonic oscillator units)

$$g(g_0; K_c, x) = \frac{g_0}{1 - \frac{g_0}{2\pi}\psi(K_c + 1 + x)}, \quad \pi/g_0 \equiv \ln(1/a) \tag{3.10}$$

is itself divergent. However, all physical observables are now divergence-free and in the $K_c \to \infty$ limit the energy spectrum (2.19) is predicted correctly. Loosely speaking, we constructed a family of models $H(g_0; K_c, x)$ which in renormalization-group-language flow, for $K_c \to \infty$, to a fixed point $H(g_0)$ independent of x.

While for the fixed point the choice of x is irrelevant it does significantly influence the behavior at finite K_c. Consider for example the two-body bound state with $\epsilon < 0$ in eq. (3.8). Since for $\epsilon < 0$ the right hand side is negative, the left hand side must be negative as well. This means that in the finite Hilbert space the bound state is only found provided that $g < 0$ or equivalently in the region

$$\frac{2\pi}{g_0} = \ln(1/a) < \psi(K_c + 1 + x). \tag{3.11}$$

[1] using that $\psi(z) \sim \ln z + \mathcal{O}(1/z)$ for large z

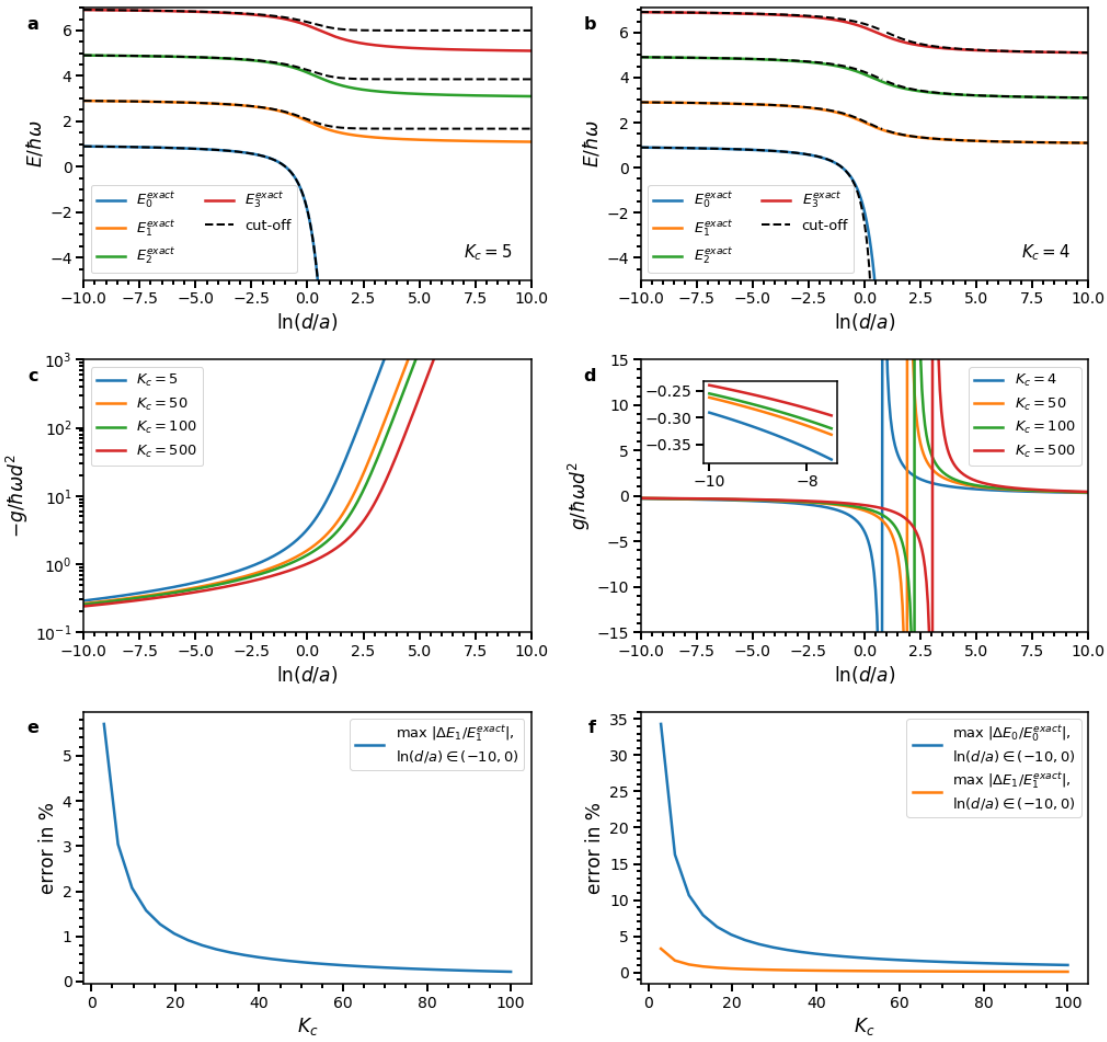

Figure 3.2: **Renormalization of the coupling constant**
Comparing two different renormalization conditions for a system of two interacting atoms in a two-dimensional isotropic, harmonic trap. Only the interacting, relative motion spectrum is considered and the Hilbert space is truncated at K_c as explained in the main text. **Left (a,c,e)** - the bare coupling constant g is chosen such that the numerical ground state energy always matches the true ground state energy. **Right (b,d,f)** - the bare coupling constant is fixed, somewhat arbitrarily, via $x = 0$ in eq. (3.10). **Upper panel (a,c)** - exact and cut-off energy spectrum. **Middle panel (c,d)** - running of the coupling with interaction strength. **Lower panel (e,f)** - speed of convergence for first states in the region $\ln(d/a) \in (-10, 0)$.

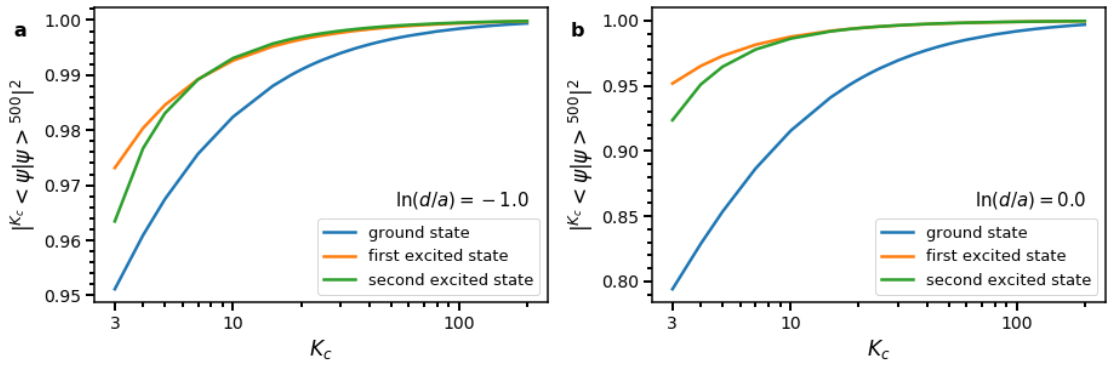

Figure 3.3: **Convergence of Overlap**
Overlap of eigenstates for different cut-offs K_c with corresponding eigenstates at very high cut-off of $K_c = 500$. The first three lowest, interacting eigenstates of two particles in a 2D isotropic, harmonic trap are depicted. The coupling constant is renormalized by the ground state condition. **a** - overlap at $\ln(d/a) = -1$. **b** - overlap at $\ln(d/a) = 0$.

For constant x the boundary of that region is just the pole of $g(g_0)$, where the bare coupling constant jumps from negative to positive values.
By choosing $x = -\epsilon_0/2$, with ϵ_0 being the exact bound state energy, we see that ϵ_0 is a solution to equation (3.9) at any K_c, i.e. the two-body bound state energy is always found exactly. Furthermore, $g < 0$ for all g_0 [2] and we avoid the pole in eq. (3.10) completely. This renormalization condition is especially useful as it allows one to link the bare coupling to experimental observables directly, without the need of knowing a mapping between g_0, K_c and g in advance.
The resulting energy spectrum from eq. (3.9) is compared with the exact solution in Fig. 3.2. The left column and right column depict the choice $x = -\epsilon_0/2$ and $x = 0$, respectively. As discussed previously, we only find a pole in the bare coupling constant g in the $(x = 0)$-case. Furthermore, the maximal relative error between the predicted and the exact energy spectrum is plotted in the lowest panel. We observe that already a small cut-off K_c yields good results for the first eigenstates. However, one is usually not only interested in predicting the eigenenergies but also the eigenstates. To get a feeling for how well the eigenstates are explained we plot the overlap between a few of the lowest eigenstates computed at various K_c with numerical solutions computed at a high cut-off of $K_c = 500$ in Fig. 3.3. We observe that already for a small size of the Hilbert space, an overlap close to 1 is obtained. The overlap depends on the interaction strength, where a higher K_c is needed for stronger interactions. For this figure the ground state renormalization condition was chosen.

[2] From eq. (3.9) evaluated at ϵ_0 we get $2\pi/g_0 = \psi(-\epsilon_0/2)$. Further noting that $\psi(x+N)-\psi(x) > 0$ for $x > 0$ already yields $g < 0$.

3.2 The Hamiltonian in second quantization

We have seen that in the two particle case the renormalized model is exactly solvable when working in center-of-mass and relative motion coordinates. Unfortunately, this method doesn't generalize well to cases with more than two particles. Instead we will make use of the formalism of second quantization, i. e. we will expand the Hamiltonian on a basis of one-particle spin-orbitals. This however, greatly blows up the size of the Hilbert space, such that even the two-particle problem becomes numerically hard to solve.
Introducing the creation operators $a_i^\dagger$, we can create a particle in mode $|i\rangle \equiv |\alpha_i, \sigma_i\rangle \equiv |k_i, m_i, \sigma_i\rangle$ by acting on the vacuum state $|0\rangle$ via

$$|i\rangle = a_i^\dagger |0\rangle , \tag{3.12}$$

where k and m label the 2D-harmonic oscillator states in the usual way and σ describes the spin degree of freedom, $\sigma \in \{\uparrow, \downarrow\}$. For convenience we summarize the orbital labels k and m in the index α at times. Since we deal with a system of fermionic particles we require the creation operators to anti-commute with their hermitian conjugates

$$\{a_i, a_j^\dagger\} = a_i a_j^\dagger + a_j^\dagger a_i = \delta_{ij}, \quad \{a_i, a_j\} = \{a_i^\dagger, a_j^\dagger\} = 0 \tag{3.13}$$

and further demand that the a_i operators annihilate the vacuum $a_i |0\rangle = 0$. Hence, the operators a_i annihilate a particle in mode i, which can be seen from $a_i |i\rangle = a_i a_i^\dagger |0\rangle = |0\rangle$. We finally note that correctly symmetrized multi particle states are simply created by acting multiple times on the vacuum, e.g. $a_i^\dagger a_j^\dagger |0\rangle$ creates a state $\frac{1}{\sqrt{2}} (|i; j\rangle - |j; i\rangle)$. We can use the states created in this fashion to span the Hilbert space of N-fermions as $\mathcal{H}_N^{(-)} = \text{span}\{a_{i_1}^\dagger ... a_{i_N}^\dagger |0\rangle , \text{for all } i_1, ..., i_N\}$.[3]
With all these tools at hand we can finally write the Hamiltonian (3.1) as

$$H = \sum_i \underbrace{(2k_i + |m_i| + 1)}_{\equiv E_i} a_i^\dagger a_i + \frac{g}{2} \sum_{ijnl} \langle i; j|\delta^{(2)}(\boldsymbol{x} - \boldsymbol{y})|n; l\rangle \, a_i^\dagger a_j^\dagger a_l a_n. \tag{3.14}$$

Here $|i; j\rangle$ is denotes the unsymmetrized product state $|i\rangle \otimes |j\rangle$. Further, note that the order of the fermionic creation and annihilation operators in the two-particle term matters. Next, we have to evaluate the matrix elements of the delta function. Expanding the states in the position basis we find for $\frac{1}{2} \langle i; j|\delta^{(2)}(\boldsymbol{x} - \boldsymbol{y})|n; l\rangle$

$$\begin{aligned} \langle \sigma_i|\sigma_n\rangle \langle \sigma_j|\sigma_l\rangle \underbrace{\int_0^\infty dr r R_{\alpha_i}(r) R_{\alpha_j}(r) R_{\alpha_n}(r) R_{\alpha_l}(r)}_{\equiv 2\pi R[\alpha_i, \alpha_j, \alpha_n, \alpha_l]} \int_0^{2\pi} \frac{d\theta}{2(2\pi)^2} e^{i\theta(m_n + m_l - (m_i + m_j))} \\ = \frac{1}{2} \delta_{\sigma_i, \sigma_n} \delta_{\sigma_j, \sigma_l} \delta_{M, M'} R[\alpha_i, \alpha_j, \alpha_n, \alpha_l], \end{aligned}$$

[3] The creation and annihilation operators connect the Hilbert spaces of different particle number. Their action is closed on the Fock state defined as $\mathcal{F}^{(-)} = \bigoplus_{n=0}^\infty \mathcal{H}_n^{(-)}$, which contains states of uncertain particle number.

(3.15)

where $R_\alpha(r) = R_{km}(r)$ is defined in eq. (3.5) and $M = m_n + m_l$, $M' = m_i + m_j$ are the total angular momentum of the incoming and outgoing states. The factor $\delta_{M,M'}$ thus ensures angular momentum conservation during the interaction. Note that the integral $R[\alpha, \beta, \gamma, \delta]$ is fully symmetric under index exchange which has some important consequences. Plugging this into eq. (3.14) yields

$$H = \sum_i E_i a_i^\dagger a_i + \frac{g}{2} \sum_{\substack{\alpha,\beta,\gamma,\delta \\ \sigma_1 \neq \sigma_2}} R[\alpha, \beta, \gamma, \delta] \delta_{M,M'} a^\dagger_{\alpha,\sigma_1} a^\dagger_{\beta,\sigma_2} a_{\delta,\sigma_2} a_{\gamma,\sigma_1}, \tag{3.16}$$

where the $\sigma_1 = \sigma_2$ contribution vanishes because we can always find two terms $R[\alpha, \beta, \gamma, \delta] a^\dagger_{\alpha,\sigma} a^\dagger_{\beta,\sigma} a_{\delta,\sigma} a_{\gamma,\sigma} = -R[\alpha, \beta, \gamma, \delta] a^\dagger_{\alpha,\sigma} a^\dagger_{\beta,\sigma} a_{\gamma,\sigma} a_{\delta,\sigma}$ and $R[\alpha, \beta, \delta, \gamma] a^\dagger_{\alpha,\sigma} a^\dagger_{\beta,\sigma} a_{\gamma,\sigma} a_{\delta,\sigma}$ that cancel each other out due to the symmetry of $R[\cdot]$. This reflects the fact that, as discussed earlier, the s-wave interaction is suppressed for particles with like spin. In a last step we write out the spin sum and use the symmetry of R again to finally arrive at

$$H = \sum_i E_i a_i^\dagger a_i + g \sum_{\alpha,\beta,\gamma,\delta} R[\alpha, \beta, \gamma, \delta] \delta_{M,M'} a^\dagger_{\alpha,\uparrow} a^\dagger_{\beta,\downarrow} a_{\delta,\downarrow} a_{\gamma,\uparrow}. \tag{3.17}$$

The integrals $R[\alpha, \beta, \gamma, \delta]$ can be computed numerically, where the computational effort can be reduced by taking into account the symmetry of $R[\cdot]$ and angular momentum conversation.

3.3 Quanty - a many body code

For most of the numerical computations performed in this thesis the fermionic many body code *Quanty* was used [Haverkort et al., 2012]. It allows the user to express operators and wavefunctions directly in second quantized manner in terms of the creation and annihilation operators $a_i^\dagger, a_i$. As we will use *Quanty* only for exact diagonalization, let us roughly sketch the underlying Lanczos-algorithm.
When working with multiple particles the dimension of the multi-particle Hilbert space scales exponentially and the problem becomes computationally intractable very fast. For example, the Hilbert space of three spin-up and three spin-down particles expressed on a basis of 15 orbitals (e.g. the five lowest shells of the harmonic oscillator) has already dimension $\binom{15}{3}^2 \sim 2 \cdot 10^5$. Furthermore, physical Hamiltonians are oftentimes sparse with a lot of vanishing matrix elements due to symmetries. For example, expressed on the same basis the two-particle interaction term in eq. (3.17) contains only $\sim 9\%$ non-zero elements. This means that dense methods are not only computationally hard but also inefficient. Instead of diagonalizing the Hamiltonian directly on the full Hilbert-space, the idea of the Lanczos-algorithm is to only use a much smaller Krylov-subspace $\mathcal{K}_n$. This space is spanned by a sequence of n vectors generated by acting multiple times with the operator H on a starting vector $|\psi_0\rangle$,

$$\mathcal{K}_n = \text{span}\{|\psi_0\rangle, H|\psi_0\rangle, H^2|\psi_0\rangle, ...H^{n-1}|\psi_0\rangle\}. \tag{3.18}$$

The goal is now to continue this sequence until the next vector $H^n |\psi_0\rangle$ is fully linearly dependent on the previous vectors, in other words, once $\mathcal{K}_n$ is invariant under action of H. Assuming that the ground state $|\psi_g\rangle$ of H has a finite overlap with the initial state $|\psi_0\rangle$, $|\psi_g\rangle$ can now be accurately computed by diagonalizing H on $\mathcal{K}_n$. In practice, one directly orthonormalizes the vectors as they are generated, such that the Krylov-sequence becomes an orthonormal basis of the subspace. Since the employed Gram-Schmidt decomposition is prone to numerical errors, one usually only generates a couple of hundred Krylov-vectors to avoid loss of orthonormality. The algorithm is then restarted with the lowest eigenvalue-eigenvector obtained from diagonalizing H on the Krylov-subspace just found. Since eigenvectors corresponding to the eigenvalues of largest magnitude converge first, it is beneficial to shift the Hamiltonian by the largest eigenvalue at this point. Practically, the procedure is stopped once a convergence condition, e.g. regarding the variance of the found states, is met. Starting with several orthogonal vectors allows for the computation of the lowest part of the spectrum.

3.4 The two-particle problem revisited

To benchmark our numerical approach we once more consider the two-particle problem for which solutions can be computed accurately. Furthermore, computing the two-particle ground state energy from eq. (3.17) is necessary to fix the bare coupling constant g via the ground state renormalization scheme presented earlier. For now we are only interested in the left part of the spectrum, i.e. in the region $\ln(d/a) < 1$. Fig. 3.4 shows the numerical results obtained from solving eq. (3.17) using *Quanty* for a range of reasonable basis sizes of 5, 6, 8 and 10 shells (i.e. 30, 42, 72 and 110 spin-orbitals, respectively). A qualitative picture is given in Fig. 3.4a and b. As a measure of accuracy we compare the energy of the first excited state with the exact solution in Fig. 3.4c. The deviation is given by $|E_1 - E_1^{exact}|/|E_1^{exact} - 3|$, i. e. we measure the energy with respect to the states energy at $a \to \infty$. As a second measure of accuracy we compute the overlap of the numerical ground state with the exact ground state obtained from numerical diagonalization of the relative motion Hamiltonian with a high cut-off of $K_c = 500$. To expand the relative motion state in second quantization (or in the lab-frame) we use the relation

$$\begin{aligned} &\frac{1}{\sqrt{2}} |\underbrace{k=0, m=0}_{\text{com}}; \underbrace{K, m=0}_{\text{rel}}\rangle \left(|\uparrow\downarrow\rangle - |\downarrow\uparrow\rangle\right) \\ &= 2^{-K} \sum_{m=-K}^{m=K} \sum_{k_1=0}^{K^*} \epsilon_{k_1 k_2} \left[\binom{K}{k_1}\binom{K}{k_2}\right]^{\frac{1}{2}} \left\{a^\dagger_{k,m,\uparrow} a^\dagger_{k_2,-m,\downarrow} - a^\dagger_{k,m,\downarrow} a^\dagger_{k_2,-m,\uparrow}\right\} |0\rangle \,, \end{aligned} \tag{3.19}$$

where $K^* = \lfloor \frac{K-|m|}{2} \rfloor$, $k_2 = K - |m| - k_1$ and $\epsilon_{k_1 k_2} = (1 + \delta_{k_1 k_2})^{-1}$. The results for the overlap presented in Fig. 3.4c are consistent with the findings in Fig. 3.3 when considering that a single-particle basis of $2K_c + 1$ shells is need to fully capture the

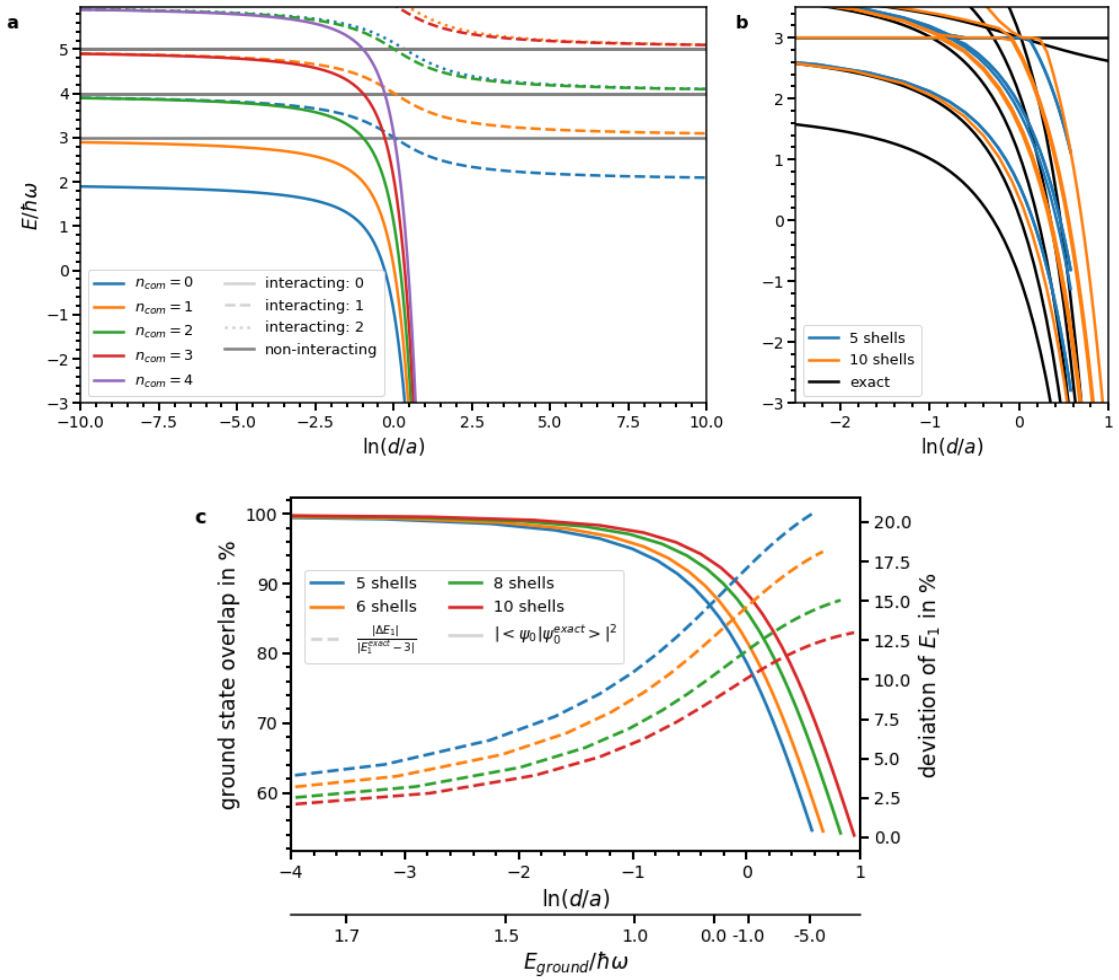

Figure 3.4: **Full two-particle energy spectrum**
Numerical and exact solution for two interacting particles in a 2D isotropic harmonic trap. The coupling constant is renormalized by matching the numerical to the exact ground state energy. **a** - exact spectrum including non-interacting states and center-of-mass motion. Center-of-mass excitations beyond shell number $n_{com} = 5$ are omitted for clarity. **b** - detailed view of the part of the spectrum where atoms are not too deeply bound. Besides the exact solution the numerical solution for different sizes of the single-particle basis is plotted. **c** - Overlap of the numerically obtained ground state with the exact solution (obtained by numerically diagonalizing the relative motion Hamiltonian with a high cut-off of $K_c = 500$ and expanding in lab-frame coordinates) on the left axis. Deviation between the numerical and exact solution for the first excited state as measured from its value at $\ln(d/a) = -\infty$ on the right axis.

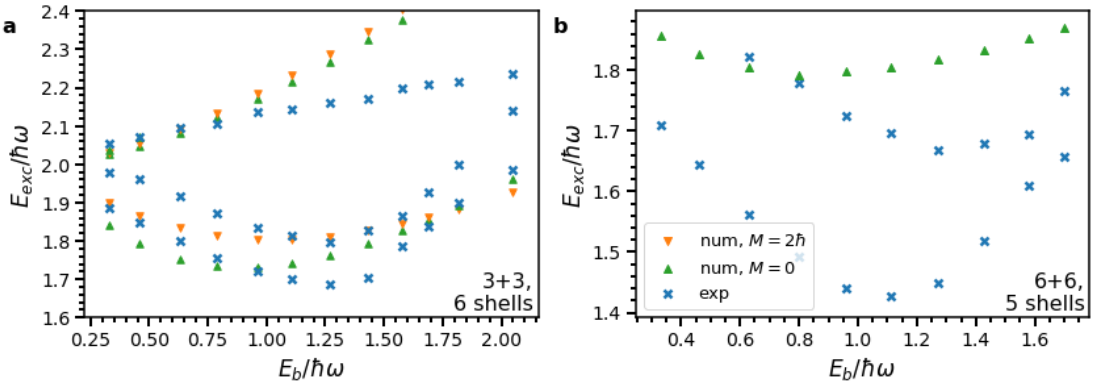

Figure 3.5: **Closed-shell excitation spectrum for $3+3$ and $6+6$ atoms** Comparing the numerically computed excitation spectrum with experimental data [Bayha et al., 2020]. The coupling constant is renormalized by matching the numerical ground state energy to the experimental data for the two-particle problem. The bound state energy E_b is defined as $E_b = 2 - E_{\text{ground}}$. M is the total angular momentum. **a** - spectrum for three spin-up and three spin-down atoms. Computed on a single particle basis of 6 shells. **b** - spectrum for six spin-up and six spin-down atoms. Computed on a single particle basis of 5 shells. The numerical solution is only purely converged. Both cases represent a closed shell configuration of the two-dimensional isotropic harmonic oscillator.

relative motion state in eq. (3.19). To obtain results with error of less then 10 %, a large single-particle basis of 110 spin-orbitals is needed. Already for the two particle problem this leads to long computation times.

3.5 Precursor of the Higgs Mode

Let us conclude this chapter by finally applying our numerical approach to a recent experimental measurement comprising more than only two particles. In [Bayha et al., 2020] the authors experimentally investigate the emergence of a quantum phase transition from the normal to the superfluid phase occurring in a balanced mesoscopic systems of 3+3 or 6+6 (number spin-up + spin-down particles) ^{6}Li atoms, respectively. All experimental results are parameterized by the two-body binding energy. We therefore renormalize the coupling constant by matching the numerical solution of the ground state energy to the experimental result in the two-body case. With the mapping between the coupling constant and the two-body binding energy at hand we go on and diagonalize eq. (3.17) using *Quanty*. The numerical results together with the experimental data are presented in Fig. 3.5. In the 3+3 case the experimental spectrum is qualitatively well described, with deviations around $5\% - 20\%$. This is roughly what we would expect at the very least from the two-body result in Fig. 3.4c. Since they use a harmonic trap with

aspect ration $\omega_z/\omega \sim 6.8$ some of the errors towards the strong binding energy end can be attributed to the loss of 2D-ness in that regime. This can qualitatively be anticipated from Fig. 2.1 which shows the exact and 2D-solution for a trap of aspect ratio 10.
The excitation spectrum in the 6+6 case could not be predicted to a satisfactory degree. Reasons for this might be found in the smaller single-particle basis consisting of only 5 shells as opposed to the 6 shells that were used for the 3+3 calculation. Sacrificing the additional shell was necessary to obtain a solution in any reasonable computational time. In fact, even with the smaller basis set the 6+6 calculation did only poorly converge. Taking a look at eq. (3.18) we see that the Krylov-space on which the Hamiltonian is eventually diagonalized heavily depends on the starting vector. Especially in large Hilbert spaces, and with a dimension of $\binom{15}{6}^2 \sim 25 \cdot 10^6$ that's truly the case here, the overlap of the starting vector with the true ground state will very easily tend to zero. Hence, in the future the convergence might be significantly improved by taking a good guess for the starting vector. [4]

[4]Currently the computation is started with the non-interacting ground and first excited states.

4 Rotating Traps: A path to Quantum Hall Physics

It has long been known that particles trapped in a two-dimensional harmonic potential under rotation are formally equivalent to electrons moving in a plane perpendicular to an external magnetic field. The latter situation gives rise to the integer, and in the presence of interactions, the fractional quantum hall effect. Due to the equivalence of both systems, ultracold atoms offer an intriguing opportunity to study highly-entangled fractional quantum hall states. Several protocols for the creation of such states have been proposed for bosonic [Popp et al., 2004] and fermionic systems [Palm et al., 2020].
The reminder of this thesis will deal with the experimental realization of the scheme proposed by [Palm et al., 2020]. First let us very briefly present the quantum hall effect. We will then introduce the equivalence of the cyclotron motion of electrons and the rotating trap, before we discuss the theoretical results found in [Palm et al., 2020]. We will then proceed with studying the system in a experimentally realistic setting. Finally the experimental methods and the optical setup is presented.

4.1 The Quantum Hall Effect in a nutshell

The classical quantum Hall effect occurs when a current I flowing through an electrical conductor is subject to a magnetic field B perpendicular to the conductor. To maintain its original direction an electric field E transverse to the current needs to build up, exactly balancing out the Lorentz force from the magnetic field component. The quotient I/E defines the Hall-, or transverse, resistivity ρ_{xy} which is proportional to the applied magnetic field. The quantum analog of this effect was first discovered in 1980 by Klitzing et al. [1980]. At low temperatures and high magnetic field the Hall resistivity becomes quantized and the formation of plateaus of constant resistance can be observed. The center of these plateaus, on which one finds a constant resistivity of $\rho_{xy} = \frac{2\pi\hbar}{e^2}\frac{1}{\nu}$, occur at magnetic fields $B = \frac{2\pi\hbar}{e}\frac{n}{\nu}$. Since the filling fractions ν are integers, the effect was termed the integer quantum hall effect. Fig. 4.1 shows a measurement taken in a sample displaying the quantization of the Hall-resistivity at both integer and rational filling fractions.
A theoretical explanation for the integer quantum Hall effect can be given by considering the motion of an electron in an external magnetic field. The Hamiltonian of the electron in terms of the canonical momentum operator $\boldsymbol{p}$ and the vector potential

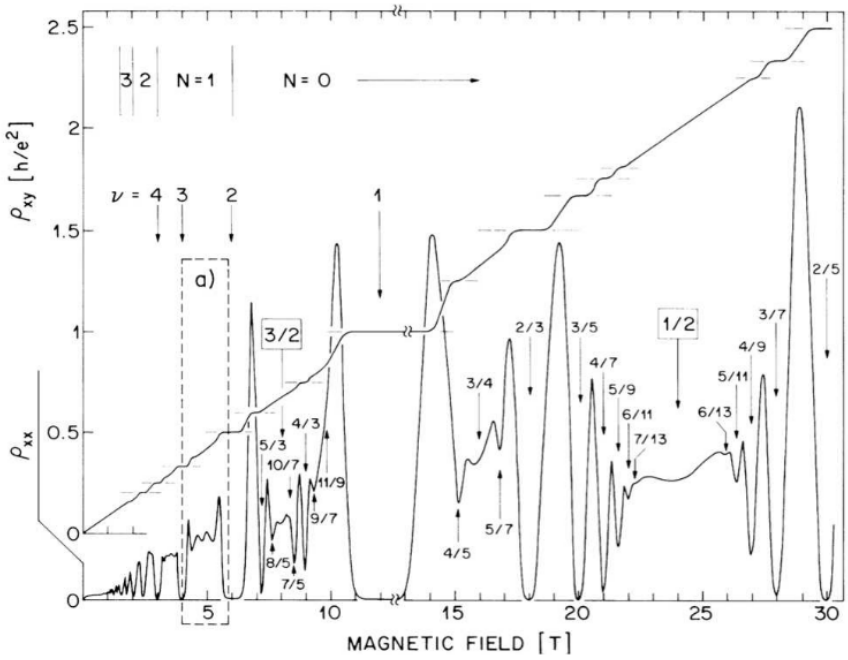

Figure 4.1: **The integer and fraction Quantum Hall Effect**
At low temperature and high magnetic fields plateaus appear in the transverse, or Hall-resistivity ρ_{xy}. The longitudinal resistivity ρ_{xx} jumps to finite values during transitions between plateaus. Taken from [Tong, 2016].

$\boldsymbol{A}$ is given by

$$H = \frac{1}{2m}(\boldsymbol{p} + e\boldsymbol{A})^2. \tag{4.1}$$

Assuming the magnetic field to be aligned in z-direction, we only consider motion in the x-y-plane. With the vector potential chosen in Landau gauge, $\boldsymbol{A} = xB\boldsymbol{e}_y$, it is convenient to make the ansatz $\psi(x, y) \sim e^{iky} f_k(x)$ which decouples the x- and y-motion. The Hamiltonian can then be rearranged to

$$H = \frac{p_x^2}{2m} + \frac{m\omega_B^2}{2}(x + kl_B^2)^2, \quad l_B = \sqrt{\frac{\hbar}{eB}},\ \omega_B = \frac{eB}{m} \tag{4.2}$$

which we recognize as a harmonic oscillator shifted along the x-axis by kl_B^2, where k is the momentum in y-direction. Hence, we find the energy spectrum to be given by $E_n = \hbar\omega_B(n + 1/2)$, where each level is hugely degenerate with respect to the motion in y-direction. These are the famous Landau levels.
Let us briefly compute the density of states in one such level. To this end we consider a square in the x-y-plane of length L. Imposing periodic boundary conditions in y-direction restricts the possible wavevectors k to $\frac{2\pi}{L}m, m \in \mathbb{Z}$. Cutting this off at N yields $N + 1$ oscillators spaced over a distance $N\frac{2\pi}{L}l_B$ on the x-line. By setting this

equal to L we estimate the density of states per Landau level to be $n_L = \frac{1}{2\pi l_B^2} = \frac{eB}{2\pi\hbar}$. Modeling the electrons in the conductor as a non-interacting Fermi-gas with density n, we find that they occupy $\nu = n/n_L$ Landau levels which depends inversely on the magnetic field via n_L. Exactly at an integer filling fraction, i.e. when ν Landau levels are completely filled, we recover the magnetic field $B = \frac{2\pi\hbar n}{e\nu}$ at which the center of the plateaus occur.
Two years after the discovery of the integer quantum Hall effect plateaus at rational filling fractions $\nu \in \mathbb{Q}$ were observed, which was subsequently called the fractional quantum Hall effect [Willett et al., 1987] (see Fig. 4.1). The additional plateaus hint at additional states in the spectrum that were previously hidden. In fact, we have so far considered the electrons to be non-interacting. It is however reasonable to assume that the Coulomb repulsion between the electron will lift the huge degeneracy of the Landau levels, leading to new states within the Landau levels at which additional plateaus can appear. We will learn more about these fractional quantum hall states in the context of the rotating trap.
Finally, the interested reader is referred to Tong [2016] for a much more detailed discussion of the physics of the quantum Hall effect.

4.2 The Rotating Harmonic Trap

Let us return to our ultracold atoms and consider again the Hamiltonian eq. (3.1) describing particles interacting in a two-dimensional isotropic harmonic trap. However, this time we take a new perspective on the problem and place ourselves in a frame of reference rotating with angular velocity Ω with respective to the lab-frame. Since the angular momentum operator $M_i = -i\frac{\partial}{\partial\theta_i}$ generates rotations of the coordinates of the i-th particle, we write down a unitary transformation like

$$U = e^{-iM\Omega t}, M = \sum_i M_i. \tag{4.3}$$

Let's denote the regular lab-frame operators and states by $\mathcal{O}'$ and $|\psi'\rangle$. We can then smuggle in the unitary defined above without effecting any physical observables, i.e. expectation values, if we define

$$|\psi\rangle = U^\dagger |\psi'\rangle , \quad \mathcal{O} = U\mathcal{O}'U^\dagger, \tag{4.4}$$

which leaves all expectation value invariant, $\langle\psi|\mathcal{O}|\psi\rangle = \langle\psi'|\mathcal{O}'|\psi'\rangle$. We can see how the new states evolve in time by evaluating the time-dependent Schrödinger equation in the lab-frame

$$i\partial_t |\psi\rangle = \left(U^\dagger H' U - M\Omega\right)|\psi\rangle \equiv H|\psi\rangle , \tag{4.5}$$

where H' is the Hamiltonian in the lab-frame.[1] Since the whole Hamiltonian including the s-wave interaction is rotationally invariant we have

$$H = H' - \Omega M = \sum_i \left(-\frac{1}{2}\Delta_i + \frac{1}{2}\boldsymbol{x}_i^2 - \Omega M_i \right) + g \sum_{i<j} \delta^{(2)}(\boldsymbol{x}_i - \boldsymbol{x}_j). \tag{4.6}$$

For now let us assume that the particles are non-interacting, i. e. we set $g = 0$. We note that the harmonic oscillator states eq. (3.5) remain eigenstates of the new Hamiltonian allowing us to directly read off the single-particle spectrum

$$E = \hbar\omega(2k + |m| + 1) - \Omega m \equiv \hbar\omega(2k + 1 + |m| - m + \alpha m), \tag{4.7}$$

where the dimensionless parameter of rotation $\alpha = 1 - \frac{\Omega}{\omega}$ was introduced. As depicted in Fig. 4.2(insets) the inverted-tree-like energy spectrum of the harmonic oscillator starts to fall over to the side of positive angular momentum when the speed of rotation is increased. In the $\alpha = 0$ limit the so called deconfinenment is reached and the spectrum is formed by horizontal levels of, in principle, infinite degeneracy. These are once again the Landau levels we have already met in the context of the quantum Hall effect! In fact the equivalence becomes more apparent when considering the single-particle Hamiltonian in a rearranged way (and expressed in physical units),

$$H = \frac{1}{2m}(\boldsymbol{p} - m\Omega \boldsymbol{e}_z \times \boldsymbol{x})^2 + \frac{m}{2}(\omega^2 - \Omega^2)\boldsymbol{x}^2, \tag{4.8}$$

where $\boldsymbol{p} = -i\hbar\nabla$ is the momentum operator. In the $\alpha = 0$ limit the centrifugal force cancels the confining harmonic potential and only the Coriolis force remains. The coriolis force $-2m\boldsymbol{\Omega} \times \dot{\boldsymbol{x}}$ is equivalent to the Lorentz force $-q\boldsymbol{B} \times \dot{\boldsymbol{x}}$ a particle of charge q experiences in a magnetic field of strength $\boldsymbol{B} = \frac{2m}{q}\boldsymbol{\Omega}$. As in electromagnetism one might introduce an artificial gauge field $\boldsymbol{A} = \frac{m}{q}\boldsymbol{\Omega} \times \boldsymbol{x}$ (with $\boldsymbol{B} = \boldsymbol{\nabla} \times \boldsymbol{A}$) in which the particle seems to move when observed in the rotating frame. For $q = -e$ we precisely recover the Hamiltonian (4.1) of the free electron moving in a magnetic field.[2]

Finally, note that the transformation we just did, i.e. $|\psi\rangle = U^\dagger |\psi'\rangle$ and $\mathcal{O} = U\mathcal{O}'U^\dagger$ does not actually correspond to a change of reference, but rather is a gauge transformation. Intuitively, this can be seen by looking at the angular momentum operator which transforms invariant under U. I.e. a state with angular momentum $\hbar m$ will have the same angular momentum no matter what frame we use. While this is the correct behavior for a gauge transformation it is not what we would expect for a change of reference to a rotating frame, where the angular momentum should be lowered or increased depending on the speed of rotation. Fortunately, we formally

[1] For ease of notation we diverged from the rule $\mathcal{O} = U\mathcal{O}'U^\dagger$ when we labeled the new Hamiltonian by H.

[2] Note however the different choice of gauge. Here the symmetric gauge is chosen, while earlier we chose the Landau gauge.

obtain the same equations (4.6) and (4.8) for the proper change of reference, only that $\boldsymbol{p}$ and M wouldn't label the kinetic (angular) momentum operator but rather the canonical ones (for the gauge transformation that's the same) [Anandan and Suzuki, 2003]. Which way of performing the 'change of reference' is in the end a matter of taste.

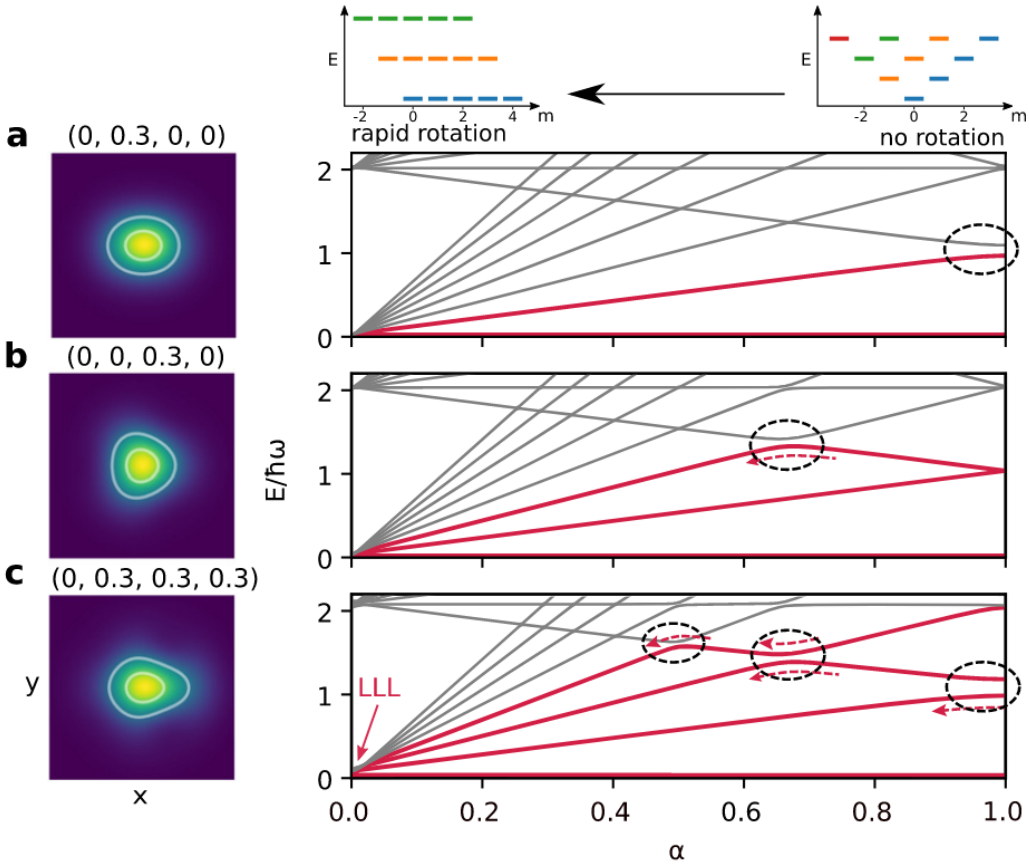

Figure 4.2: **Single-particle spectrum of the rotating harmonic trap**
The inverted tree-like energy structure of the harmonic trap (top inset, right) transforms into degenerate Landau levels when viewed from a rotating frame (top inset, left). Perturbations of higher azimuthal-order lead to the opening of gaps in the spectrum and can be used to adiabatically transfer atoms into the lowest Landau level (LLL) via the single-particle paths highlighted in red. The experimental trapping potentials corresponding to these perturbations are shown in the left column where the values in the bracket indicate the perturbation strengths $(\epsilon_1, \epsilon_2, \epsilon_3, \epsilon_4)$. **a** - pure elliptical, **b** - triangular, **c** - composite perturbation. The transition of the perturbed spectrum is only sketched. Taken from [Palm et al., 2020].

4.2.1 Perturbations: Opening an adiabatic path to the LLL

From taking a look at the energy spectrum in the deconfinement limit in Fig. 4.2 one might expect that, due to the large degeneracy, the lowest energy eigenstates are predominantly formed in the lowest Landau level (LLL). Even when switching on interactions this shouldn't change drastically as long as the interaction energy remains small compared to the splitting of the Landau levels of $2\hbar\omega$. However, describing the system from a rotating frame of reference is merely a theoretical trick and shouldn't change anything about the actual physics going on. Furthermore, it is neither experimentally possible to measure nor to prepare atoms directly in the rotating frame. So what's the point of the whole equivalence?
When looking closely at the energy spectrum we notice that any state hosted in the LLL will have a potentially arbitrarily large angular momentum. In fact the LLL precisely consists of the state with lowest energy (as seen from the lab-frame) per sectors of non-negative angular momentum. This gives us a clue on how to prepare states in the LLL. We simply need to transfer angular momentum into the system in an adiabatic way such that the system always remains in its ground state. To this end we consider the following class of time-dependent perturbations,

$$V_l(t) = \epsilon_l(r^l e^{il\theta} e^{il\Omega t} + c.c.). \tag{4.9}$$

The potential clearly breaks the rotational symmetry and couples modes which differ in angular momentum by $\pm l$. Its matrix elements in the harmonic oscillator basis (3.5) can be computed directly and are given by [Srivastava et al., 2003]

$$\begin{aligned}\langle k'm'|r^l e^{il\theta}|k,m\rangle = \delta_{m',m+l}\Gamma(\mu+1)(-1)^{k+k'}\sqrt{\frac{k!k'!}{(k+|m|)!(k'+|m'|)!}} \\ \cdot \sum_{n=0}^{\min(k,k')} \binom{\mu-|m|}{k-n}\binom{\mu-|m'|}{k'-n}\binom{\mu+n}{n},\end{aligned} \tag{4.10}$$

where $\mu = \frac{1}{2}(l+|m|+|m'|)$.
The transformation U precisely cancels the time-dependence of the perturbation, $U^\dagger V_l(t)U = \epsilon_l(r^l e^{il\theta} + c.c.)$ and the perturbed problem can be solved straightforwardly in the frame rotating with the speed Ω. [3] The numerically computed energy spectrum for different perturbations is shown in Fig. 4.2a-c versus the rotation parameter α. The coupling of states of different angular momentum leads to the opening of gaps in the spectrum whenever two states cross, that fulfill the selection rule $\Delta m = m' - m = \pm l$. This corresponds to the resonance condition $\Delta E = \hbar\Delta m\Omega$, $|\Delta m| = l$ when viewed from the resting frame. The perturbations can be superimposed to open gaps corresponding to different selection rules simultaneously, cf. Fig. 4.2c. A simple experimental protocol could for example look like this. Starting from a zero angular momentum, closed shell configuration of three

[3] This means for a perturbation rotating with speed $l\Omega$ we go to a frame rotating with Ω.

spin-up and three spin-down atoms populating the first two shells one switches on the $l = 3$ perturbation and slowly increases the speed of rotation. Beyond $\alpha = 0.6$ we have then introduced six quanta of angular momentum into the system and transferred all atoms into the LLL.
Lastly, also some technical remarks about the perturbations eq. (4.9) are in place. Note that beyond $l = 2$ the perturbation leads to a Hamiltonian that isn't bound from below anymore. In fact, the form of the perturbation given here is only approximately true as long as $\epsilon_l R^l \ll 1$ holds for R being the maximal spatial extension of the wavefunctions considered. In that sense the $(l > 2)$-perturbations are always only valid on a finite Hilbert space respecting this condition. At non-zero Ω the overall potential can nevertheless become anti-confining. An instructive example is the case of the elliptical $l = 2$ perturbation which for $\Omega = 0$ and $\epsilon_2 < 2$ (in h.o. units) represents a valid Hamiltonian even in the infinite dimensional limit. However, once the speed of rotation is increased above $\Omega_c = \sqrt{1 - 2\epsilon_2} \approx 1 - \epsilon_2$ the total potential (trap + perturbation + centrifugal force) becomes anti-confining in one axis and the atoms start to escape from the trap. This effect was just recently observed in a rotating Bose-Einstein-condensate by Fletcher et al. [2021].

4.2.2 Switching on Interactions: Renormalization in the Lowest Landau Level

So far we have only investigated the non-interacting case. To see how the picture of the interacting system changes in the rotating frame let us study once more the two-particle problem in relative coordinates. Since all interacting states have zero relative angular-momentum anyway their energy stays unaltered. The other non-interacting states are shifted in energy and form Landau levels just as we already know them from the single particle problem. Fig. 4.3a shows the energy of the two lowest interacting relative motion states. Furthermore, the overlap of the two states with the relative motion $|k = 0, m = 0\rangle$-state is plotted. Since interacting states are a superposition of $|k, 0\rangle$ states, the overlap with $|0, 0\rangle$ gives the overlap with the complete LLL of two particles. We observe that the ground state and the first excited stated are predominantly hosted in the LLL for scattering lengths $d/a \ll 1$ and $d/a \gg 1$, respectively. This tells us that in this regime (provided we don't care about the deeply bound dimer-state for $d/a \gg 1$) we might be able to effectively describe the physics at low energies, i.e. $< 2\hbar\omega$ with respect to the non-interacting ground state, by only considering the LLL, even when dealing with more than two particles. We further note that at small interaction energies $\Delta E = E - \hbar\omega$ the solution of eq. (3.9) is approximately given by [4]

$$\Delta E \approx \frac{2\hbar\omega}{2\ln(d/a) + \gamma}, \quad |\ln(d/a)| \gg 0.289. \tag{4.11}$$

[4] Using that $\psi(x) = -\gamma - \frac{1}{x} + O(x)$.

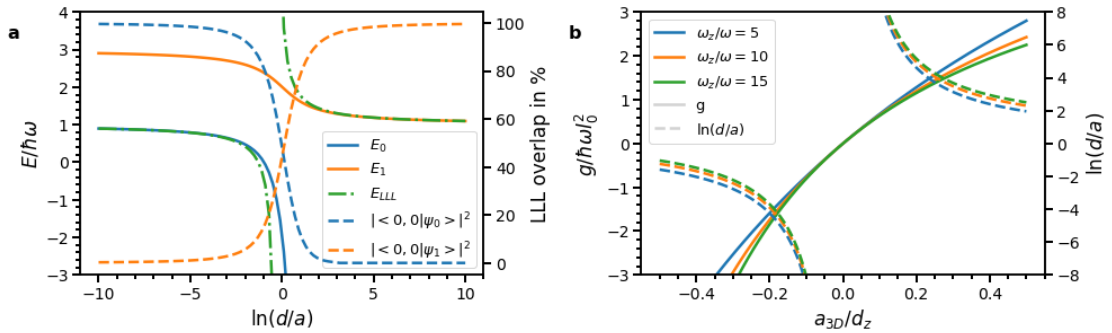

Figure 4.3: **Interacting states and renormalization in the LLL**
a - The lowest two interacting states for the relative motion of two particles interacting in a 2D isotropic harmonic trap. Furthermore, the approximative solution E_{LLL}, eq. (4.11), is plotted which is valid for small interaction energies. Besides the energies also the overlap of the states with the LLL is depicted on the right axis. **b** - The value of the coupling constant in terms of the 3D-scattering length for different aspect ratios is plotted on the left axis. The corresponding 2D interaction strength is depicted on the right axis.

In total, we find that in the deconfinement-limit the energy spectrum below $2\hbar\omega$ w.r.t. the non-interacting ground state consists of only two, infinitely-degenerate manifolds, the non-interacting states at the vacuum energy and the interacting states with energy $\hbar\omega\Delta E$ above that, both of them being hosted in the LLL. As already stressed above these states correspond to the states of lowest energy from sectors with non-negative angular momentum in the lab-frame.

For two particles, the LLL can be spanned by the states $|0, M\rangle_{\text{com}} \otimes |0, m\rangle_{\text{rel}}$. Remarkably, these are already solutions to the Hamiltonian (3.1) with energy $2\hbar\omega$ for relative angular momentum $m \neq 0$ and $\hbar\omega(2 + g/2\pi)$ for the $m = 0$ states. By matching this solution with the previous one we can identify the bare coupling constant in terms of the 2D- and 3D-scattering length, respectively

$$g/\hbar\omega l_0^2 = \frac{4\pi}{\ln(d/a) + \gamma} \approx \frac{4\pi}{\ln(0.513n) + \sqrt{\pi}\frac{d_z}{a_{3D}}} \overset{|\frac{a_{3D}}{d_z}| \ll \frac{\sqrt{\pi}}{\ln(0.513n)}}{\approx} 4\sqrt{\pi}\frac{a_{3D}}{d_z}. \quad (4.12)$$

Here g is expressed in physical units and $n = \omega_z/\omega$ is the aspect ratio. The coupling constants for different aspect ratios is plotted in Fig. 4.3b. From now on we assume to be always well in the regime $|\frac{a_{3D}}{d_z}| \ll \frac{\sqrt{\pi}}{\ln(0.513n)} \sim 1$ and $g \ll 2\pi$. Since we neglect the deeply bound dimer-state this is also precisely the regime in which we expect the purely two-dimensional treatment to be accurate. With these assumptions in mind we will restrict ourselves to the lowest Landau level for the remainder of this section. Finally, note that the coupling constant is then independent of any angular-momentum cut-off!
Choosing to work in the LLL greatly simplifies the evaluation of the interaction and perturbation matrices. Neglecting the vacuum energy, the Hamiltonian (4.6)

reduces to

$$H = \alpha \sum_{m\sigma} a^\dagger_{m,\sigma} a_{m,\sigma} + g \sum_{M=0}^{\infty} \sum_{m,m'}^{M} h_{M,m,m'} a^\dagger_{m',\uparrow} a^\dagger_{M-m',\downarrow} a_{m,\downarrow} a_{M-m,\uparrow} + \sum_{l} \epsilon_l \sum_{m,\sigma} v_{l,m} (a^\dagger_{m+l,\sigma} a_{m,\sigma} + h.c.) \quad , \tag{4.13}$$

where $a^\dagger_{m,\sigma}$ creates a particle in the $|0, m, \sigma\rangle$ state and $m \geq 0$, $\sigma \in \{\uparrow, \downarrow\}$. The matrices h and v_l are given by

$$h_{M,m,m'} = \frac{M!}{2\pi 2^M \sqrt{m!m'!(M-m)!(M-m')!}} \tag{4.14}$$

$$v_{l,m} = \sqrt{\frac{(m+l)!}{m!}}. \tag{4.15}$$

4.2.3 Fractional Quantum Hall States

We have seen how for the two-particle problem the eigenstates formed in the LLL took the simple form $|0, M\rangle_{\text{com}} \otimes |0, m\rangle_{\text{rel}} \sim (z_1 + z_2)^M (z_1 - z_2)^m e^{-\frac{1}{2}(r_1^2 + r_2^2)}$, with the complex coordinates $z_i = x_i + iy_i$. For repulsive interactions the ground state manifold is given by the $m \neq 0$ solutions for which the wavefunction becomes zero when the position of the particles coincides. The particles, therefore, never see each other and cannot feel any repulsion from the contact interaction. Interestingly, the argument can be extended to multiple particles. Let us assume $\alpha = 0$ and introduce the new complex coordinates $z_i = x_i + iy_i$ and $\tilde{z}_i = \tilde{x}_i + i\tilde{y}_i$, labeling the spin-up and the spin-down particles, respectively. In the case of a spin-polarized system with only one spin component, say $N_\uparrow$, an extension of the two-particle ground state was proposed by Laughlin [1983],

$$\Psi_n(z_1, ..., z_{N_\uparrow}) \sim \prod_{i<j}^{N_\uparrow} (z_i - z_j)^m, \tag{4.16}$$

where the Gaussian envelope was omitted. This state occupies the LLL up to angular momentum $m_{max} = (N_\uparrow - 1)m$ and has total angular momentum $M = \frac{mN_\uparrow}{2}(N_\uparrow - 1)$. Note how the vortices $(z_i - z_j)^m$ carve out a region around each particle. In the presence of a general repulsive interaction this helps to reduce the energy of the state. For systems of small particle number one finds a high overlap between the Laughlin-wavefunction and the numerically found ground state. While the overlap is expected to vanish for large systems it is still instructive to study the Laughlin-state in the context of the fractional quantum Hall effect, where the electrons interact via the Coulomb repulsion. In fact, we can compute the filling fraction of the Laughlin-states by estimating their size by the largest occupied LLL state. For N particles we find $R = \sqrt{2m_{max} l_B^2} \approx \sqrt{2Nml_B^2}$ corresponding to an area $A = \pi R^2 = 2\pi N m l_B^2$,

where we used that $l_0^2 = 2l_B^2$ (since $\omega_B = 2\omega$). This results in a particle density of $n_m = \frac{1}{2\pi l_B^2}$ which exactly matches the electron density n at magnetic field $B = \frac{2\pi\hbar n}{e\nu}$, with $\nu = \frac{1}{m}$. These correspond to the centers of some of the plateaus we find in the fractional quantum Hall effect! Furthermore, we can compare the particle content of the Laughlin-state with that of a partially field LLL for the area A. One finds that the Laughlin-state contains the same particle density as a partially filled LLL with filling fraction $\nu = \frac{1}{m}$. For $m = 1$ we recover the fully filled LLL. The Laughlin-wavefunction then only contains vortices of order one which stem from the Paul-exclusion principle and correspondingly describes a Fermi-sea of N particles. Note also that, at least for fermions, the spatial wavefunction needs to be antisymmetric in the case of a one-component gas ruling out all even m. In the case of ultracold atoms we note that the Laughlin-states become exact ground states due to the pure s-wave interaction (at $g > 0$).
The Laughlin states were further generalized by Halperin [1983] to contain another spin-component

$$\Psi_{(m,m,n)}(z_1, ..., z_N, \tilde{z}_1, ..., \tilde{z}_N) \sim \prod_{i<j}^{N}(z_i - z_j)^m \cdot \prod_{i<j}^{N}(\tilde{z}_i - \tilde{z}_j)^m \cdot \prod_{i,j}^{N}(z_i - \tilde{z}_j)^n, \quad (4.17)$$

where we already restricted ourselves to the balanced case with $N = N_\uparrow = N_\downarrow$. These states have maximum angular momentum $m_{max} = (N-1)m + nN$, total angular momentum $M = mN(N-1) + nN^2$ and filling fraction $\nu = 2/(m+n)$. They are antisymmetric with respect to exchange of particles of like spin for uneven m. However, in general they do not obey the correct symmetry properties when one exchanges spin-up and spin-down particles. An exception to this are states with $m = n$ and m odd, which represent a fully antisymmetric orbital wavefunction. Together with the symmetrized version of the spin-wavefunction $|\uparrow ... \uparrow\downarrow ... \downarrow\rangle$ the total state has the correct symmetry. Due to the symmetric spin-wavefunction this state has maximum total spin S^2, representing a ferromagnet with $S_z = 0$.
In general the Halperin-states should be seen as some kind of shorthand notation from which the fully antisymmetric states are obtained by application of an antisymmetrization procedure. In second quantization, for example, one could simply expand the product in eq. (4.17) and replace each term by the corresponding Slater-determinant $\mathcal{N}_{\{m\},\{\tilde{m}\}} a^\dagger_{m_1,\uparrow} ... a^\dagger_{m_N,\uparrow} a^\dagger_{\tilde{m}_1,\downarrow} ... a^\dagger_{\tilde{m}_N,\downarrow}$, with the normalization $\mathcal{N}_{\{m\},\{\tilde{m}\}} = \sqrt{\prod_i \pi m_i! \prod_j \pi \tilde{m}_j!}$.
With this understanding of the Halperin-states one finds that only the $\Psi_{(n+1,n+1,n)}, n$ even, states form a spin-singlet with total spin $S^2 = 0$. $\Psi_{(1,1,0)}$ for example denotes a product of two Fermi-seas with total spin $S^2 = 0$. A spin-singlet state around $\nu = \frac{1}{q}$, i.e. $\Psi_{(q,q,q)}$, was identified by Yoshioka [1998],

$$\Psi_q^{(r)} = \Psi_{(q,q,q)} \mathrm{per}|M^{(r)}|, \quad (4.18)$$

where the additional factor $\mathrm{per}|M^{(r)}|$ is the permanent of the matrix $M_{ij}^{(r)} = (z_i - \tilde{z}_j)^r$. It introduces another r quanta of angular momentum in to the state, resulting

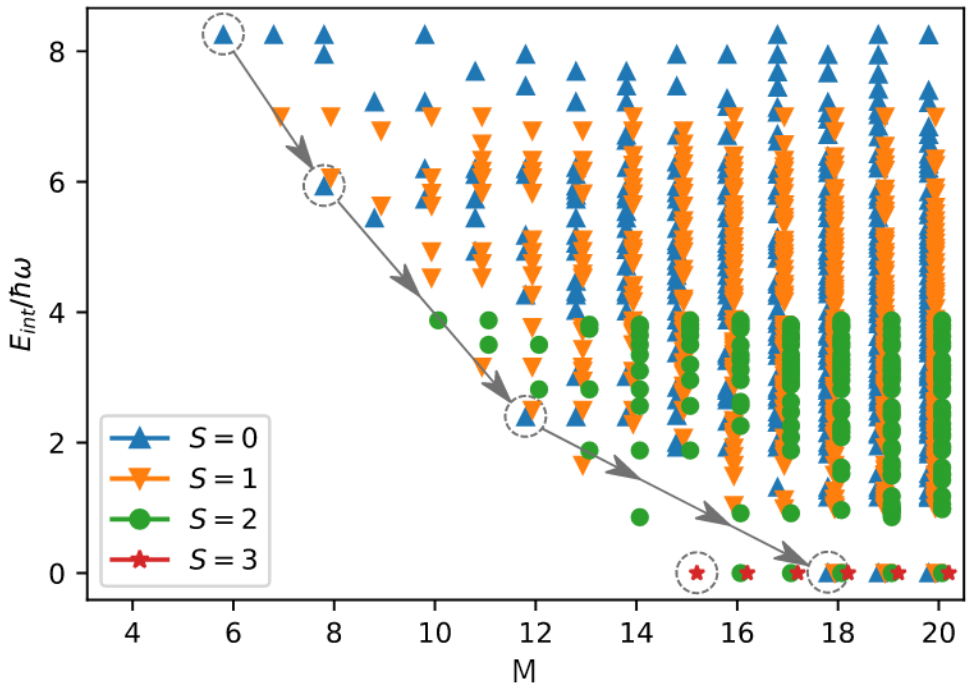

Figure 4.4: **Energy spectrum of $3+3$ particles in the deconfinement-limit** The numerically computed Yrast-spectrum of a system of $3+3$ particles. The computation is done in the deconfinement limit and hence the resulting spectrum can be scaled to arbitrary interaction strengths, here $\eta = g/4\pi = 1$. The first states with vanishing interaction energy appear in the $(S = 3)$-channel at angular momentum $M = 15$. For higher angular momentum also channels with lower spin host a non-interacting state. For non-zero α all states would shift in energy according to their angular momentum content. Taken from [Palm et al., 2020].

in $m_{max} = (N-1)m + nN + r$ and total angular momentum $M = mN(N-1) + nN^2 + rN$. Note that the contribution of r to m_{max} does not scale with the particle number. Hence, for large N it will have a filling fraction very close to $\frac{1}{q}$. This suggests that the state can be seen as an excitation on top of the ferromagnetic $\Psi_{(q,q,q)}$ state.

FQH-states in the Rotating Trap

Palm et al. [2020] have conducted a numerical study for the case of a balanced mix of $3+3$ atoms in a rotating harmonic trap. They solved the Hamiltonian (4.6) in the deconfinement-limit on a LLL-basis. Since in this case all terms other than the contact interaction vanish, the results are independent of the interaction strength (however, still $g > 0$). By computing the overlap of the numerical eigenstates with the states eq. (4.17) and (4.18) a series of fractional quantum Hall states could be identified. The energy spectrum they obtain is shown in Fig. 4.4 where the iden-

tified FQH-states are highlighted. First notice how the interaction is completely suppressed in the $S = 3$ channel. The first ground state at $M = 15$ exactly corresponds to $\Psi_{(1,1,1)}$ representing a ferromagnetic state. The most interesting states however appear in the $S = 0$ channel. Starting from the $\Psi_{(1,1,0)}$ state at $M = 6$ one finally reaches the first non-interacting state at $M = 18$. This is the $\Psi_1^{(1)}$ state, which how further analysis reveals, can be identified as a Skyrmion.

What is a Skyrmion?

Skyrmions are commonly found as excitations on top of ferromagnetic states. They can be thought of as quasi-particles featuring a long-range spin texture. While locally preserving the ferromagnetic correlations, i.e. a parallel orientation of the spins, the Skyrmion excitation also hosts reversed spins on longer scales. Hence the Skyrmion state can be distinguished from the other FQH-states by analyzing its correlations. Palm et al. [2020] conduct a quantitative analysis by employing the second order correlation functions

$$g^{(2)}_{\sigma_1,\sigma_2}(\boldsymbol{x}_1, \boldsymbol{x}_2) = \frac{\langle \Psi^\dagger_{\sigma_1}(\boldsymbol{x}_1)\Psi^\dagger_{\sigma_2}(\boldsymbol{x}_2)\Psi_{\sigma_1}(\boldsymbol{x}_1)\Psi_{\sigma_2}(\boldsymbol{x}_2)\rangle}{\langle \Psi^\dagger_{\sigma_1}(\boldsymbol{x}_1)\Psi_{\sigma_1}(\boldsymbol{x}_1)\rangle \langle \Psi^\dagger_{\sigma_2}(\boldsymbol{x}_2)\Psi_{\sigma_2}(\boldsymbol{x}_2)\rangle}, \tag{4.19}$$

where $\Psi^\dagger_\sigma(\boldsymbol{x})$ creates a particle at site $\boldsymbol{x}$ with spin σ. This spin-resolved correlation function tells us whether finding a particle at site $\boldsymbol{x}_1$ with spin σ_1 correlates ($g^{(2)} > 1$) or anti-correlates ($g^{(2)} < 1$) with finding a spin σ_2 particle at site $\boldsymbol{x}_2$. However, instead of repeating the findings of the authors here we instead want to paint a more qualitative picture. To this end we compute the optimal configurations of the spin-resolved wavefunction for different states, i.e. we seek the configurations $\boldsymbol{z}$ and $\tilde{\boldsymbol{z}}$ that maximize $|\Psi(\boldsymbol{z}, \tilde{\boldsymbol{z}})|^2$. Note that for a spin-resolved measurement the correct probability distribution is already given by eq. (4.17) and (4.18) provided that we have m odd. The resulting configurations for the product state $\Psi_{(1,1,0)}$, the ferromagnetic $S = 3, M = 15$ ground state $\Psi_{(1,1,1)}$ and the $S = 0, M = 18$ Skyrmion $\Psi^{(1)}_{(1,1,1)}$ in the case of $N_\uparrow = N_\downarrow = 8$ particles are depicted in Fig. 4.5. The configurations were obtained by numerical optimization starting from randomly chosen initial configurations. From all runs the best and another interesting configuration (with almost the same value of the probability density) was picked, where the latter is shown in the second row in Fig. 4.5.

The state shown in the first column is the simple product state $\Psi_{(1,1,0)}$ corresponding to a Fermi-sea of both components. We expect the particles of like spin to separate due to the Pauli-exclusion principle (or equivalently the $(m = 1)$-vortices) while particles of unlike spin remain uncorrelated. This is indeed what can be observed in Fig. 4.5. The emerging structure is the lowest Landau level analog of the recently discovered Pauli crystals [Gajda et al., 2016][Holten et al., 2021b]. In the second column the ferromagnetic ground state $\Psi_{(1,1,1)}$ with $S = 3, M = 15$ is shown. We see how now also the particles of unlike spin repel each other. Furthermore, particles of like spin tend to cluster together in long chains. This clustering is significantly

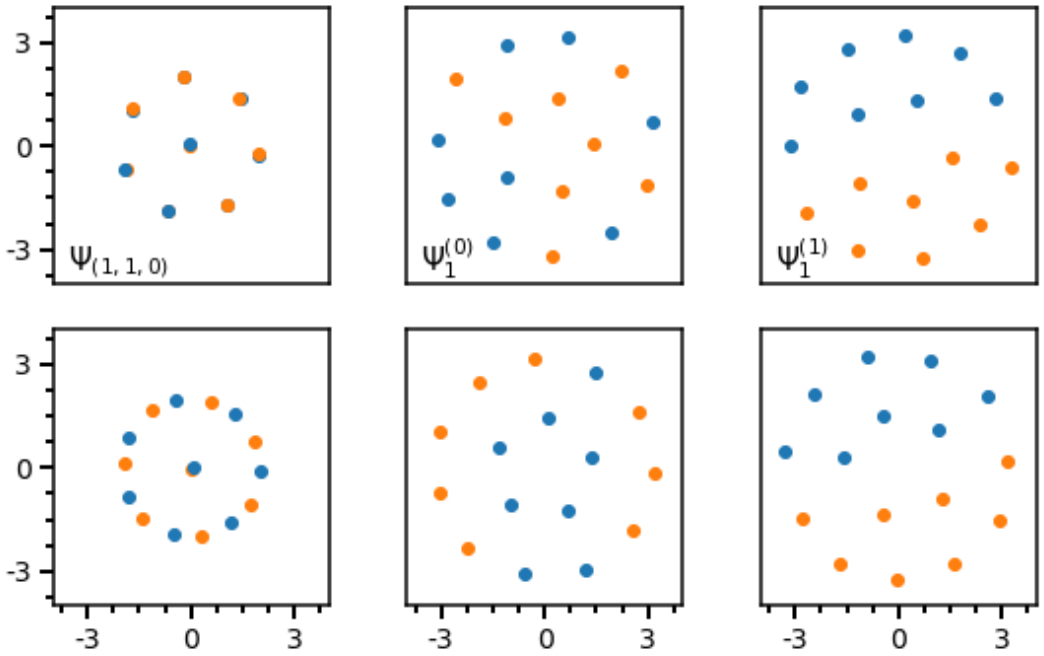

Figure 4.5: **Optimal configurations of FQH-states**
Configurations that maximize the multi-particle probability density for a spin-resolved measurement. The optimal configurations are computed for the product state $\Psi_{(1,1,0)}$ (first column), the ferromagnetic $S = 3, M = 15$ ground state $\Psi_{(1,1,1)}$ (second column) and the $S = 0, M = 18$ Skyrmion $\Psi^{(1)}_{(1,1,1)}$ (third column) in the case of $N_\uparrow = N_\downarrow = 8$ particles. A second optimal configuration with slightly lower probability density is depicted in the lower row. Lengths are measured in harmonic oscillator units l_0.

enhanced in the optimal configurations found for the Skyrmion state. In the third row we can observe that the two spin-species seem to spatially separate from another forming two distinct phases characterized by their spin-projection. Note also how the size of the ferromagnetic and the Skyrmion-state increases as compared to the product state indicating a smaller filling fraction ν. As a final remark keep in mind that the crystalline structures we can observe in Fig. 4.5 only emerge when considering the optimal configurations of the underlying probability distribution. Depending on how sharp the distribution is peaked around these configurations the images obtained by sampling from the probability distribution, either numerically or experimentally, will significantly deviate from the rigid crystalline structure. Since the FQH-states typically describe quantum liquids this is indeed to be expected.

4.2.4 Detection

Based on Fig. 4.5 we can get a feeling about the size of the states we are interested in. For a typical trapping frequency of $\omega = 2\pi \cdot 1$ kHz we obtain a harmonic oscillator length of $l_0 = \sqrt{\hbar/m\omega} \sim 1.3$ µm. On the other hand the atoms are imaged through a high-NA objective with NA = 0.55. For resonant 671 nm light this yields a diffraction-limited resolution of $\delta x = \lambda/2\text{NA} \sim 0.61$ µm. Hence, to obtain high-quality images of the atomic cloud it has to be enlarged before imaging. Luckily, such a magnification mechanism is available with the *wavefunction microscope* [Read and Cooper, 2003]. By switching off the harmonic trap the atomic gas can expand freely. After sufficiently long times the distribution in position space is given by the rescaled initial momentum distribution. In that sense the momentum distribution can be accessed by direct imaging of the expanded cloud. Since the eigenfunctions of the harmonic trap transform self-similar under a Fourier transform, the final distribution in the case of a harmonic trapping potential will be just a magnified version of the original distribution in position space. In fact in the harmonic case the original distribution but magnified is already recovered at finite times. Finally, note that the authors argue that interactions among the atoms are negligible during the free expansion. Anyhow, the interactions between the atoms may be removed quasi-instantaneously during the measurement by flipping the (electronic) spin of one of the atomic species via a Raman transition. If the new mixture is only weakly interacting the interaction is effectively switched off [Holten et al., 2021a].

4.3 The Rotating Gaussian Trap and other experimental caveats

In the last chapters we have always tacitly assumed that the trapping potential has the form of a harmonic oscillator. Unfortunately, due to the ever more rapidly growing potential, harmonic traps are experimentally not possible to realize and the best one can achieve is to maintain a close to harmonic shape at the center of the trap before the potential eventually has to level off. The finiteness of the trap has some important consequences, most importantly it only supports a finite number of bound states and possesses a continuum of unbound states. That's especially relevant in the context of rotating traps. The rotating perturbations successively couple states to higher and higher angular momentum which may eventually cause the atoms to escape from the trap. This behavior will lead to a finite life time of the atoms in the trap setting an upper bound for the time in which the experiment has to be performed. Furthermore, the LLL hosts states with high angular momentum which are, due to their high energy in the resting frame, especially sensible to the actual shape of the trapping potential. These deviations in the potential will lift the degeneracy of the Landau levels, introducing another energy scale competing with the interactions.
As outlined in the introduction the 2D-traps used in the experiments in our group are mostly generated by strongly focused Gaussian laser beams. The potential the atoms feel via the optical dipole force is itself of Gaussian shape. Note, that in the optical setup used to generate the rotating traps the use of a spatial light modulator (SLM) allows one to madify the actual shape of the light fields. Typical trapping potentials might for example resemble more the shape of an Airy-disk. On the other hand, the SLM can also be used to increase the harmonicity of the potential.
However, for now we will adopt the model of a perfect Gaussian beam. At the very least this will serve us as a Toy-model to study effects of the finite trap depth and anharmonicity. In this spirit Laguerre-Gaussian laser beams will be used to generate the higher-order azimuthal perturbations.

4.3.1 Realistic Traps using Laguerre-Gaussian Laser Beams

A Laguerre-Gaussian beam is a special type of monochromatic electromagnetic radiation. It is a so called transverse electromagnetic mode, i.e. both the electric and the magnetic component oscillate in the plane perpendicular to the direction of propagation. Other characteristic features are the compact distribution of power around the central axis of propagation, giving it its beam like shape and that the beam is maintaining its intensity pattern in the transverse plane up to rescaling. Gaussian beams in general are a solution to the paraxial Helmholtz equation, i.e. their amplitude is assumed to vary only very slowly on the scale of the wavelength

of the light. The amplitude of the Laguerre-Gaussian beam at its focus is given by

$$\mathrm{LG}_p^l(r,\phi,z=0) = \frac{\sqrt{2}}{w_0}\sqrt{\frac{p!}{\pi(|l|+p)!}}\left(\frac{\sqrt{2}r}{w_0}\right)^{|l|} L_p^{|l|}(2r^2/w_0)e^{il\phi}e^{-r^2/w_0^2}, \quad (4.20)$$

where w_0 is called the minimal waist of the beam which it assumes precisely at the focus. Note, that this is equivalent to the eigenfunctions (3.5) of the 2D harmonic oscillator with the oscillator length given by $l_0 = w_0/\sqrt{2}$. The amplitude eq. (4.20) is normalized accordingly and hence a beam of total power $P = \int d^2x|u(\boldsymbol{x})|^2$ is simply given by $u = \sqrt{P}\mathrm{LG}_p^l$.
For a standard Gaussian beam consisting only of the LG_0^0 mode the intensity distribution in the focal plane is given by

$$I(r) = \frac{2P_0}{\pi w_0^2}e^{-2r^2/w_0^2} = I_0 e^{-2r^2/w_0^2}, \quad I_0 \equiv \frac{2P_0}{\pi w_0^2}. \quad (4.21)$$

Let us now consider the presence of atoms in the focal spot of the beam with a optical transition ω_0 close to the frequency of the laser light ω_L. For a large red-detuning with respect to the width of the transition Γ, $\Delta = \omega_0 - \omega_L \gg \Gamma$, the atoms experience an attractive force from the laser field , c.f. eq. (2.21),

$$V(r) \approx -\frac{3\pi c^2}{2\omega_0^3}\frac{\Gamma}{\Delta}I(r) = -V_0 e^{-2r^2/w_0^2}, \quad V_0 \equiv \frac{3c^2}{\omega_0^3}\frac{\Gamma P_0}{\Delta w_0^2}. \quad (4.22)$$

Evaluating this expression for small radii to lowest non-vanishing order allows one to make contact with the harmonic oscillator. Neglecting the constant shift we find

$$V(r) \approx \frac{2V_0 r^2}{w_0^2} + O(r^4) \equiv \frac{m\omega^2}{2}r^2, \quad (4.23)$$

where we identified the harmonic oscillator frequency

$$\omega = \frac{2}{w_0}\sqrt{\frac{V_0}{m}} = \sqrt{\frac{12c^2\Gamma}{m\omega_0^3\Delta}}\frac{\sqrt{P_0}}{w_0^2} \quad (4.24)$$

in terms of the mass of the atoms m. Due to the similarity of the Gaussian potential with the harmonic oscillator we estimate the Gaussian trap to contain $N = V_0/\hbar\omega$ 'shells'. The number of shells can be taken as a measure of the anharmonicity of the trap and is given by

$$N = \sqrt{\frac{3mc^2\Gamma}{4\hbar^2\omega_0^3\Delta}}\sqrt{P_0}. \quad (4.25)$$

Combining eq. (4.24) and (4.25) yields relations for the waist of the Gaussian beam and the total beam power in terms of the trapping frequency and the anharmonicity

[5]

$$\begin{aligned} w_0 &= \sqrt{\frac{4\hbar N}{m\omega}} \sim 8.19\ \mu\text{m}\sqrt{\frac{N\ /\ 10}{\omega\ /\ 2\pi\ \text{kHz}}} \\ P_0 &= \frac{4\hbar^2\omega_0^3\Delta}{3mc^2\Gamma}N^2 \sim 1.03\ \text{mW}\,(N/10)^2 \end{aligned} \quad . \tag{4.26}$$

The values for the waist and the beam power can be evaluated for a reasonable trapping frequency of $\omega = 2\pi$kHz and a moderate depth of $N = 10$. Assuming ^{6}Li to be used, fulfilling these constraints already requires a large trap of waist ~ 8 µm, which is much larger than usual trap sizes of $w_0 \sim 1$ µm. As we will see later on increasing the trap size further to $N \sim 20$ is probably necessary. This would correspond to a waist of ~ 12 µm. Note that an upper bound for the trapping frequency ω is given by the maximal experimentally possible trapping frequency in z-direction since we want to maintain a large aspect ratio ω_z/ω. We have $\omega_z \lessapprox 2\pi \cdot 30$kHz.
Before we investigate the spectrum of the Gaussian trap in detail, let us see how higher order Laguerre-Gaussian modes can be used to generate azimuthal perturbations.

Generating azimuthal perturbations with Laguerre-Gaussian beams

To this end we consider a superposition of a Gaussian beam with a waist w_0 and a higher-order $\hat{\text{LG}}_0^l$ beam with waist w_0'. Let the total amplitude be given by

$$u(r,\phi) = \sqrt{P_0}\text{LG}_0^0(r) - \sqrt{P_l}\hat{\text{LG}}_0^l(r,\phi). \tag{4.27}$$

We further assume the waists of both beams to be of comparable size, $\gamma = w_0/w_0' \sim 1$. The composed beam then generates a trapping potential

$$V(r,\phi) = -V_0 e^{-2r^2/w_0^2}\left|1 - \sqrt{\frac{P_l}{P_0}}\frac{\gamma}{\sqrt{|l|!}}\left(\frac{\sqrt{2}r}{w_0'}\right)^{|l|} e^{il\phi}e^{(1-\gamma^2)r^2/w_0^2}\right|^2 . \tag{4.28}$$

Expressing everything in terms of harmonic oscillator units $\omega = \sqrt{\frac{4V_0}{w_0^2 m}}$, $l_0 = \sqrt{\frac{\hbar}{m\omega}}$ and using that $\frac{l_0^2}{w_0^2} = \frac{\hbar\omega}{4V_0}$ we arrive at

$$\begin{aligned} V(r,\phi) &= -V_0 e^{-r^2/2V_0}\left|1 - \sqrt{\frac{P_l}{P_0}}\frac{\gamma}{\sqrt{|l|!}}\left(\frac{\gamma r}{\sqrt{2V_0}}\right)^{|l|} e^{il\phi}e^{(1-\gamma^2)r^2/4V_0}\right|^2 \\ &\equiv -V_0 e^{-r^2/2V_0}\left|1 - \frac{1}{V_0}\epsilon_l r^l e^{il\phi}e^{(1-\gamma^2)r^2/4V_0}\right|^2 \end{aligned} \quad , \tag{4.29}$$

[5] The numerical values are computed in the case of ^{6}Li, with $\omega_0 = \frac{2\pi c}{671\ \text{nm}}$, $\Delta = 2\pi c\ (1/671 - 1/1064)\ \text{nm}^{-1}$ and $\Gamma = 2\pi \cdot 5.87$ MHz.

where now all energies and lengths are dimensionless and the perturbation strength

$$\epsilon_l = \gamma^{|l|+1}\sqrt{\frac{P_l}{P_0|l|!}\frac{V_0^2}{(2V_0)^{|l|}}} \tag{4.30}$$

has been introduced. Evaluating the square yields [6]

$$V(r,\phi) = -V_0 e^{-r^2/2V_0} + \epsilon_l r^l (e^{il\phi} + c.c.) e^{-(1+\gamma^2)r^2/4V_0} + O(\epsilon_l^2/V_0). \tag{4.31}$$

Whenever it's possible to neglect the second order term in ϵ is a somewhat subtle question that depends on the energy scale on which we want the approximation to be valid. Let R be the maximal length scale of interest which might either be given by the scale of the potential $R \sim \sqrt{2V_0}$ itself or by an angular momentum cut-off M in the LLL, yielding $R = \sqrt{M}$. If we want the approximation only to be accurate on the energy scale of the potential $\sim V_0$ we require $\epsilon_l R^l/V_0 \ll 1$. However, we usually want the harmonic oscillator to stay the dominant energy scale and thus we demand the perturbation itself to be small on that scale, i.e. $\epsilon_l R^l \ll 1$. Note that this automatically implies that the second order terms in ϵ are negligible, since $\epsilon_l R^l/\sqrt{V_0} \ll 1$.
Finally, if $R \ll \sqrt{2V_0}$ we can also perform the harmonic approximation yielding

$$V(r,\phi) = \frac{r^2}{2} + \epsilon_l r^l (e^{il\phi} + c.c.), \tag{4.32}$$

where the offset energy was omitted.
The time-dependent perturbation potential eq. (4.9) for only one $\epsilon_l \neq 0$ can be recovered by introducing a detuning $\delta = l\Omega$ between the trapping the and perturbation laser. This results in the potential

$$V_l(r,\phi,t) = \epsilon_l r^l (e^{il\phi} e^{il\Omega t} + c.c.). \tag{4.33}$$

4.3.2 Exact single-particle spectrum

Let us now compare the single-particle spectrum of the Gaussian trap to that of a harmonic trap. The potential of the Gaussian trap is given by

$$V_g(r) = -V_0 e^{-r^2/2V_0}, \tag{4.34}$$

where we have already expressed all quantities in harmonic oscillator units. The single-particle Hamiltonian can then be conveniently written as

$$H_g = \underbrace{\frac{1}{2}(-\Delta + r^2) - (1-\alpha)M}_{H_0} - V_0 e^{-r^2/2V_0} - \frac{1}{2}r^2 \tag{4.35}$$

[6] The second order term in ϵ_l computes to $\frac{1}{V_0}\epsilon_l^2 r^{2l} e^{-\gamma^2/2V_0}$.

consisting of the harmonic trap Hamiltonian H_0 as seen from the rotating frame and a perturbation term. The matrix elements of the Gaussian potential and the harmonic term can be computed analytically in the harmonic oscillator basis (3.5),

$$\langle k', m|V_g|k, m\rangle = -V_0\sqrt{\frac{k!k'!}{(k+|m|)!(k+|m|)!}}\int_0^\infty dx x^m e^{-(1+a)x}L_k^{|m|}(x)L_{k'}^{|m|}(x), \tag{4.36}$$

with $a = 1/2V_0$. The remaining integral is a special case of the more general integral [Srivastava et al., 2003] [7]

$$\begin{aligned} I[k, m,k', m'; l, a] &= \int_0^\infty dx x^\mu e^{-(1+a)x}L_k^{|m|}(x)L_{k'}^{|m'|}(x), \quad \mu = \frac{1}{2}(l+|m|+|m'|) \\ &= \frac{\Gamma(\mu+1)}{(1+a)^{\mu+1}}\sum_{n=0}^{\min(k,k')}\binom{k+|m|}{k-n}\binom{k'+|m'|}{k'-n}\binom{n+\mu}{n}(1+a)^{-2n} \\ &\quad \cdot {}_2F_1\left(-k+n, \mu+n+1, |m|+n+1, \frac{1}{1+a}\right) \\ &\quad \cdot {}_2F_1\left(-k'+n, \mu+n+1, |m'|+n+1, \frac{1}{1+a}\right) \end{aligned} \tag{4.37}$$

appearing in the context of $\langle k', m'|r^l e^{il\phi}e^{-ar^2}|k, m\rangle$. The harmonic term, giving the expectation value of the potential energy on the diagonal, can be expressed similarly as

$$\begin{aligned} \langle k'm|r^2|k, m\rangle &= (|m|+1)!(-1)^{k+k'}\sqrt{\frac{k!k'!}{(k+|m|)!(k'+|m|)!}} \\ &\quad \cdot \sum_{n=0}^{\min(k,k')}\binom{1}{k-n}\binom{1}{k'-n}\binom{|m|+1+n}{n}, \end{aligned} \tag{4.38}$$

which only couples $k = k'$ and $k = k' \pm 1$ modes.
Since the Gaussian potentials retains the rotational symmetry of the harmonic Hamiltonian, angular momentum stays a good quantum number. We can then solve for the eigenvalue spectrum for each angular momentum channel separately. The resulting spectrum for different trap depths is shown in Fig. 4.6a. In the deconfinement limit we can clearly see how the degeneracy is lifted. With higher angular momentum m the levels start to curve down significantly. Fig. 4.6b gives a quantitative picture of the energy shifts in the LLL. Even for low angular momenta fairly deep traps are necessary to ensure that the energy shifts stay below $\hbar\omega$. Furthermore, we see that shallow traps host only a small number of states in the LLL.

[7] ${}_2F_1(a, b, c; z)$ is the Gaussian hypergeometric function.

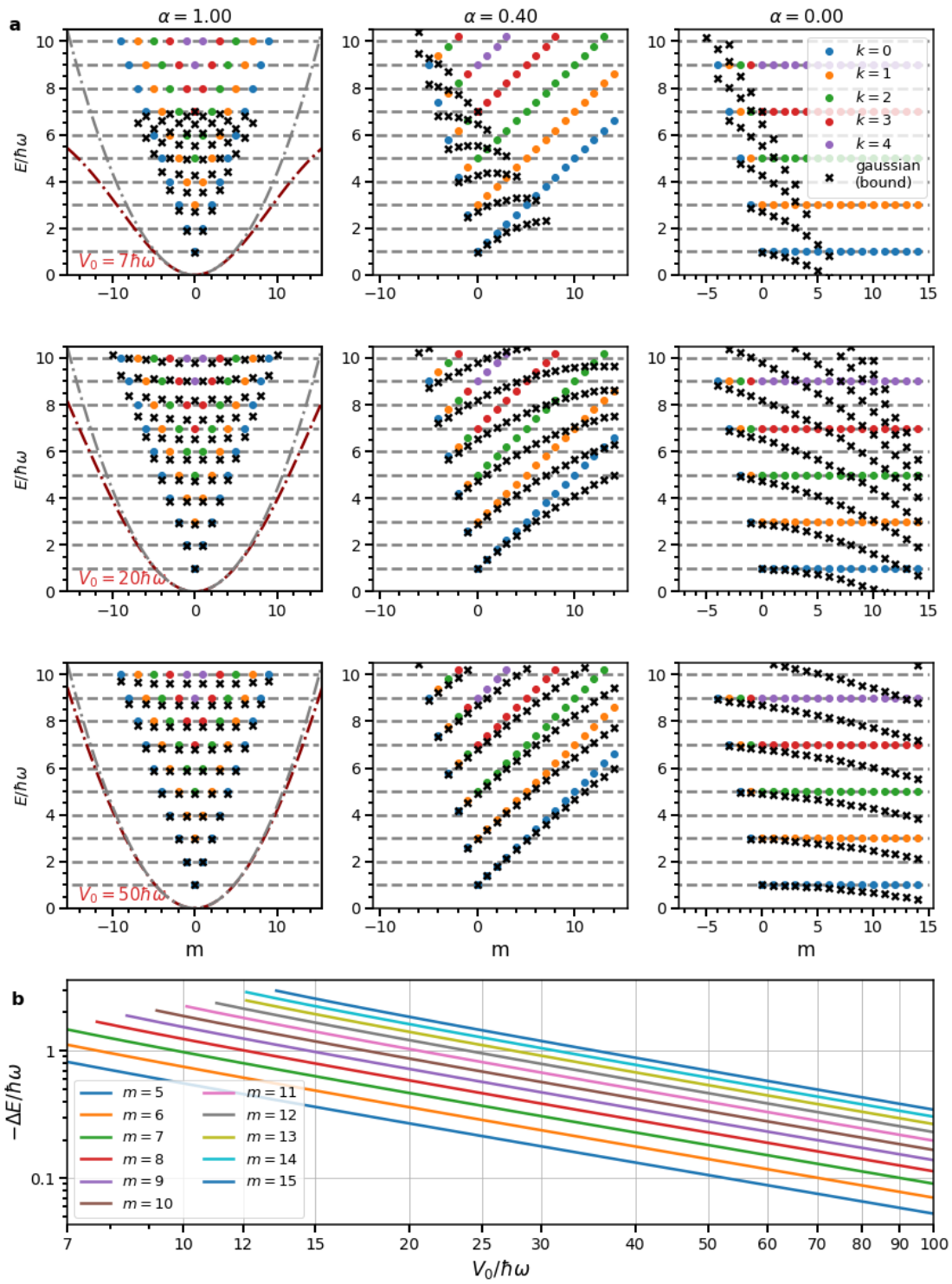

Figure 4.6: **Energy Spectrum of the Gaussian Trap**
a - Exact energy spectrum of Gaussian traps of various depths V_0 (rows). The columns show the spectrum as seen from a rotating frame rotating with frequency $1-\alpha$. For comparison the levels of the harmonic oscillator are shown as well. **b** - Energy shift of the LLL levels in the Gaussian trap as compared to the harmonic oscillator, $\Delta E_m = E_m^{Gaussian} + V_0 - E_m^{HO}$.
m is the angular momentum quantum number. Only bound states with energy $E < 0$ are depicted. Per m-channel 41 k-modes are used to expand the Hamiltonian.

4.3.3 How deep is deep enough?

A natural question to ask now is how deep we have to design the Gaussian trap to avoid the lifted degeneracy in the LLL to destroy the fractional quantum hall states we're seeking. Qualitatively speaking we expect the degeneracy to be sufficiently well preserved when the energy shift ΔE_{an} caused by the anharmonicity is small compared to the scale of the interaction $\Delta E_{int} = g/2\pi$. In the opposite regime $\Delta E_{an} > \Delta E_{int}$ the particles may be willing to pay the extra energy cost of the interaction, since we take $g > 0$, in favor of a net gain of energy by shifting the weight of the populated angular momentum states around (still maintaining the same total angular momentum).
To get a more quantitative picture of this effect we want to study the ground state of the Gaussian trap in the deconfinement limit. Since we're ultimately interested in finding the $\Psi^{(1)}_{(1,1,1)}$ Skyrmion-state let us compare the numerically computed ground state in the $S^2 = 0, M = 18$ channel for $3 + 3$ atoms with the 'Gaussian' Skyrmion, i.e. instead of the harmonic LLL-states we use the analog states from the Gaussian trap. To this end we expand the Gaussian Hamiltonian eq. (4.35) and the contact interaction on a large harmonic oscillator basis with angular momentum cut-off $0 \leq m \leq 9$ and six k-modes per m-channel. In a first step we solve the single-particle problem from which we get the eigenstates of the Gaussian-trap. By taking only the two lowest eigenstates per m-channel we can create a new much smaller basis, which we denote by $b^\dagger_{k,m,\sigma} = \sum'_k R^{(m)}_{k,k'} a^\dagger_{k',m,\sigma}$. All operators in second quantization are then readily obtained by replacing $a_{k,m,\sigma} \to R^{(m)}_{k',k} b_{k',m,\sigma}$. This rotation procedure is handled automatically by *Quanty*, one only needs to provide the semi-unitary rotation matrices R which we already computed in the first step. We finally compute the ground state via *Quanty* where starting with the 'Gaussian'-Skyrmion state significantly boosts the convergence of the Lanczos-algorithm. The numerical results for different trap depths and interaction strengths are depicted in Fig. 4.7. Note that we introduced the interaction parameter $\eta = \frac{g}{4\pi}$ which was used in [Palm et al., 2020].[8] For a very low interaction strength of $\eta = 0.01$ no overlap with the Skyrmion-state is found. For $\eta = 0.05, \eta = 0.1$ and $\eta = 0.25$ the overlap jumps to order 1 at trap depths around $45\hbar\omega$, $20\hbar\omega$ and $12\hbar\omega$. Following the qualitative argument made above we should be able to infer similar values of the trap depth by considering the level shifts in Fig. 4.6b. The Skyrmion-state populates angular momentum states up to $m = 6$. Since that might be a little too conservative we read off the trap depths at which we find the corresponding energy shifts $\Delta E = 0.02, 0.1, 0.2$ and $\Delta E = 0.5$ ($\Delta E_{int} = 2\eta$) for the $m = 5$ state. This gives roughly $> 100\hbar\omega, 50\hbar\omega, 25\hbar\omega$ and $12\hbar\omega$, which is in fairly good agreement with

[8] In principle we should have $\eta = g$. Instead the numerical results from [Palm et al., 2020] can only be reproduced with $g = 4\pi\eta$. Note that the authors give the relation $\eta = \sqrt{8\pi}\frac{a_{3D}}{l_z}$. In contrast we found $g = \sqrt{8\pi}\frac{a_{3D}}{l_z}$ in eq. (4.12), which hints at an error. Note that also the matrix elements of the contact interaction in the LLL given in [Palm et al., 2020] differ by a factor 4π (be aware of the summation of spins in the operator!) to the ones given here, which is in line again with the relation $g = 4\pi\eta$.

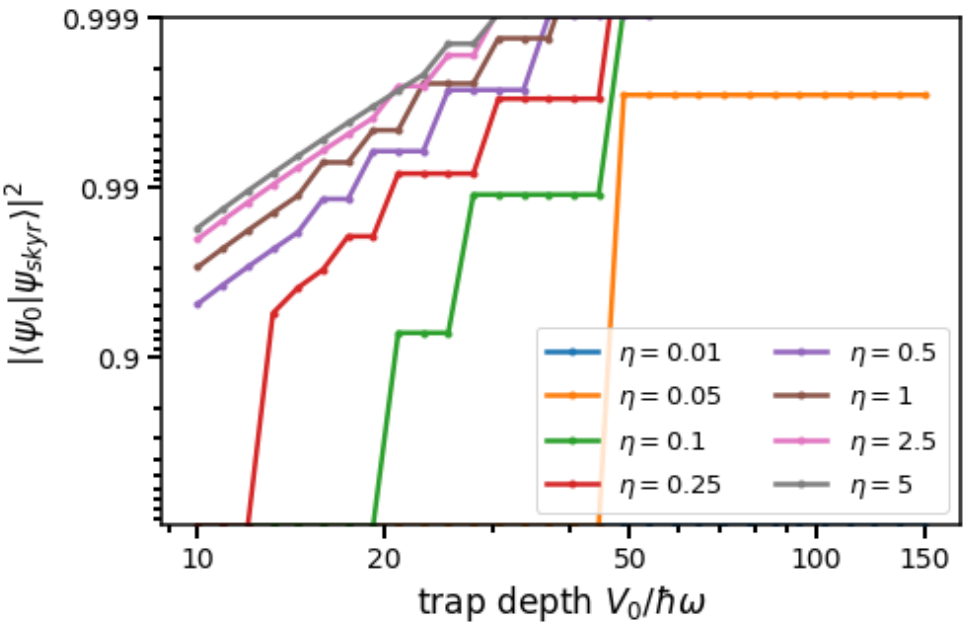

Figure 4.7: **Ground state overlap with the Skyrmion for the Gaussian Trap** Overlap of numerically computed ground state in the channel $S^2 = 0$, $M = 18$ with the 'Gaussian' Skyrmion-state $\Psi^{(1)}_{(1,1,1)}$ for $N_\uparrow = N_\downarrow = 3$ (the state is build with states from the Gaussian LLL instead of the harmonic oscillator LLL). The two lowest Landau levels of the Gaussian traps with angular momentum cut-off $0 \leq m \leq 9$ are used. The interaction strength η is related to the previously used coupling constant $g = 4\pi\eta$. Hence, the interaction energy is $\Delta E_{int} = 2\eta$.

the numerical finding!
Note that the overlap was computed for $\eta > 0.5$ as well, corresponding to large interaction energies of above $1\hbar\omega$. Interestingly, the Skyrmion-state sill remains the ground state of the system, despite the presence of the second Landau level. However, this can be anticipated because the positive coupling constant strongly favors non-interacting states as the ground state. In that sense we expect the Skyrmion-like ground state even for arbitrary large η. Per contra, as has been discussed already, a positive coupling constant hides the dimer-state. For large interaction strengths we will finally come into a regime where the dimer-like states become to shallow to be ignored anymore (cf. Fig. 3.2b,d). Then such dimer-like states, consisting of many Landau levels, will become the new ground state of the system.
Besides the condition $\Delta E_g < \Delta E_{int}$, we should take care that no relevant states from the next higher Landau level drop into the LLL, i.e. $\Delta E_g^{1LL} < 2\hbar\omega$. This condition is fulfilled for all trap depths considered in Fig. 4.7.

4.3.4 Adiabatic Passage in the Gaussian Trap

We conclude our discussion of the Gaussian trap by considering the adiabatic preparation of the Skyrmion-state. Based on Fig. 4.7 we choose a moderately deep trap of $V_0 = 20\hbar\omega$ and a coupling constant of $g = \pi$ ($\eta = 0.25$). Starting from a closed-shell configuration of $3 + 3$ non-interacting atoms the LLL can be reached by the same protocol that was already mentioned when discussing the harmonic trap. We apply a ($l = 3$)-perturbation which opens a gap between the $|0, -1\rangle$ and $|0, 2\rangle$ state. Beyond $\alpha \approx 0.5$ the perturbation can be turned off as we have successfully prepared the $S = 0, M = 6$ $\Psi_{(1,1,0)}$ state. Note that due to the anharmonicity of the Gaussian trap, the position of the gap will be slightly shifted as compared to the harmonic case. In a next step we switch on the interactions and apply the elliptical ($l = 2$)-perturbation. Note that one wants to do this only at rather small α where the LLL (up to the angular momentum we care about) is energetically separated from the higher Landau Levels. This avoids coupling into other Landau levels which might otherwise be energetically favorable.
Let us pause for a moment here. In the harmonic case we would now ramp up the speed of rotation until the Skyrmion-state is reached i.e. when the Skyrmion becomes the ground state of the non-perturbed system. Since it is the first state with vanishing interaction energy for $S = 0$, all higher angular momentum states will be shifted by an energy $\alpha\Delta M$. Depending on the ratio between $\alpha\Delta M$ and the strength of the perturbation an increasing number of higher excited states will be coupled into the perturbed ground state. However, by slowly switching off the perturbation we can drive the system eventually into its true ground state, the Skyrmion.
For the Gaussian trap this situation unfortunately is much more delicate. States with angular momentum higher then the Skyrmion will have a lower total energy due to the energy shifts in the Gaussian trap. Because these shifts can easily exceed $\hbar\omega$ for high enough angular momentum the strict ordering in energy with increasing total angular momentum we know from the harmonic trap is not maintained. Thus we expect states of higher angular momentum $M > 18 + \Delta M$ to be the true ground states where we would have thought to the find the Skyrmion (actually these will be scattering states with arbitrarily high angular momentum). Note that ΔM will increase with the depth of the trap. Without any coupling between states of different M we can simply ignore this effect. In the presence of the elliptical perturbation however we have to be careful as it can directly couple states up to $\Delta M \leq 12$ (for 6 particles). Now, if the Skyrmion-state gets coupled to a state of lower energy we can no longer drive the system into the Skyrmion-state by switching off the perturbation! Under which circumstances this is going to be a problem is hard to anticipate. Due to the large angular momenta involved numerical simulation is not feasible as the corresponding Hilbert spaces are too large. For now we simply resort to checking if the occupation probability of the different angular momentum states drops to zero for the highest m states. An interesting option to address this potential problem consists in designing the perturbation to primarily couple states of lower angular momentum. This can be achieved by choosing a narrower waist for the perturbation

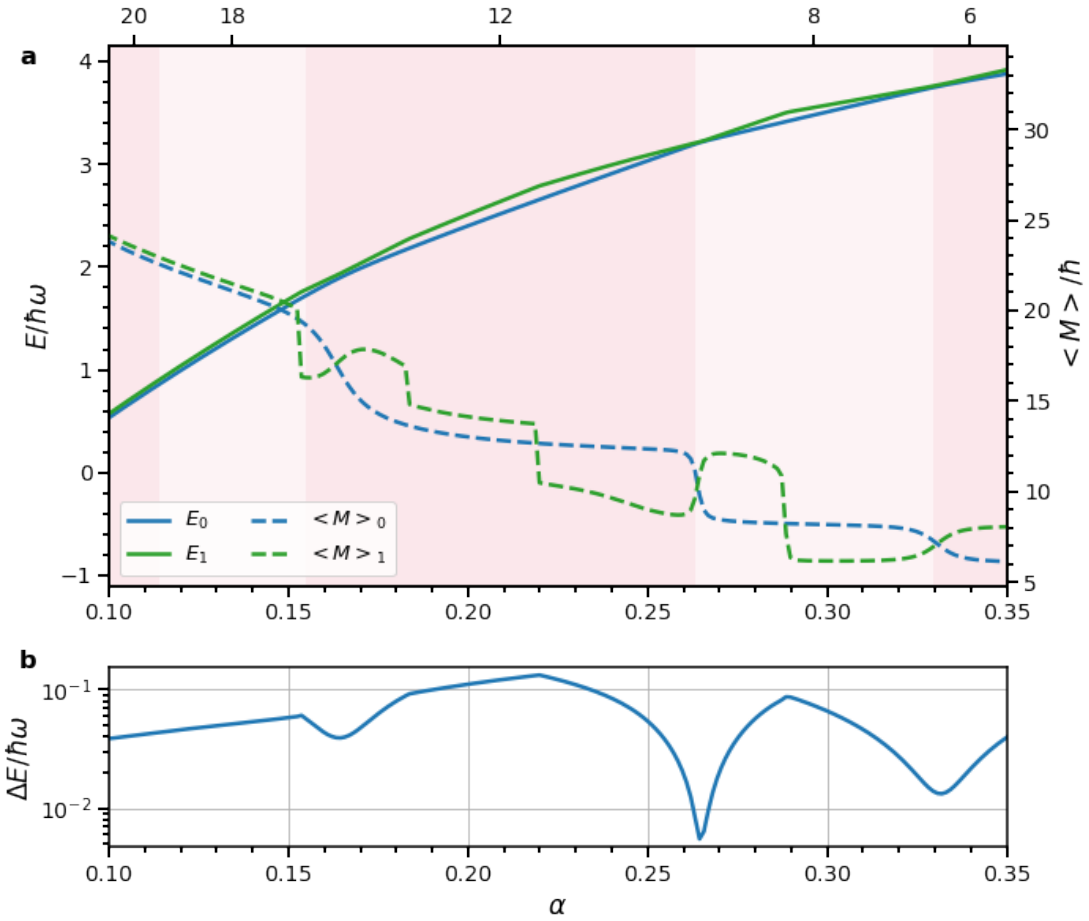

Figure 4.8: **Adiabatic Passage for $3+3$ atoms in the Gaussian Trap**
a - Energy of the two lowest states for $3+3$ atoms in a Gaussian trap of depth $20\hbar\omega$ perturbed with a elliptical perturbation rotating with speed $2\Omega = 2\omega(1-\alpha)$. The energies have been shifted with respect to the vacuum energy. The perturbation has strength $\epsilon_2 = 0.02$ and the same waist as the Gaussian trap, i.e. $\gamma = 1$. The interaction strength is set to $\eta = 0.25$ ($g = \pi$). Highlighted regions indicate the angular momentum (top x-axis) of the ground state in the unperturbed trap. Besides the energy the expectation value of angular momentum is plotted on the right axis for both states. Numerical results are obtained by expanding on a basis of the Gaussian-LLL with maximum angular momentum $m_{max} = 9$. **b** - Energy gap between the ground and first excited state.

beam, i.e. $\gamma > 1$. Fig. A.1 in the appendix shows the matrix elements of the $l = 2$ perturbation for $V_0 = 20\hbar\omega$ and different γ. At the cost of higher coupling into the first Landau level the coupling between higher angular momentum modes can be significantly reduced.
Let us now set this issue aside and focus on the result of a computation where we choose $\epsilon_2 = 0.02$ [9] and $\gamma = 1$ for simplicity, i.e. both the trap and the perturbation have the same waist. As before we expand the Hamiltonian on the Gaussian LLL with angular momentum cut-off $m_{max} = 9$. In Fig. 4.8a the energies and angular momentum expectation values of the two lowest laying eigenstates in the spin singlet-channel are plotted. Due to the perturbation gaps open in the spectrum and we can adiabatically follow the ground state from $M = 6$ to the Skyrmion at $M = 18$. The energy difference between both states is plotted in Fig. 4.8b. The values found here a very similar to the findings of Palm et al. [2020] for the same set of parameters ($\eta = 0.25$, $\epsilon = 0.02$) in the harmonic case. In Fig. 4.8a the highlighted background areas indicate the regions for which the state with total angular momentum M (top x-axis) is the ground state of the unperturbed system. For the first three segments ($M = 6, 8, 12$) pronounced plateaus in the angular momentum of the perturbed ground state can be observed. Once the $M = 18$ region is entered this changes and angular momentum starts to increase more steadily in both the ground and the first excited state. For the excited state this is in strict contrast to the behavior observed for $M < 18$, where its angular momentum content often times got exchanged with that of the ground state or a higher excited state whenever there was a level crossing. This is to be anticipated since states beyond $M = 18$ can effectively suppress the interaction. This leads to a reduced separation in energy which enhances the transfer of angular momentum.
In Fig. 4.9 we further plot the ground state density distribution at selected points during the adiabatic passage. One can clearly see how the ellipticity of the droplet increases for higher rotational speed. In the lower right corner also the occupation probability of the different angular momentum modes in the LLL is plotted. Beyond $\alpha = 0.16$ more weight is pushed into modes with higher angular momentum. This may be taken as a signal that the used Hilbert space becomes too small. Especially the results towards $\alpha = 0.1$ should hence be taken with a grain of salt.
Finally, let's get some numbers about the Gaussian and Laguerre-Gaussian beams we would need to execute the aforementioned protocol. First of all eq. 4.26 tells us that we need a 4 mW beam with a 12 µm waist to generate a trap of depth $20\hbar\omega$ and a trapping frequency of 2π kHz. The power of the perturbation beam can be computed from eq. 4.30 which yields 13 µW. From Fig. 4.8b we can now also read off the minimal gap size which gives $\Delta \sim 2\pi \cdot 5$ Hz.

[9] In the harmonic approximation this yields a critical speed of $\alpha_c = 0.02$. At faster rotation the atoms are anti-confined and will escape from the trap.

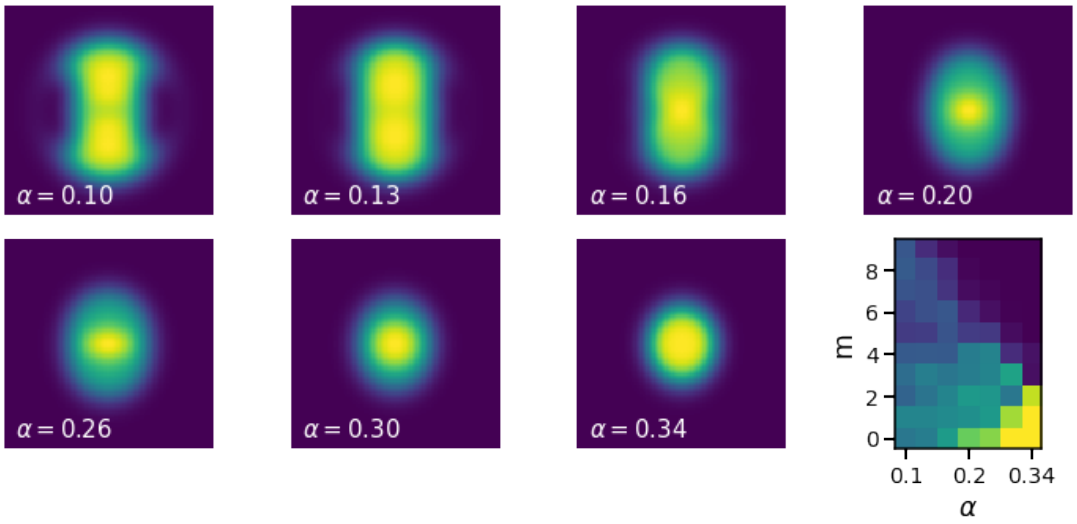

Figure 4.9: **Density of $3+3$ atoms during an adiabatic passage in the Gaussian Trap**
The density distribution during the adiabatic passage of $3+3$ atoms in a Gaussian trap of depth $V_0 = 20\hbar\omega$ is shown in the region $[-5,5] \times [-5,5] l_0$. The trap is perturbed with an elliptical perturbation of strength $\epsilon_2 = 0.02$ and same waist as the Gaussian trap, i.e. $\gamma = 1$. The interaction strength is set to $\eta = 0.25$ ($g = \pi$). Numerical results are obtained by expanding on a basis of the Gaussian-LLL with maximum angular momentum $m_{max} = 9$. In the bottom right corner the occupation probability of the different angular momentum modes in the LLL is depicted. For small speed of rotation $\alpha < 0.16$ the higher angular momentum modes become increasingly populated. This may indicate that the numerical results become erroneous, especially towards $\alpha = 0.1$.

4.4 Implementation and Experimental Methods

After discussing the physics in a rotating harmonic trap and the more realistic rotating Gaussian trap from a theoretical standpoint we finally turn towards their experimental realization. A central role of this chapter will be played by the spatial light modulator (SLM) that allows us to generate the light fields needed for trapping and perturbing the atoms. However, since it heavily relies on the concept of Fourier optics, we shall start with a brief introduction to this subject first. In this context we will also discuss the Fourier transforming properties of lenses, perhaps our most important optical tool after all. Special focus will be put on the influence of aberrations on the formed Fourier transforms. Eventually, the current optical setup will be presented.

4.4.1 Optical Design: Lenses and Aberrations

A short Introduction to Fourier Optics

Already in the context of the Gaussian beams we came across the paraxial Helmholtz equation. This is a special case of the general wave equation under the condition that the spatial shape of the involved light fields varies only very slowly on the scale of the wavelength of the light. Let us take a few steps back and start from the scalar wave equation

$$\left(\nabla^2 - \frac{1}{c^2}\frac{\partial^2}{\partial t^2}\right) u(\boldsymbol{x}, t) = 0. \tag{4.39}$$

It describes the evolution of the scalar wave u which we will take to be the amplitude of the electric field $\boldsymbol{E}$. Note that this will yield a valid description of electromagnetic waves in linear, homogeneous and isotropic media. Separating the amplitude into a product $u(\boldsymbol{x}, t) = u(\boldsymbol{x})e^{i\omega t}$ immediately yields the Helmholtz equation

$$\left(\nabla^2 + k^2\right) u(\boldsymbol{x}) = 0, \tag{4.40}$$

where the wave number k obeys the well-known wave relation $k = |\omega|/c$. A convenient solution is again found by a product ansatz separating the spatial coordinates, $u(\boldsymbol{x}) = e^{i\boldsymbol{k}\cdot\boldsymbol{x}}$. In order to fulfill the wave relation one of the components of the wave vector $\boldsymbol{k}$ is constrained in terms of the others. Choosing this to be the z-component gives the solutions

$$u_{k_x,k_y}(\boldsymbol{x}) = e^{-i(k_x x + k_y y)} e^{\mp i\sqrt{k^2 - k_x^2 - k_y^2}\, z}. \tag{4.41}$$

These are just plane waves with wavelength $\lambda = 2\pi/k$ which propagate in either positive or negative z-direction as long as $k^2 > k_x^2 + k_y^2$. Beyond this point the z-propagation becomes damped exponentially as k_z becomes imaginary. [10] Since the

[10] Technically, it grows exponentially in the other direction. However, without any further boundary conditions, e.g. in a finite volume, this branch of the solution is unphysical.

Helmholtz equation is linear and k_x and k_y are still unconstrained we can superimpose solutions as we wish. This allows us to compose an (almost) arbitrary field in some plane of fixed z, e.g. $z = 0$,

$$u_0(x,y) = \int dk_x dk_y U_0(k_x,k_y) e^{-i(k_x x + k_y y)} e^{-i\sqrt{k^2 - k_x^2 - k_y^2}z}|_{z=0} = u(x,y,z=0), \quad (4.42)$$

which we recognize as a Fourier transform. Evaluating u at non-zero z then tells us how the field u_0 propagates to planes at different z! Due to the important role of the Fourier transform, this approach to solving the Helmholtz equation was termed Fourier optics. It is especially useful when the problem allows one to consider the propagation of fields between planes, like above.
By means of the Fourier transform [11]

$$U(\nu_x,\nu_y) = \mathcal{F}[u](\nu_x,\nu_y) = \int dxdy u(x,y) e^{2\pi i(\nu_x x + \nu_y y)} \quad (4.43)$$

of a function $u(x,y)$ we can write down the propagation of a light field given by u to a different plane located a distance d away by

$$G(\nu_x,\nu_y) = \underbrace{e^{-2\pi i\sqrt{\frac{1}{\lambda^2} - \nu_x^2 - \nu_y^2}d}}_{H_0} U(\nu_x,\nu_y). \quad (4.44)$$

The field in the new plane can be computed by in the inverse Fourier transform of G, i.e. $g(x,y) = \int d\nu_x d\nu_y G(\nu_x,\nu_y) e^{-2\pi i(\nu_x x + \nu_y y)}$. H_0 is called the transfer function of free space. Throughout the rest of this thesis we will assume the so-called small angle and Fresnel approximation which is valid in the regime

$$\lambda^2\nu^2 \ll 1, \quad \frac{d\lambda^3\nu^4}{4} \ll 1, \quad \nu^2 = \nu_x^2 + \nu_y^2. \quad (4.45)$$

Since the smallest features in real-space δx_{min} will determine the largest features in Fourier-space $\nu_{max} = 1/\delta x_{min}$ the first conditions tells us that u better be well resolved on the scale of the wavelength, i.e. $\delta x_{min}/\lambda \gg 1$. Introducing the angle θ between the wave vector $\boldsymbol{k}$ and the z-direction allows us to write $\nu = \frac{1}{\lambda}\sin\theta$. The small-angle condition then translates to $\theta^2 \ll 1 \Leftrightarrow \nu \approx \theta/\lambda$. We can also rewrite the second condition in this way, $d\theta^4/4\lambda \ll 1$. Putting everything together allows us to expand the square root in the free space transfer function to first non-vanishing order in ν,

$$H_0 \approx e^{-ikd} e^{i\pi\lambda d(\nu_x^2 + \nu_y^2)}. \quad (4.46)$$

Using the convolution theorem we are now able to directly compute the propagated field g in real space,

$$g(x,y) = \frac{i}{\lambda d} e^{-ikd} \int dx' dy' u(x',y') e^{-i\frac{k}{2d}\left((x-x')^2 + (y-y')^2\right)}. \quad (4.47)$$

[11] In the following we will adopt the notation of Bahaa E. A. Saleh [1991], which essentially means introducing $\nu_i = k_i/2\pi$.

The thin Lens

Probably the most important piece of optics we will make use of is the lens. We don't really want to discuss the absolute basics here, rather we want to develop a little bit of a refined understanding in the context of Fourier optics. Especially, we want to focus on the Fourier transforming properties of the lens.
Let us start by considering a lens of very simple shape. One side shall be plane and its other side shall be shaped in terms of a function $\Delta(x, y)$ giving the thickness of the lens. Furthermore, let Δ_0 be its maximum thickness. In the spirit of Fourier optics we are interested in how a light field $u(x, y)$ propagates from the plane just before the lens, say at $z = 0$, to the plane at $z = \Delta_0$. For a moment let us picture a light ray passing through the lens. It will penetrate the lens at some point $(x, y, 0)$ where it will be refracted until it hits the other surface of the lens. Here it will be refracted again, leave the lens and finally arrive at the output plane at (x', y', z_0). In total the ray is now displaced and in terms of wave optics it will also have acquired a phase along its way. Both the displacement and the phase shift will depend in a very complicated way on the lens shape, the entrance point of the ray and its angle. This will only get worse if we want to follow the propagation of the whole light field u through the lens. Luckily, the problem considerably simplifies when we make a few assumptions that nevertheless allow us to capture typical practical situation quite well. The main problem of the full description is the complicated path a ray of light takes through the lens. However, if we assume a suitable combination of a thin profile $\Delta(x, y)$ and small angles at the diffracting surfaces we can approximate the path of the ray to be straight. The displacement will then be zero and the light field in the output plane is straightforwardly found to be $e^{-i(\Delta_0+(n-1)\Delta(x,y))}u(x, y)$, where n is the refractive index of the lens material. These assumptions are summarized under the name thin lens approximation. A special type of thin lens is the ideal lens which is precisely shaped to yield the output field

$$u'(x, y) = e^{ik\frac{x^2+y^2}{2f}}u(x, y), \tag{4.48}$$

with the focal length f of the lens. Within the thin-lens approximation a more realistic description can be obtained by introducing the pupil function $p(x, y) = T(x, y)e^{i2\pi W(x,y)}$ with which the light field is to by multiplied. $T(x, y)$ gives the transmission of the lens, which for the simplest case is given by $\Theta(D/2 - r)$[12], representing a spherical aperture of diameter D. $W(x, y)$ will encode aberrations to be discussed later on.

The Fourier transforming Lens

Let $\tilde{u}(x', y')$ be said input field directly in front of a lens with focal length f and pupil function $p(x', y')$. We now want to compute the field in the focal plane of the

[12] $\Theta(x)$ is the Heaviside step function

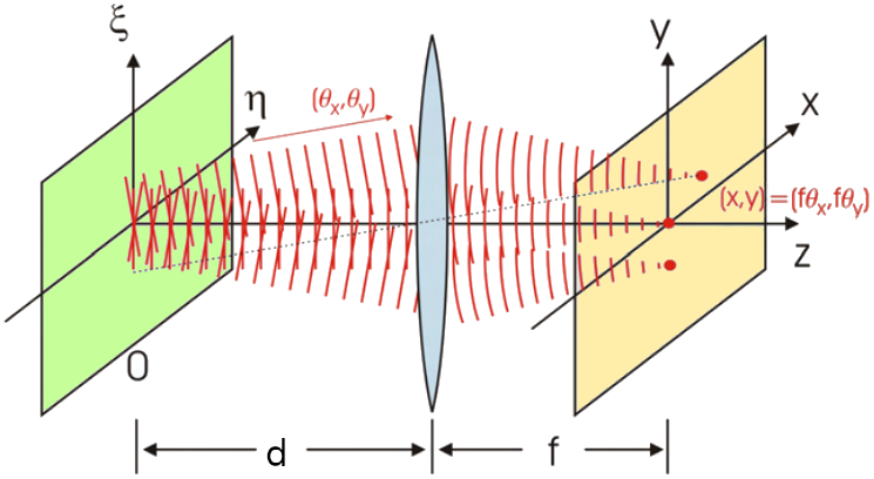

Figure 4.10: **The Fourier transforming lens**
The field in the object plane O can be decomposed into plane waves with different spatial frequency $\boldsymbol{\nu} = (\nu_x, \nu_y)$, which propagate under an angle $\boldsymbol{\theta} = (\theta_x, \theta_y) = \lambda\boldsymbol{\nu}$ with the optical axis (z-axis). The plane waves are focused in the focal plane of the lens at positions $(x, y) = \lambda f\boldsymbol{\nu}$, leading to the formation of the Fourier transform of the field in the object plane. Taken and adapted from [Heine, 2008].

lens. To this end we use eq. (4.47) which directly equates to (with $x_f = \frac{x}{\lambda f}, y_f = \frac{y}{\lambda f}$)

$$\begin{aligned} g(x,y) &= \frac{i}{\lambda f} e^{-ikf} e^{-i\frac{k}{2f}(x^2+y^2)} \int dx'dy' p(x',y')\tilde{u}(x',y') e^{2\pi i(x_f x' + y_f y')} \\ &= \frac{i}{\lambda f} e^{-ikf} e^{-i\frac{k}{2f}(x^2+y^2)} \int d\nu_x d\nu_y \tilde{U}(\nu_x,\nu_y) P(x_f-\nu_x, y_f-\nu_y). \end{aligned} \tag{4.49}$$

Up to a phase this is the Fourier transform of $\tilde{u}(x', y')$ times the pupil function! Or equivalently the Fourier transform $\tilde{U}$ of the input field convoluted with the Fourier transform P of the pupil function. Note that P is the well-known point spread function one encounters when considering the image formation properties of the lens, i.e. when we are interested in the field formed in the image plane of the lens. Well, usually one doesn't know the field in the lens plane but rather at some distance d before it. Using eq. (4.44) in the Fresnel-approximation we obtain

$$\begin{aligned} g(x,y) = &\frac{i}{\lambda f} e^{-ik(f+d)} e^{i\frac{k}{2f^2}(x^2+y^2)(d-f)} \\ &\cdot \int d\nu_x d\nu_y U(x_f-\nu_x, y_f-\nu_y) P(\nu_x,\nu_y) e^{i\pi\lambda d(\nu_x^2+\nu_y^2)} e^{-i2\pi\lambda d(\nu_x x_f + \nu_y y_f)} \end{aligned}, \tag{4.50}$$

where U is the Fourier transform of the field $u(\xi, \eta)$ at $z = -d$ (where (ξ, η) label the coordinates in that plane). This situation is sketched in Fig. 4.10. For the ideal lens the point-spread function is given by a delta function and the integral

reduces to $U(x_f, y_f)$. In the non-ideal case we now face also two exponential terms oscillating with ν and ν^2, respectively. These terms potentially influence the shape of the resulting light field g significantly. Especially for large distances g will look nothing like the Fourier transform of u anymore. Interestingly, the ν^2-term can be neglected for most of the experimental situations we're interested in. For reasonable applications the pupil function should be well concentrated inside a region of radius ν_p. In the case of a perfect spherical aperture of diameter D we find the Airy-disk $P(\nu) \sim J_1(\pi\nu D)/\nu$ for which we set $\nu_p \approx 1.22/D \approx 1/D$ based on its first root. We can then neglect the ν^2-term in eq. (4.50) provided that

$$\frac{\lambda d}{D^2} \ll 1 \tag{4.51}$$

holds. For a typical one-inch lens this gives a pretty large upper bound for the distance of $d \ll 606$ m given that we use infrared light with a wavelength $\lambda \sim 1$ µm. Under this assumption the integral in eq. (4.50) reduces to

$$\int d\nu_x d\nu_y U(x_f - \nu_x, y_f - \nu_y) P(\nu_x, \nu_y) e^{-i2\pi\lambda d(\nu_x x_f + \nu_y y_f)} \tag{4.52}$$

or equivalently

$$\int d\xi d\eta \; u(\xi, \eta) p(\xi + \lambda d x_f, \eta + \lambda d y_f) e^{i2\pi(\xi x_f + \eta y_f)}, \tag{4.53}$$

which we recognize as some kind of odd convolution and Fourier transform, respectively where the function to be transformed depends on the final argument. The latter equation is the easiest to interpret by considering again the angle $\boldsymbol{\theta}$ corresponding to a spatial frequency $\boldsymbol{\nu}$ or position in the focal plane $\boldsymbol{x}_f$ as $\boldsymbol{\theta} = \lambda\boldsymbol{\nu} = \lambda\boldsymbol{x}_f$. Plugging this into eq. (4.53) tells us that the pupil function is shifted by $d\boldsymbol{\theta}$. This is exactly the geometrical displacement in the lens plane rays propagating with wavevector $\boldsymbol{k} = (\boldsymbol{\theta}/\lambda, k_z)$ acquire over the distance d! Hence, the shift just accounts for the evolution of the light field from the object to the lens plane. Now for the ideal lens with finite aperture the pupil function is just given by a disk of radius $D/2$, $p(r) = \Theta(D/2 - r)$, and evaluating the integral for different positions in the focal plane will crop out different parts of the light field $u(\xi, \eta)$ to be Fourier transformed. For our purposes we can assume $u(\xi, \eta)$ to be extending over a scale smaller or at most comparable to the lens' aperture. We can then identify two interesting regimes, where we for simplicity also take $u(\xi, \eta)$ to be centered at the optical axis. If

$$\lambda d r_f \ll D, \quad \text{with } r_f^2 = x_f^2 + y_f^2 \tag{4.54}$$

we can simply neglect the pupil function and obtain a perfect Fourier transform in the focal plane. In the opposite regime, $\lambda d r_f \gg D$, the integral becomes zero since we evaluate the pupil function outside the aperture. Since $\nu_p \approx 1/D$, this condition is equivalently expressed as $2\lambda d r_f \nu_p \gg 1$ and we observe that the convolution eq.

(4.52) will vanish accordingly due to the now rapidly oscillating exponential. In total this tells us that the free space propagation together with the lens is causing a cutoff

$$\nu_c = \frac{1}{2d\lambda\nu_p} = \frac{D}{2d\lambda} \tag{4.55}$$

in the frequency spectrum of the field $u(\xi, \eta)$. In that sense the lens acts as a lowpass filter. Hence, under the above assumptions we find the field in the Fourier plane $z = f$ to be given by,

$$g(x,y) = \frac{ie^{-ik(f+d)}}{\lambda f} e^{i\frac{k}{2f^2}(x^2+y^2)(d-f)} (U*P)(x_f, y_f) \sim \mathcal{F}[u{\cdot}p](x_f, y_f), \quad r_f \ll \nu_c \tag{4.56}$$

where $*$ denotes the usual convolution. [13] Note that the pupil function also introduces a maximal cutoff length scale $L = 1/\nu_p$ for the field $u(\xi, \eta)$ in the object plane at $z = -d$, where in the simplest case of a perfect spherical pupil function we have $L = D$. This corresponds to the finest length scale $\delta x_f = 1.22/D$ in the Fourier plane. In physical coordinates $x = x_f/\lambda f$ we find the well-known diffraction-limited resolution $\delta x = 1.22\lambda f/D = 0.61\lambda/\mathrm{NA}$, where $\mathrm{NA} = D/2f$ is the numerical aperture of the lens.
Finally, note that the non-ideal pupil function will not be unity inside the aperture and thus the shift in eq. (4.53) actually does matter at intermediate frequencies, $\nu \lesssim D/2\lambda d$. However, if the frequency spectrum of u is concentrated sufficiently well around a central value, say $\boldsymbol{\nu}_0$, we might simply get away with replacing $p(\boldsymbol{x}) \to p(\boldsymbol{x} + \lambda d\boldsymbol{\nu}_0)$ and $P(\boldsymbol{\nu}) \to P(\boldsymbol{\nu})e^{-2\pi i\lambda d\boldsymbol{\nu}\cdot\boldsymbol{\nu}_0}$ in eq. (4.56).

Aberrations

In the typical experimental situations we face during this thesis the field in the focal plane of the lens should be well described by eq. (4.56). Furthermore, all lenses will be chosen such to avoid any clipping of the incident beam. Thus, one might assume that $P(\nu_x, \nu_y)$ is essentially 1 and all the Fourier transforms we need are going to be perfectly realized. Unfortunately, realistic lenses are other than perfect. All sorts of errors during the manufacturing-process and the optical alignment by the end-user, but also designed deviations from the optimal geometric shape for a single wavelength lead to broadening of the point-spread function. While the effect of these errors will unarguably have significant impacts on the actual light fields that form in the lens focal plane our hope is that they are small enough to still be describable in the thin lens approximation. To this end the phase term $e^{2\pi iW(x,y)}$, $W \in \mathbb{R}$ was introduced in the pupil function.

[13] $(f * g)(x, y) = \int dtduf(t, u)g(x - t, y - u)$.

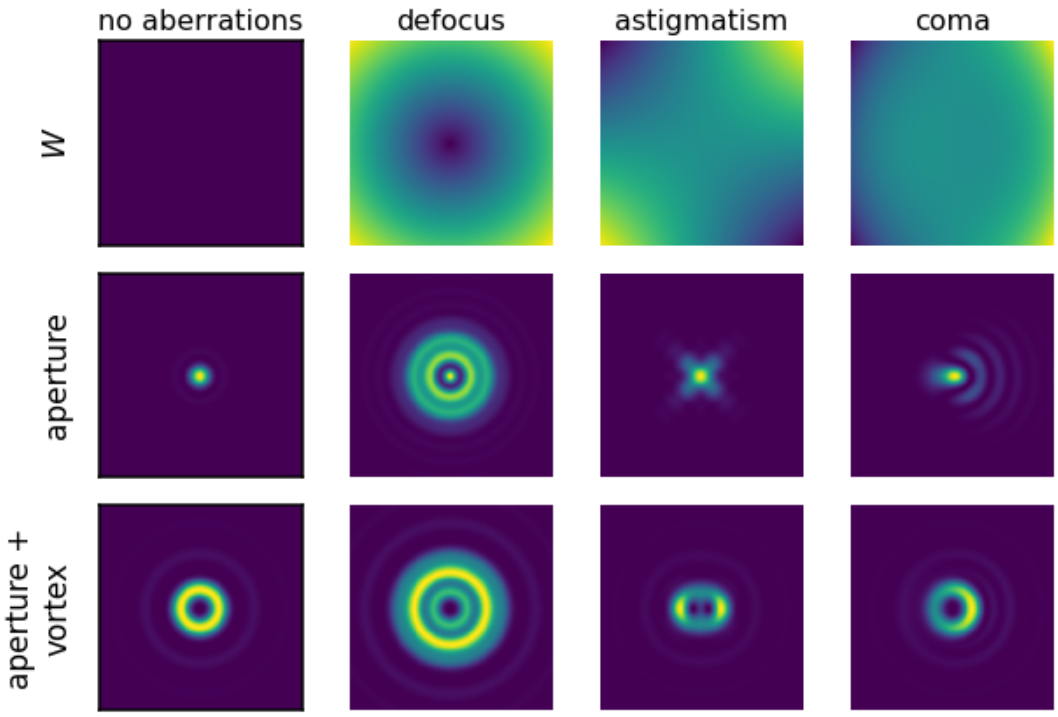

Figure 4.11: **Aberrations**
The effect of different aberrations on the intensity profile of a flat-top beam with constant phase (second row) and with a phase-vortex $e^{i2\phi}$ (third row) in the focal plane of a lens is depicted. The first row shows the phase error map $W(x, y)$ responsible for the aberrations caused by the lens. No aberrations, spherical defocus, astigmatism and coma are shown. For the flat-top beam with constant phase $3 \cdot W$ is used to enhance the visible effects of astigmatism and coma.

A few of the most common aberrations and their characteristic effects on two different types of light beams are depicted in Fig. 4.11. The second and third row show the intensity profile obtained in the focal plane of the lens for a flat top beam (second row) and a flat top beam with an additional second-order phase vortex $e^{2i\phi}$ (third row). For a perfect lens the latter will give rise to an intensity pattern close to a LG_0^2 Laguerre-Gauss mode. The focal pattern of the pure flat top beam is just the point spread function of the illuminated part of the lens. The different types of aberrations can be associated with the so-called Zernike polynomials, which form a basis for the real functions on the unit disk. Expanding $W(x, y)$ on this basis hence allows for a good qualitative and quantitative discussion of the aberrations present in a lens.
To quantify the broadening of the point spread function, the Strehl-ratio [Jr et al., 2004][str]

$$S = \frac{|P_{real}(0,0)|^2}{|P_{ideal}(0,0)|^2} \tag{4.57}$$

can be used which compares the peak intensity of the aberrated point spread function $P_{real}(\nu_x, \nu_y) = \mathcal{F}[\Theta(D/2-r)e^{2\pi i W(x,y)}](\nu_x, \nu_y)$ to the unaberrated case $P_{ideal}(\nu_x, \nu_y) = \mathcal{F}[\Theta(D/2 - r)](\nu_x, \nu_y)$. Optics with $S > 0.8$ is said to be diffraction-limited. If the object to be Fourier-transformed is smaller than the lens' size a high-quality Fourier transform can be achieved if the lens is in fact diffraction limited. Then the finest details in the Fourier transform, set by the size of the object, can be fully resolved. In the case of much smaller objects this condition can be relaxed as we only require the illuminated part of the lens to be diffraction limited. Since aberrations usually grow with distance from the optical axis smaller apertures will generally speaking result in a higher Strehl-ratio. Based on the condition $S > 0.8$ we can define an effective lens diameter $D^* < D$, which will result in a larger effective size $\nu_p^* = 1/D^* > 1/D$ of the point spread function and hence also a lower frequency cutoff ν_c^*. If the full point spread function is known ν_p can of course be determined directly.
In practice aberrations are oftentimes also caused by non-perfect alignment of the lens with respect to other optical components. For example light beams that propagate through the lens under a 'mean' non-zero angle θ_0 with the optical axis typically experience coma. This angle-dependency indicates the limit of the thin-lens approximation. Luckily, the angular scale of such effects is usually much larger than the corresponding frequency spectrum of the object to be imaged or Fourier transformed. If that's the case we can include an angle or frequency dependency into the aberrations $W = W_{\theta_0}(x, y)$ and the point spread function $P = P_{\nu_0}(\nu_x, \nu_y)$, the pupil function $p = p_{\nu_0}(x, y)$, respectively. [14] It is reasonable to assume that ν_p grows with θ_0. Subsequently, the cutoff of the spatial frequencies in the object plane ν_c, but also the resolution in the Fourier plane will drop. By employing the same condition $S > 0.8$ we can also define a maximum angle θ_0 accepted by the lens.

[14] Note that this is stronger than simply shifting the pupil function by the mean angle as we did previously.

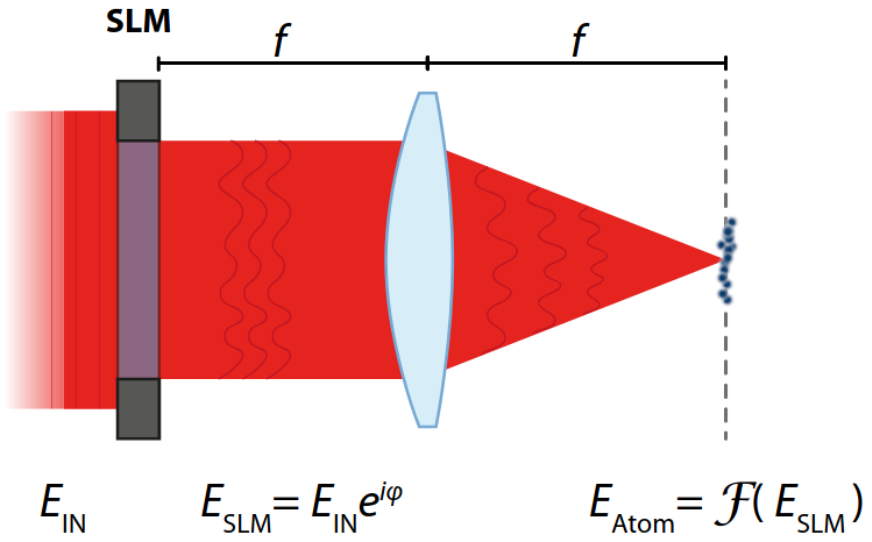

Figure 4.12: **Phase-only SLM**
A spatial light modulator is used to imprint a spatially varying phase $\phi(x, y)$ onto the incident beam. By a subsequent Fourier transform via a lens an almost arbitrary intensity distribution can be generated in focal plane of the lens. Taken from [Palm, 2018].

4.4.2 The Spatial Light Modulator

A powerful optical tool for the generation of arbitrary light fields is nowadays given in terms of spatial light modulators (SLM). The phase-only SLM we are going to use in this thesis can be pictured as a small mirror consisting of roughly half a million pixels. But these pixel do not only reflect the incident light. By adapting their refractive index also the phase of the reflected light can be manipulated. By subsequent Fourier transformation almost arbitrary light fields can be created in the focal plane of the used lens. This mechanism is illustrated in Fig. 4.12. Mathematically expressed, the SLM allows us to imprint a phase field $\phi(x, y)$ onto the reflected light field, i.e.

$$u_{out}(x, y) = e^{i\phi(x,y)} u_{in}(x, y). \tag{4.58}$$

More about the functional principle of the phase-only SLM and its characterization can be found in [Holten, 2014][Palm, 2018][Hammel, 2019].
Since the desired intensity distribution is not directly accessible, elaborated phase-retrieval algorithms are needed that at least approximate the phase $\phi(x, y)$ that yields the optimal intensity in the Fourier plane. Numerical and analytic approaches to this problem have been explored by Palm [2018] and Hammel [2019]. Both methods can be used to significantly enhance the harmonicity of the potentials we can generate using the SLM. Unfortunately, they are also rather complicated to implement and potentially time-consuming in their execution. So far, that means during the construction phase of the experiment, we have instead resorted to a much sim-

pler approach to generate the needed Gaussian and Laguerre-Gaussian potentials. We therefore want to quickly discuss the light fields generated in this way. Once the experiment is fully setup we can always optimize the trapping and perturbation potentials by the other methods.

Beam Generation

To generate a Laguerre-Gaussian beam we shine a collimated beam of laser light on the SLM. The incident laser beam has the profile of a LG_0^0-mode eq. (4.21) with waist W_0 and power P_0. Shortly behind the SLM the beam, perpendicular to its direction of propagation, has the modulated amplitude

$$u(r,\phi) = \sqrt{I_0}\Theta(R-r)e^{-r^2/W_0^2}e^{il\phi}, I_0 = \frac{2P_0}{\pi W_0^2} \tag{4.59}$$

where the phase $e^{il\phi}$ and the circular aperture were imprinted via the SLM. The latter is achieved by modulating a gradient within a disk of radius R onto incident beam. Such a phase pattern is shown in Fig. 4.13a for $l = 4$. The beam is then passed through a system of lenses which we simplify by a single lens of focal length f performing a Fourier transform of the beam. Assuming this lens to be ideal, the field at its focal plane is given by eq. (4.50) with $P(\nu_x,\nu_y) = \delta^{(2)}(\nu_x,\nu_y)$,

$$g(\boldsymbol{x}) = \frac{\sqrt{I_0}R}{2\pi r_0}e^{il\phi}F_l\left(r/r_0;\alpha\right), \quad F_l(\nu;\alpha) = \int_0^1 dy y e^{-\alpha y^2}\int_0^{2\pi} d\theta e^{il\theta}e^{iy\nu\cos(\theta)}, \tag{4.60}$$

where $\alpha = R^2/W_0^2$, the length scale $r_0 = \frac{\lambda f}{2\pi R}$ and (r,ϕ) now label the polar coordinates in the focal plane. Furthermore, any complex factors independent of l were omitted. The θ-integral can be rearranged slightly and then evaluates to $2\pi i^l J_l(\nu y)$, where J_l is the Bessel function. The remaining integral can be solved by expansion in powers of α and ν which leaves us with

$$F_l(\nu;\alpha) = 2\pi i^l\int_0^1 dy y e^{-\alpha y^2}J_l(\nu y) = 2\pi i^l\left(\frac{\nu}{2}\right)^l \underbrace{\sum_{m=0}^{\infty}\frac{(-1)^m a_{m,l}}{m!(m+l)!}\left(\frac{\nu}{2}\right)^{2m}}_{\equiv H_l(\nu;\alpha)}, \tag{4.61}$$

where the symbols $a_{m,l}(\alpha) = \sum_{n=0}^{\infty}\frac{(-\alpha)^n}{n!(2n+2m+l+2)}$ were defined. For our application we will always have $\alpha < 0.4$, thus only the first terms in $a_{m,l}(\alpha)$ are usually needed. Putting everything together we finally arrive at

$$g(r,\phi) = \frac{\sqrt{I_0}R}{r_0}i^l\left(\frac{r}{2r_0}\right)^l e^{il\phi}H_l(r/r_0;\alpha). \tag{4.62}$$

The function H_l behaves similar to an Airy-disk, in fact for $l = \alpha = 0$ it precisely reduces to this case, $H_0(\nu,0) \sim \frac{1}{\nu}J_1(\nu)$.

To connect to the Laguerre-Gaussian modes we compare the behavior of eq. (4.60)

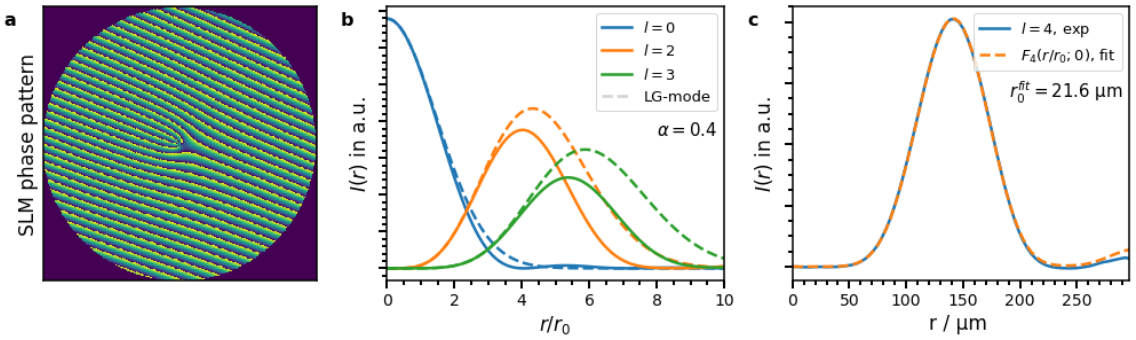

Figure 4.13: **Formation of higher-order Ary-disks**
a - Phase pattern on the SLM that leads to a formation of an approximate $l = 4$ Laguerre-Gauss mode in the Fourier plane of the SLM. **b** - The exact analytic solution eq. (4.60) for $l = 0, 2, 3$ and $\alpha = 0.4$ compared to the Laguerre-Gaussian approximation. **c** - Experimental measurement of the light field in the Fourier plane for the phase pattern (**a**) compared to a fit with eq. (4.60). The fit yields $r_0 = 21.6$ µm. The experimental 2D-data was warped to polar coordinates and then averaged over the angular degree of freedom. The data is taken for an aberration corrected lens.

with eq. (4.20) at small arguments. This yields

$$\begin{aligned} w_l &= 2r_0\sqrt{(l+1)\frac{a_{0,l}}{a_{1,l}}} = \frac{\lambda f}{\pi R}\sqrt{(l+1)\frac{a_{0,l}}{a_{1,l}}} \xrightarrow{\alpha\to 0} \frac{\lambda f}{\pi R}\sqrt{\frac{(l+4)(l+1)}{(l+2)}} \\ Q_l &= \frac{4P_0R^2}{W_0^2}\frac{a_{0,l}^2}{2^l l!}\left(\frac{a_{0,l}}{a_{1,l}}(l+1)\right)^{l+1} \\ &\xrightarrow{\alpha\to 0} \frac{4P_0R^2}{W_0^2}((l+2)^2 2^l l!)^{-1}\left(\frac{(l+4)(l+1)}{(l+2)}\right)^{l+1} \end{aligned} \quad , \tag{4.63}$$

where w_l is the waist and Q_l the power of the corresponding LG_0^l-mode in the focal plane. In the limit of small α we find $w_l/(\lambda f/R) = 0.45, 0.58, 0.66, 0.75$ and 0.82 (for $l = 0-4$), where the deviation for α up to 0.4 is on the order of 1%. In Fig. 4.13b the exact intensity profile for $\alpha = 0.4$ and $l = 0, 2, 3$ is compared to the Laguerre-Gaussian approximation. For small arguments a good agreement is achieved. For higher-l modes the deviations become significantly worse at larger arguments, where the Laguerre-Gaussians overestimate the exact higher-order Airy-type shape. Finally, the exact result eq. (4.61) is compared to an experimental observation of the intensity in the Fourier plane generated by a ($l = 4$)-vortex phase pattern with effective aperture radius of 160 px (i.e. 3.2 mm)[15]. The observation and a fit with eq. (4.61) is shown in Fig. 4.13c. The fit shows an excellent agreement and

[15]The actual aperture was only 80 px in radius, however the SLM plane was magnified by a 2:1 telescope

gives $r_0 = 21.6$ µm. For the 400 mm lens used, the expected value of r_0 computes to $r_0 = \lambda f/2\pi R \approx 19.9$ µm which is in good agreement with the fit result. Note that due to the small aperture on the SLM $\alpha \approx 0$ was used.

Higher Orders and other parasitic effects

The Hamamatsu 10468-03 SLM we are using consists of an array of 792 times 600 pixels spanning a total area of 15.8 times 12 mm, with a pixel pitch of 20 µm.[16] The phase per pixel can be specified with 8 bit resolution. Since the 2π-value, i.e. the number between 0 and 255 that corresponds to a phase of 2π, is typically less than 255, the phase-resolution is further lowered. The limited spatial and phase resolution will introduce some interesting effects that we shall study now.
Let d denote the pixel size and let there further be N_x and N_y pixels in x- and y-direction, respectively. We want to modulate the continuous phase pattern $\phi(x, y)$ onto the incident light field $u(x, y)$. Due to finite pixel size the actual phase pattern will be discretized instead and we get

$$u'(x,y) \approx \sum_{n,m} u(x_n, y_m) e^{i\phi(x_n,y_m)} h_d(x - x_n, y - y_m), \tag{4.64}$$

where the pixel coordinates are given by $x_n = d(n - (N_x - 1)/2)$, n runs from 0 to $N - 1$ (y-coordinate accordingly) and we assumed that the amplitude of the incident beam varies hardly over the scale of one pixel. Furthermore, $h_d(x, y) = \Theta\left(d - |x/2|\right)\Theta(d - |y/2|)$ is the envelope of a single pixel. This can be formally rewritten as

$$u'(x,y) = (q * h_d)(x,y) \tag{4.65}$$

with

$$q(x,y) = u(x,y)e^{i\phi(x,y)} \sum_{n,m} \delta^{(2)}(x - x_n, y - y_m). \tag{4.66}$$

The field in the focal plane is given by the Fourier transform which is straightforward to compute in this way,

$$U'(\nu_x, \nu_y) = (\underbrace{\mathcal{F}[u \cdot e^{i\phi}]}_{U'_0\nu_x,\nu_y)} * \mathrm{Px})(\nu_x, \nu_y) \cdot H_d(\nu_x, \nu_y). \tag{4.67}$$

H_d is the the Fourier transform of the pixel function which computes to [17]

$$H_d(\nu_x, \nu_y) = d^2 \mathrm{sinc}(d\nu_x)\mathrm{sinc}(d\nu_y), \tag{4.68}$$

[16] Distance between the centers of two neighboring pixels.
[17] $\mathrm{sinc}(x) = \sin(\pi x)/\pi x$

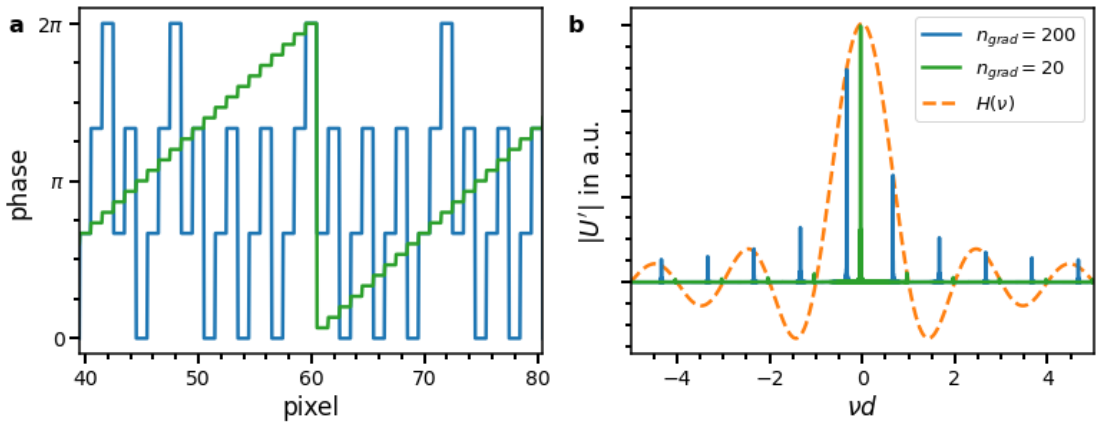

Figure 4.14: **SLM with phase gradient**
Phase on the SLM and corresponding amplitude in Fourier space for two different phase gradients. For clarity only one-dimension with 600 pixels is considered. **a** - Discretized phase value for a snippet of 20 pixels. **b** - Light amplitude in Fourier space. Besides the amplitude for both gradients also the envelope $H(\nu)$ is plotted. The bad resolution in the case of $n_{grad} = 200$ leads to stronger higher diffraction orders. For $n_{grad} = 0$ all higher orders would vanish identically as their position would coincide with the zeros of the envelope function.

and Px denotes the Fourier transform of the sum of the Dirac-deltas

$$\mathrm{Px}(\nu_x, \nu_y) = e^{-\pi i d\nu(N_x-1)} \sum_n^{N_x-1} e^{2\pi i d n \nu_x} \cdot (\leftrightarrow y) = \frac{\sin(\pi d N_x \nu_x)}{\sin(\pi d \nu_x)} \frac{\sin(\pi d N_y \nu_y)}{\sin(\pi d \nu_y)}. \quad (4.69)$$

Note that if we agree to take $u(x, y)$ to be zero outside of the SLM we can formally increase the number of pixels in eq. (4.66). This allows us to evaluate Px in the limit $N_x, N_y \to \infty$ which yields a Dirac comb,

$$\mathrm{Px}(\nu_x, \nu_y) \approx \frac{1}{d^2} \sum_{n,m=-\infty}^{\infty} \delta^{(2)}\left(\nu_x - \frac{n}{d}, \nu_y - \frac{m}{d}\right). \quad (4.70)$$

Putting everything together we see how the convolution of U_0' with Px creates an infinite amount of copies of U_0' placed on the grid $(n/d, m/d)$. However, successive multiplication with the envelope function $H_d(\nu_x, \nu_y)$ suppresses all frequencies beyond $\nu_x = \nu_y = 1/d$.

To illustrate this we take a look at a very simple phase pattern, the phase gradient

$$\phi(x, y) = \exp\left[2\pi i (n^x_{grad} x/dN_x + n^y_{grad} y/dN_y)\right]. \quad (4.71)$$

The gradient $\boldsymbol{g} = (n^x_{grad}/dN_x, n^y_{grad}/dN_y)$ means that the phase wraps n^x_{grad}-times around 2π over the full length of the SLM in x-direction. In Fourier space the

gradient will result in a peak at position $\boldsymbol{\nu} = -\boldsymbol{g}$, corresponding a physical displacement $\boldsymbol{x} = -\lambda f \boldsymbol{g}$ in the focal plane of of a lens with focal length f or an angle of propagation $\boldsymbol{\theta} = -\boldsymbol{g}/\lambda$ with respect to the direction of the reflected beam. In Fig. 4.14a the discretized phase pattern is depicted for two gradients with $n^y_{grad} = 20$ and $n^y_{grad} = 200$. For simplicity only one spatial dimension is considered. Since $N_y = 600$ the latter gradient is only very poorly resolved. The amplitude of the Fourier transformed field is shown in Fig. 4.14b where a constant illumination was assumed, i.e. $u(y) = h_{N_y d}(y)$. For the large gradient we observe comparatively strong higher diffraction orders at $d\nu = 1/3 + k, k \in \mathbb{Z}$, which stem from the poor spatial resolution of the phase pattern on the SLM. For smaller gradients these higher orders drop in power until for $n_{grad} = 0$ they vanish completely, since the location of the higher orders now coincides with the zeros of the envelope function H. This is to be expected since in our description the SLM is now completely structureless and hence no pixel effects should remain. On the contrary, the real SLM has only a filling factor of around 97 % which means that the pixel size is slightly smaller than the pixel pitch. In that sense we will always get higher diffraction orders (since the envelope becomes slightly larger while Px stays the same). More problematic however, is the '0-th order' peak, i.e. the light that is simply reflected by the space between the pixels of the non-ideal SLM. Due to its nature it cannot be manipulated and hence it has to be filtered out in a 4f-setup. For now let us already estimate the position of the higher orders in the focal plane. For a lens of $f = 100$ mm the first higher orders appear at ± 5.3 mm and hence can very easily be filtered out. For reasonable gradients, or spatial frequencies in general, we can therefore neglect Px and H and approximate

$$U'(\nu_x, \nu_y) \approx U'_0(\nu_x, \nu_y) = \mathcal{F}[u \cdot e^{i\phi}](\nu_x, \nu_y). \tag{4.72}$$

In practice higher orders can nevertheless be observed at lower frequencies, which have their origin in the 2π-value mentioned above. Let us again consider a a phase gradient $\boldsymbol{g} = (g, 0)$, however this time with a limited modulation depth $a \in [0, 1]$ corresponding to a 2π-value set too low. The corresponding phase pattern is given by

$$\phi(x, y) = 2\pi a(gx \mod 1), \tag{4.73}$$

i.e. the phase jumps to zero whenever a phase of $a2\pi$ is reached. We can then rewrite the light amplitude u' as

$$u'(x, y) = u(x, y) \sum_{n=-\infty}^{\infty} e^{2\pi i a g(x - \Delta n)} h_\Delta(x - n\Delta) \tag{4.74}$$

with $\Delta = 1/g$. This looks again like a pixel structure! Fourier transforming yields a convolution of $U(\nu_x, \nu_y)$ with the Fourier transform of the sum. The latter evaluates

to

$$\delta(\nu_y)H_\Delta(\nu_x+ag,0)\cdot\sum_{n=-\infty}^{\infty}e^{2\pi i n\nu_x/g}=g^2\delta(\nu_y)H_\Delta(\nu_x+ag,0)\sum_n\delta(\nu_x+ng). \quad (4.75)$$

Hence we will observe copies of U at positions $\nu_x=-ng, n\in\mathbb{Z}$, where their intensity is given by the envelope H_Δ,

$$I_n=\frac{\sin(\pi a)^2}{\pi^2(a-n)^2}. \quad (4.76)$$

For $a\approx 1$ the main peak is found for $n=1$ at $\nu_x=-g$ just as expected. However, if the 2π-value is not set correctly the spectrum becomes very spurious.

Generating multiple Beams

We can also use the SLM to generate multiple beams from one incident beam. Say we want to generate two beams with phase pattern $\phi_1(x,y)$ and $\phi_2(x,y)$, respectively. If we manipulate the incident beam with the pattern

$$\phi(x,y)=\arg\left(e^{i\phi_1(x,y)}+e^{i\phi_2(x,y)}\right) \quad (4.77)$$

the resulting modulated amplitude will look like

$$u_{out}(x,y)=\frac{1}{2}u_{in}(x,y)\frac{e^{i\phi_1(x,y)}+e^{i\phi_2(x,y)}}{1+\cos(\phi_1-\phi_2)}. \quad (4.78)$$

If we ignore the denominator for a moment we see how this will give rise to two distinct patterns in the Fourier plane, just what we wanted to achieve. But how is the oscillating denominator influencing this? Unfortunately, this question is not too easy to answer. Furthermore, as simulations and experimental observations show the approach works fine. However, we might nevertheless try to get at least a glimpse of what's going on. Let's assume both patterns to be separated well in the Fourier plane, i.e. both phase patterns are separated by a gradient $\Delta\boldsymbol{g}$. Since this gradient is the strongest fluctuation in the phase patterns, we will find poles in the denominator roughly every $\Delta\boldsymbol{x}=1/\boldsymbol{g}$, where the exact position of the poles is slightly shifted around for each pole due to the actual behavior of $\phi_1-\phi_2$. Between the poles the denominator will be of order one. Thus we again obtain something like a Dirac comb! Following the usual story we expect the presence of the denominator to reveal itself in the existence of higher diffraction orders in the Fourier plane separated by $\Delta\boldsymbol{g}$. This is indeed what one observes.

For our purpose we need two aligned modulated beams with a relative frequency detuning $\delta=\omega_L-\omega_L'$. To this end we simply shine two beams with the required relative detuning under an angle $\Delta\theta$ onto the SLM. Displaying the above phase pattern will consequently result in four outgoing beams. If we choose the relative

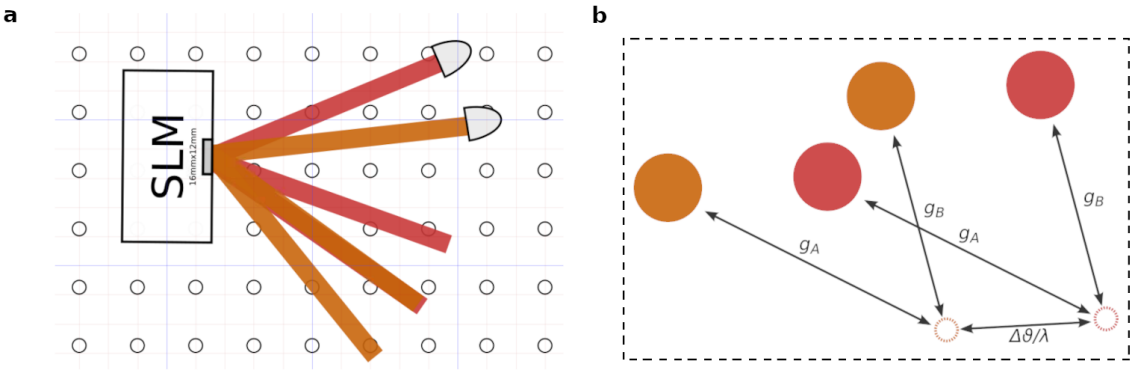

Figure 4.15: **Multiple beams**
a - Two laser beams (indicated by a slightly different color) are shone onto the SLM. Due the phase pattern on the SLM, two outgoing beams per incident beam are generated. Here the relative gradient between the outgoing beams is chosen such that two of the four beams are aligned. **b** - The corresponding image in the Fourier plane of the SLM, however this time none of the beams overlap. If $\Delta\boldsymbol{\theta}$ is the angle between the two incident beams then two beams overlap in the Fourier plane exactly when $\boldsymbol{g}_B - \boldsymbol{g}_A = \Delta\boldsymbol{\theta}/\lambda$. The dotted little circles indicate the position of the reflected beams if no phase pattern was modulated onto the incident beams via the SLM.

gradient between the phase patterns $\Delta\boldsymbol{g}$ to match the angle between the two incident beams, i.e. $\Delta\theta = \lambda\Delta\boldsymbol{g}$, two of the four outgoing beams will be aligned. This situation is sketched in Fig. 4.15. Fig. 4.15a shows a simplified version of the optical setup, where the slight color difference indicates the detuning of the beams. Here the relative gradient is chosen to precisely align two of the four beams. In Fig. 4.15b the corresponding image in the Fourier plane of the SLM is depicted, however here the alignment-condition is not met. After two beams are aligned the remaining two beams need to be filtered out with a pupil placed in the Fourier plane of the SLM. Note that the size of the angle between the incident beams limits the largest potentials that can be generated in this way, since at some point the different beams will overlap.

Canceling Aberrations

In section 4.4.1 we already discussed how in any realistic setting imperfections in the optical elements and alignment inevitably introduce aberrations leading to a broadening and distortion of the systems point spread function. Especially for our purposes of generating potentials for the ultracold lithium atoms, special care needs to be taken to carefully reduce the amount of aberrations present. Fortunately, the SLM provides us with a convenient way of mapping out and even canceling the aberrations in the optical setup. To this end recall eq. (4.56) that gives the field

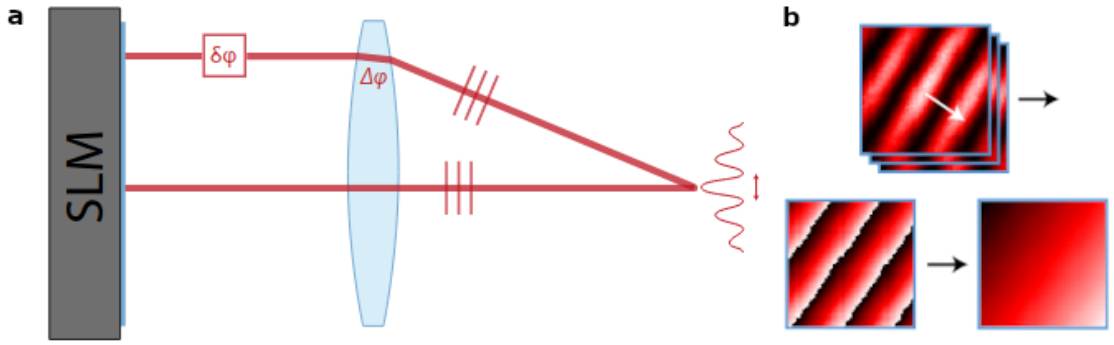

Figure 4.16: **Phase shift interferometry (PSI)**
a - Two spatially separated parallel beams interfere in the focal plane of the lens. Aberrations in the lens introduce a relative phase shift $\Delta\varphi$ between both beams shifting the maximum of the observed interference pattern. Moving one beam around the SLM allows to probe the phase shift at different sites of the lens. An additional phase shift $\delta\varphi$ is introduced via the SLM. **b** - Sweeping $\delta\varphi$ over 2π gives rise to a series of shifted patterns from which the phase map $\Delta\Phi$ of the original interference pattern can be extracted. Unwrapping the phase yields a continuous version for which a linear 2D-fit can be performed. Taken and adapted from [Palm, 2018].

$g(\boldsymbol{z})$ in the focal plane of a non-ideal lens with pupil function $p(x, y)$,

$$g(\boldsymbol{z}) = \mathcal{F}[u \cdot p](\boldsymbol{z}_f), \quad \boldsymbol{z}_f = \boldsymbol{z}/\lambda f \tag{4.79}$$

where we take $u(x, y)$ to be the field on the SLM. Let's assume we can write the pupil function as $p(x, y) = \Theta(D/2 - r)e^{2\pi i W(x,y)}$, where D is the lens diameter and W encodes the aberrations. If we further assume $W(x, y)$ to vary only slowly we might have the following idea. Let's make two small apertures with radius R and gradient $\boldsymbol{g}$ on the SLM located at different positions $\boldsymbol{x}_i$. This creates two beams that overlap in the Fourier plane. However, due to their displacement on the SLM they take different paths through the lens. In that sense they probe the pupil function at different sites from which they acquire an average phase shift $\Delta\varphi_i = 2\pi \langle W \rangle (\boldsymbol{x}_i)$. The resulting amplitude in the Fourier plane is given by

$$g(\boldsymbol{z}) \sim \sum_i \sqrt{I(\boldsymbol{x}_i)} e^{2\pi i \boldsymbol{z}_f \cdot \boldsymbol{x}_i + i\Delta\varphi_i} \mathrm{Ar}(\boldsymbol{z}_f R), \tag{4.80}$$

where $\mathrm{Ar}(\nu) = J_1(2\pi\nu)/\nu$ is the Airy-disk. When we measure the intensity we can observe the interference pattern,

$$I(\boldsymbol{z}) \sim \mathrm{Ar}^2(\boldsymbol{z}_f R) \left[I_1 + I_2 + 2\sqrt{I_1 I_2} \cos(2\pi \Delta\boldsymbol{x} \cdot \boldsymbol{z}_f + \Delta\varphi) \right], \tag{4.81}$$

where $\Delta\boldsymbol{x} = \boldsymbol{x}_2 - \boldsymbol{x}_1$, $\Delta\varphi = \varphi_2 - \varphi_1$ and $I_i = I(\boldsymbol{x}_i)$. This interference pattern is shown in Fig. 4.16b for a certain value of $\Delta\boldsymbol{x}$. In principle fitting the central region

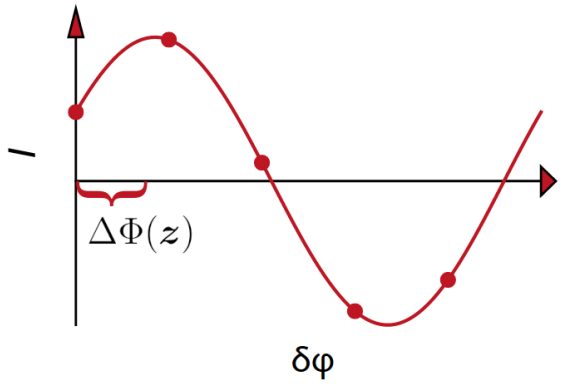

Figure 4.17: **PSI for one pixel**
A series of intensities is generated by adding a phase $\delta\varphi_n = 2\pi n/N$ to the probe beam. The phase offset $\Delta\Phi(\boldsymbol{z})$ can be deduced easily from the emerging cosine pattern. Here, $I_1 = I_2$ for simplicity. Taken and adapted from [Palm, 2018].

of the pattern allows one to deduce the phase shift $\Delta\varphi$. Note that the central lobe of the pattern will contain about $1 + |\Delta\boldsymbol{x}|/R$ stripes, so R should be chosen small enough to be able to resolve at least a few of the stripes. To map out the aberrations of the lens we fix the position of the first beam at the center of the SLM. By moving the second beam around we can probe the lens at different positions and retrieve an averaged version of the $W(x, y)$ up to a constant. This mechanism is sketched in Fig. 4.16a.

Performing a 2D-fit of the interference pattern is not the most reliable way of obtaining the phase shift $\Delta\varphi$. Fortunately, a refined version of the algorithm exists. By introducing an additional phase shift $\delta\varphi$ into the probe beam via the SLM we can alter the observed interference pattern. If we scan the phase according to $\delta\varphi = 2\pi n/N, n \in \{0, ..., N-1\}$,this results in a series of intensity patterns $I^{(n)}(\boldsymbol{z})$. Since the series ought to be periodic in n it can be decomposed into a Fourier series. As Schwider et al. [1983] show, this allows us to recover the total phase $\Delta\Phi(\boldsymbol{z}) = 2\pi\Delta\boldsymbol{x} \cdot \boldsymbol{z}_f + \Delta\varphi$ via

$$\tan(\Delta\Phi(\boldsymbol{z})) = \frac{\sum_n I^{(n)}(\boldsymbol{z}) \sin\delta\varphi_n}{\sum_n I^{(n)}(\boldsymbol{z}) \cos\delta\varphi_n}. \tag{4.82}$$

This procedure is illustrated in Fig. 4.17 for a single position $\boldsymbol{z}$. The injected phase shift $\delta\varphi_n$ leads to the emergence of a cosine-pattern precisely shifted by $\Delta\Phi(\boldsymbol{z})$. Intuitively speaking, $\Delta\Phi(\boldsymbol{z})$ can be deduced conveniently by locating the maximum of the cosine. Finally, we can unwrap the phase pattern $\Delta\Phi$ to obtain a continuous version of it. By fitting a gradient to the unwrapped phase we can deduce the remaining phase offset $\Delta\varphi$ as illustrated in Fig. 4.16b. The whole method goes by the name phase shift interferometry [Bruning et al., 1974] and allows us to measure aberrations down to 0.01λ [Schwider et al., 1983]. More details and a quantitative evaluation can be found in [Palm, 2018].
In order to cancel the lens aberrations we simply subtract the measured aberrations from the phase pattern we want to display. Note that the success of this method crucially relies on the same assumptions we used to arrive at eq. (4.56). Especially when we can no longer neglect the frequency dependent shift of the pupil function in eq. (4.53) the method will fail.

4.4.3 Optical Setup

In Fig. 4.18 the final setup built into the experiment is presented. Let us go through the setup step by step. We start with two laser beams that are each coupled out of a high power fiber. The 5-axis kinematic outcouplers are placed in the top right corner. The laser beams themselves are prepared on another smaller breadboard where they are generated by splitting a single laser beam into two. Furthermore placing two AOMs in the paths of these beams allows us to control their relative detuning. Hence, the two laser beams arriving at the main breadboard should be inherently phase stable, at least theoretically.[18] After they're coupled out of the fibers they diverge rapidly due to their small initial waist of 3.3 µm. Since we want to illuminate the 16x12 mm large SLM chip, we let the beams expand freely before we collimate both of them with the same one-inch 100 mm lens. This will yield a large Gaussian beam with a diameter of about 20 mm large enough to cover the SLM. To make the setup more compact we already place several optical elements in the optical path during the expansion of the beams. First of all the polarization of the light is cleaned with a 5 mm polarizing beam splitter. Directly afterwards a one centimeter 90:10 beam splitter is placed. The 10 % of the light reflected at this beam splitter is focused with a short one-inch 40 mm lens onto a fast photo-diode. This allows us to measure and stabilize the intensity of both beams separately, where the latter is achieved via the same AOMs used to create a detuning between the beams. The diverging light from both outcouplers is superimposed on a one-inch non-polarizing beam-splitter. Only then the light is collimated by the 100 mm lens. Behind the lens another one-inch beam splitter reflects the light onto the SLM. On the SLM the phase of the incident beams is modulated and the light is reflected backwards. This time 50 % of the light is transmitted through the cube down the breadboard. Note that a this point we have already lost almost 90 % of the light only due to the beam splitters. For circular apertures on the SLM at least another 40 % will be lost.

To remove the '0-th order' and all other higher orders stemming from the SLM we perform a Fourier transform with a one-inch 100 mm lens. In the lens' focal plane a pupil is placed that allows us to crop out the relevant part of the spectrum. Another one-inch 75 mm lens is placed accordingly to collimate the light beam again. Hence both lenses together form a telescope with demagnification of 0.75. Note that we don't really care about a perfect 4f-configuration here as we will perform a final Fourier transform when we send the light to the atoms anyway. Fig. 4.19 shows an image of the intensity in the focal plane of the 100 mm lens. Here the SLM is used to generate two beams with different gradient but same aperture by means of eq. (4.77). This result in two separated spots termed beam A and beam B in the Fourier plane. Since we shine two beams onto the SLM we expect four such spots in total. Here the gradient between beam A and beam B was chosen to exactly match the angle of the incident laser beams, thereby aligning two of the four spots int the Fourier plane. Beside this bright spot, the '0-th' orders of both incident beams can

[18] The optical fibers can be a source of phase instabilities.

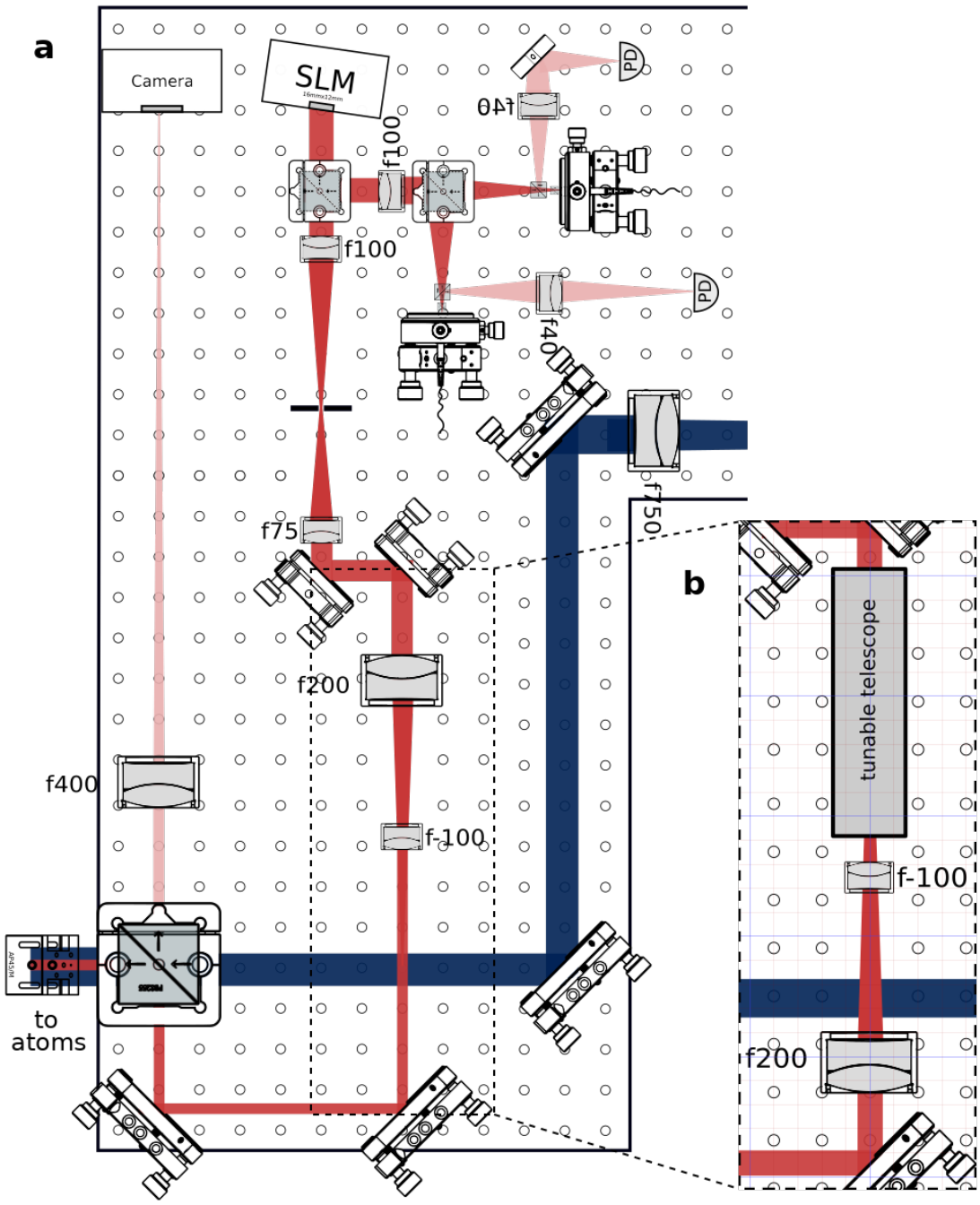

Figure 4.18: **Rotating-Trap Setup**
The beam path of the rotating trap setup is indicated in red, that of the microtrap in blue. The trapping and perturbation beam are collimated by the first 100 mm lens. Then both beams are send to the SLM where their wavefronts are modulated. They get reflected down the breadboard and filtering is performed with a pupil located in the focus of a 3:4 telescope. Finally, the beam is superimposed with the microtrap beam before it is send to the atoms via the high NA objective. **a** - Without, **b** - with tunable lens telescope and additional magnifying 2:1 telescope.

be seen. Furthermore, we also find a higher order and beam B of the first incident beam. In the present setup the alignment is achieved for a relative gradient of $\sim (n_x, n_y) = (60, 10)$, which allows large forth order vortex modes (100 px aperture radius + forth order phase vortex) to still be separated in the Fourier plane. This gradient corresponds to a relative angle of ~ 5 mrad between both beams.
After the filter telescope the laser beams are once again demagnified by a 1:2 telescope consisting of a 30 mm lens with a focal length of 200 mm and a one-inch -100 mm lens. Finally, the the light is superimposed with the microtrap beam (colored in blue) via a large 30 mm polarizing beam splitter. The reflected SLM-light and the transmitted microtrap beam are send down vertically where they are focused via the high-NA objective (not shown in Fig. 4.18) onto the trapped atoms. By rotating the polarization of the SLM light and the microtrap beam accordingly a small part will be transmitted through the 30 mm cube. This light is then focused with a large two-inch 400 mm lens onto a camera, where we choose the large focal length of 400 mm in order to minimize aberrations (lenses of smaller focal length usually bring in more aberrations). The image on the camera will tell us how the intensity in the plane of the atoms look like. This also allows us to access the aberrations introduced by the optical components in front of the 30 mm cube. Unfortunately, additional aberrations will be introduced by the high-NA objective and the window of the vacuum chamber.
In the scenerario just described (Fig. 4.18a), the strong microtrap is needed to initially trap the atoms. Only then the atoms are transferred into the much larger trap generated by the SLM. In the focal plane of the atoms the size of the SLM-trap can reach from a waist of about 4.3 µm (for the largest possible circular aperture of a radius of 300 pixel) up to 13 µm (100 px aperture radius). A different scenario is shown in Fig. 4.18b, where the 2:1 telescope is rotated by 180 degrees and a tunable lens telescope is inserted after the filter telescope. The tunable lens telescope is designed to achieve a variable demagnification of 1 to at least 0.2. This allows us to realize traps in the focal plane reaching from 1.1 µm up to 16.2 µm (for a 100 px aperture and a demagnification of the tunable lens telescope of 0.2) with the same setup. In this scenario the microtrap is not needed to load atoms into the SLM-trap. To achieve the aforementioned specifications the tunable lens telescope requires long optical paths on the order of meters. It is therefore build vertically. Due to the varying focal lengths of the tunable lenses it is not possible to realize a perfect 4f-setup with the telescope. Hence, the intensity behind the tunable telescope will be blurred heavily for most configurations due to defocus . Luckily, we are only interested in the intensity of the Fourier transform in the atom plane which isn't sensible to these kind of imaging errors. At the point of writing this thesis the tunable lens telescope is still under construction and hence the scenario depicted in Fig. 4.18a is implemented.

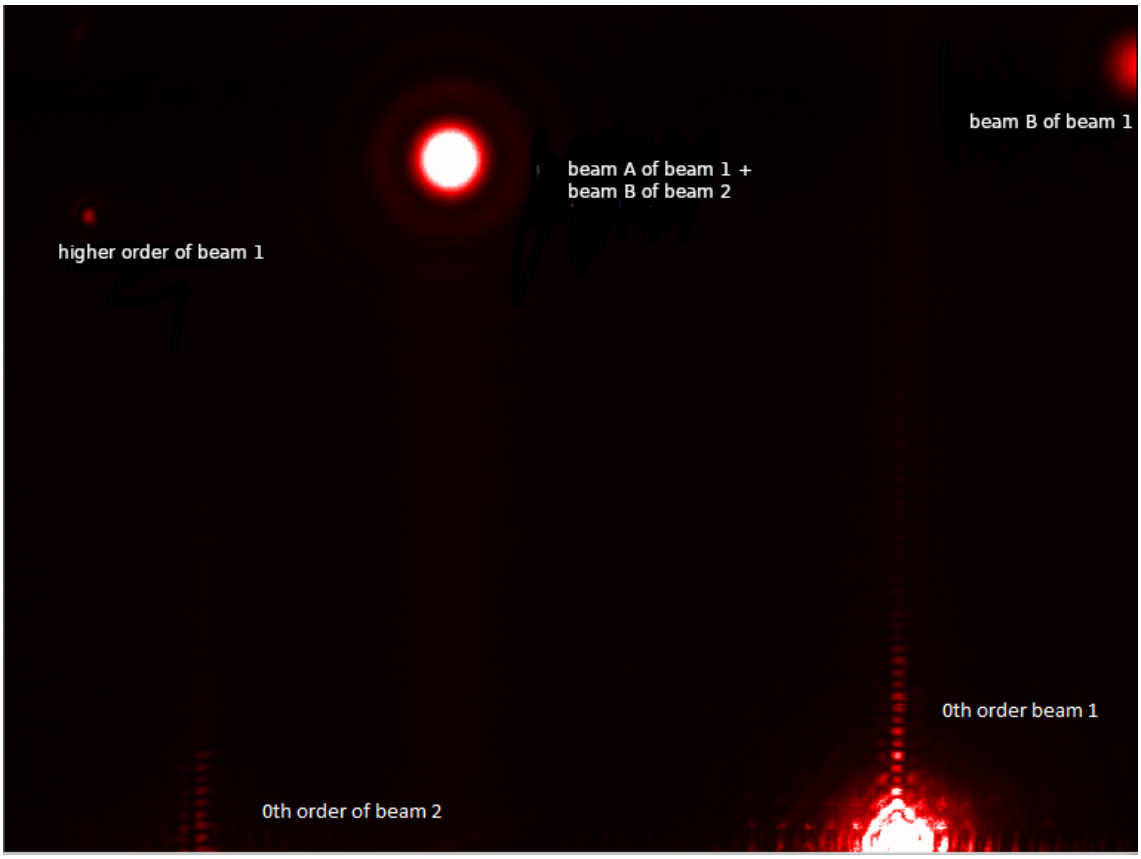

Figure 4.19: **Landscape in the Fourier plane**
Intensity in the focal plane of the filter telescope. The SLM modulates an aperture with two different gradients following eq. (4.77) onto the incident light, which leads to two beams (A and B) propagating under different angles with the optical axis. Since two beams are shone onto the SLM, we expect four outgoing beams. Here the gradients have been chosen such that two of these four beams are aligned. This results in a bright spot in the Fourier plane. Furthermore, one of the other two remaining generated beams, the '0-th orders' and additional higher orders can be observed. The relative angle between both incident beams is about 5 mrad.

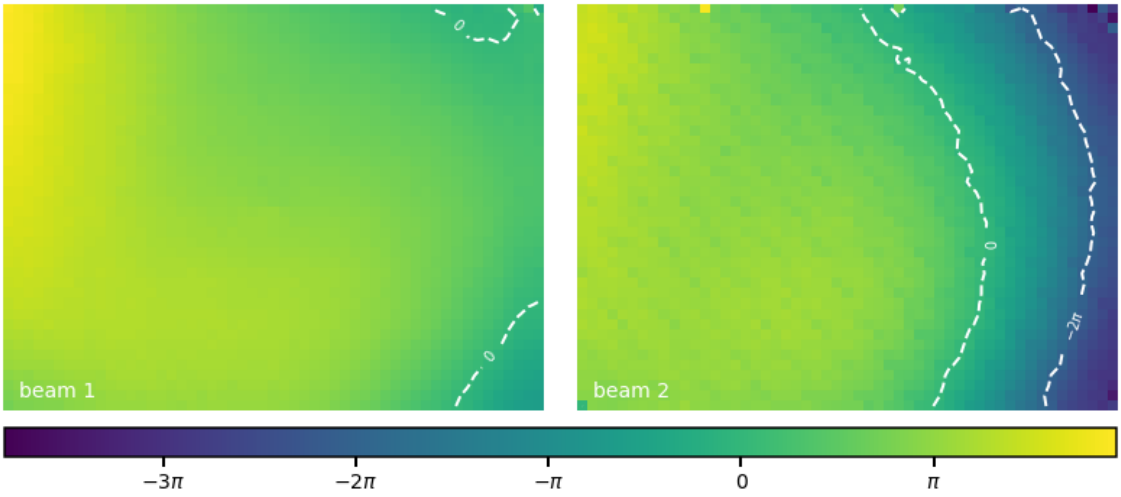

Figure 4.20: **Aberration map for both incident beams**
Aberration maps obtained via the PSI algorithm for both incident beams in the setup Fig. 4.18a.

Phase Errors and Measurements

In order to produce potentials of high quality we need to correct for the aberrations present in the optical setup. To this end we run the PSI algorithm introduced earlier. The resulting aberration maps are presented in Fig. 4.20, where one phase map per incident beam was recorded. While we only find weak aberrations for the first beam, they are significantly stronger for the second one. The reason for this lies in the simultaneous collimation of both beams with the first lens. In order to achieve a good collimation both outcouplers have to be placed in exactly the right distance from the lens. To minimize the amount of aberrations introduced by the lens both beams should pass through the lens in parallel with the optical axis. We furthermore want to illuminate the SLM as central as possible and especially we want to avoid a displacement between both beams on the SLM (which would eventually lead to a relative phase gradient in the Fourier plane distorting the rotating trap). Finally, we need a small angle between both beams in order to keep the different generated orders separable in the Fourier plane of the filter telescope. In turns out that these constraints are hard to meet simultaneously and hence the perfect collimation of beam 2 was sacrificed in favor of the other constraints. This is indeed a weakness of the compact setup. Nevertheless, also the aberrations on the second beam are sufficiently weak to correct for them via the SLM.

To demonstrate the effectiveness of the PSI algorithm several intensity patterns measured in the Fourier plane of the SLM are presented in Fig. 4.21. The measurements were taken for a single incident beam and a forth-order vortex and an aperture with gradient was displayed on the SLM. In Fig. 4.21e we see the intensity pattern if no correction is applied. The Laguerre Gauss mode is heavily distorted. Based on Fig. 4.11 the distortion hints at the presence of strong astigmatism in the

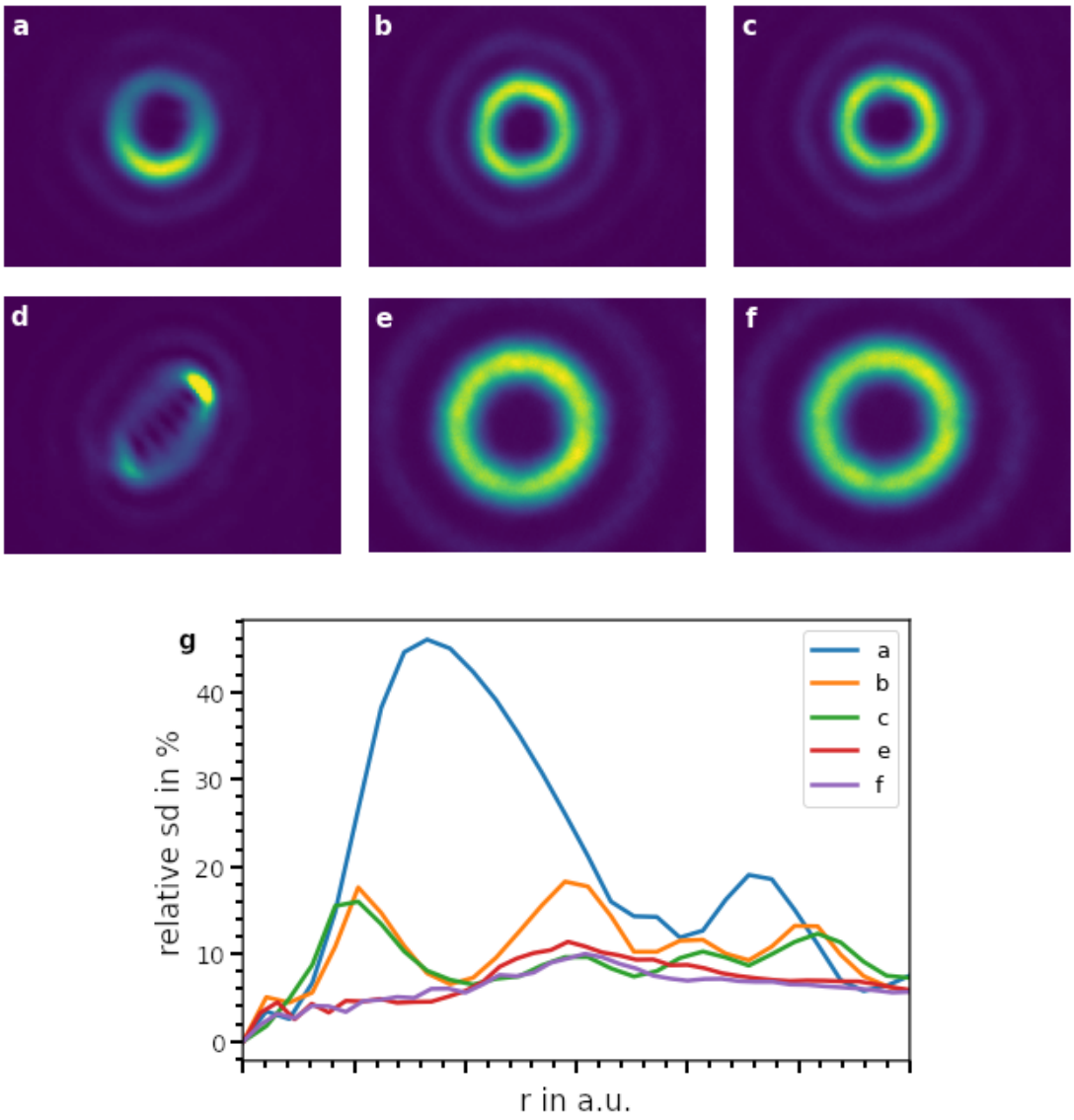

Figure 4.21: **Landscape in the Fourier plane**
Intensity in the Fourier plane of the SLM for a forth-order vortex and different aperture diameters. **a** - 600 px aperture with aberration correction, **b** - 600 px aperture with aberration correction and aligned with center of incident beam, **c** - 600 px aperture with second iteration of aberration correction and aligned with center of incident beam, **d** - 600 px aperture without any correction or alignment, **e** - 160 px aperture with aberration correction and aligned with center of incident beam, **f** - 160 px aperture with second iteration of aberration correction and aligned with center of incident beam. **g** - Intensity standard deviation over rings of different radii r around the center of the modes. The standard deviation is normalized with respect to the mean value in the corresponding ring, $\sqrt{\langle (I(r) - \langle I(r) \rangle)^2 \rangle} / \langle I(r) \rangle$, with $\langle I(r) \rangle = \int d\phi I(r, \phi)/2\pi$.

setup. The quality of the mode improves immediately when the aberration map is subtracted from the phase pattern displayed on the SLM, c.f. 4.21a. The rotational symmetry is again significantly improved when the center of the vortex is shifted to match the exact center of the incident Gaussian beam on the SLM (c.f. 4.21b). Performing another iteration of aberration correction improves the result only slightly (c.f. 4.21b). Fig. 4.21e,f shows the same setting with a smaller aperture of only 160 px. Since the light beam now illuminates a smaller part of the lenses in the optical setup in total less aberrations are acquired. This again significantly enhances the quality of the generated modes. For a more quantitative picture the relative standard deviation over a ring of radius r around the modes' centers is plotted in Fig. 4.21g. This tells us that despite the aberration correction there are still around 10 to 15 % of anisotropy left. On top of the aberrations stemming from the optical components on the breadboard additional aberrations will be introduced via the high-NA objective and the window of the vacuum chamber. How, or if at all these aberrations can be measured is yet an open question.

5 Conclusion and Outlook

In the first part of this thesis we discussed new numerical tools provided by the many-body code *Quanty*. While the taken numerical approach traces back to the 1950s and has long found its way into standard numerical libraries like ARPACK (and scipy), *Quanty* directly builds upon the formalism of second quantization making it especially attractive for the physics community. In that sense wavefunctions and operators can be conveniently specified in terms of creation and annihilation operators and the code handles antisymmetrization internally. During this thesis parts of the code, that originally runs in the scripting language Lua, were wrapped in python. The Lanczos-algorithm at the heart of *Quanty* tackles the problem of the exponential growth of the Hilbert space of multiple particles by generating a much smaller subspace on which the Hamiltonian will be diagonalized instead. Unfortunately, we found that the approach was still limited to a rather small number of at most 12 interacting particles in the harmonic trap. However, much of the problems can be attributed to the s-wave contact interaction that leads to a (deeply) bound molecular state. As this state is hard to express in terms of the used harmonic oscillator basis, a huge single particle basis is needed to accurately describe even just the physics of two atoms. Nevertheless, in a computation for the case of 6 interacting particles central features of the experimentally observed excitation spectrum could be reproduced.
To improve the numerical results optimization of the used single-particle basis is needed, especially when the numerical method should be extended to systems of larger particle number. One option to approach this would be to express a known solution of the two-particle problem on a huge basis spanned by the harmonic oscillator states $|i\rangle$, i.e. $|\psi_0\rangle \approx \sum_{ij} A_{ij} |i\rangle \otimes |j\rangle$. Then we seek a semi-unitary rotation R that rotates from the used harmonic oscillator basis to a smaller basis, $|\tilde{i}\rangle = R_{ij} |j\rangle$ while trying to keep the norm of $|\psi_0\rangle$ projected to the new basis as large as possible. Another way of improving the speed of the numerical computation for large particle numbers lays in the observation that the convergence of the Lanczos-method crucially depends on the overlap of the starting state with the ground state of the system. Hence the method could greatly benefit from starting with a more carefully chosen starting vector than just the non-interacting configuration. Such a starting vector could in the future for example be provided by the Richardson-model [von Delft, 2001].

In the second part we built upon the proposal by Palm [2018] and Palm et al. [2020] of an experimental scheme for the realization of fractional quantum Hall states in a system of few fermions in a rotating trap. While the original proposal studied

the case of a harmonic trap, it was quickly noted that the anharmonicity of experimentally realistic traps significantly impacts the physics in the lowest Landau level. This is mostly due to the lifted degeneracy in the LLL which competes with the interactions among the particles. This situation is similar to the original fraction quantum Hall effect where the Coloumb repulsion between the electrons has to compete with disorder in the sample. In order to observe the interesting quantum Hall state the energy shift ΔE_{an} introduced by the anharmonicity of the real trap needs to be small compared to the interaction energy $\Delta E_{int} \gg \Delta E_{an}$, at least up to some maximum angular momentum set by the state we are interested in. Furthermore, the states corresponding to the lowest and the first Landau level should also be well separated in energy, resulting in the weaker requirement, $\Delta E_{an}^{1LL} < 2\hbar\omega$. In a numerical simulation for 6 particles the ground state found in a Gaussian trap was compared to a target state, the Skyrmion-state occurring in the spin-singlet channel which was first identified by Palm et al. [2020] in the harmonic case. For traps deeper than $V_0 = 20\hbar\omega$ an overlap close to 100 % can be obtained for reasonable interaction strengths above $\eta = 0.1$. To prepare the Skyrmion state angular momentum is transferred by stirring the quantum droplet with a rotating elliptical perturbation. The corresponding adiabatic passage in a $20\hbar\omega$ deep Gaussian trap was simulated for $\eta = 0.25$ and a perturbation strength of $\epsilon_2 = 0.02$. In this scenario the Skyrmion state is reached at a speed of rotation of about $\Omega = 0.85\hbar\omega$. [1] Note that a larger interaction lets us reach the Skyrmion at lower speed of rotation, however this comes at cost of a smaller gab between the ground state and the first excited state. An upper bound for the perturbation is hard to define for the Gaussian trap since the lifted degeneracy results in a complicated level spectrum, even in the single-particle case. For now we resort to the harmonic case for which we can define a critical speed of rotation beyond which the overall potential becomes anti-confining in the presence of the perturbation. This yields $\Omega_c = 0.98$ in the present setting, however, this should be seen as only a crude upper bound and atoms might be lost from the trap at smaller speed. The smallest gap during the adiabatic passage was found to be $\Delta \sim 0.005\hbar\omega$ and occurs at $\Omega \sim 0.74\hbar\omega$. For an axial confinement of $\omega_z = 2\pi \cdot 30$ kHz and a radial trapping frequency of $\omega = 2\pi$ kHz the scenario just described is realized at a 3D-scattering length of $a_{3D} = 2800a_B$, where a_B is the Bohr-radius. If the trap and the perturbation are generated via Gaussian and Laguerre-Gaussian beams, a waist of $w_0 = 12$ µm and a power of 4 mW for the trapping and 13 µW for the perturbation beam is required. For this choice of the radial trapping frequency the minimal gab computes to $\Delta = 2\pi \cdot 5$ Hz, which poses a lower bound of ~ 200 ms for the minimal time with which the passage can be executed.
Besides the numerical study of the realistic trap also an optical setup was build in our ^{6}Li-experiment, which will be used to generate the needed trap and rotating perturbations by employing a spatial light modulator. To achieve potentials of high rotational symmetry in the atom plane it is crucial to cancel aberrations present in the setup. This can be conveniently done with the SLM as well, however some

[1] The elliptical perturbation is then physically rotating with speed $2\Omega = 1.9\hbar\omega$.

kind of image feedback is needed. Since so far no atoms could be loaded into the SLM-trap it still remains an open question whether or not the additional aberrations introduced by optical elements located between the optical setup and the final plane of the atoms can be canceled or how badly the quality of the final potentials is influenced.

A Additional Figures

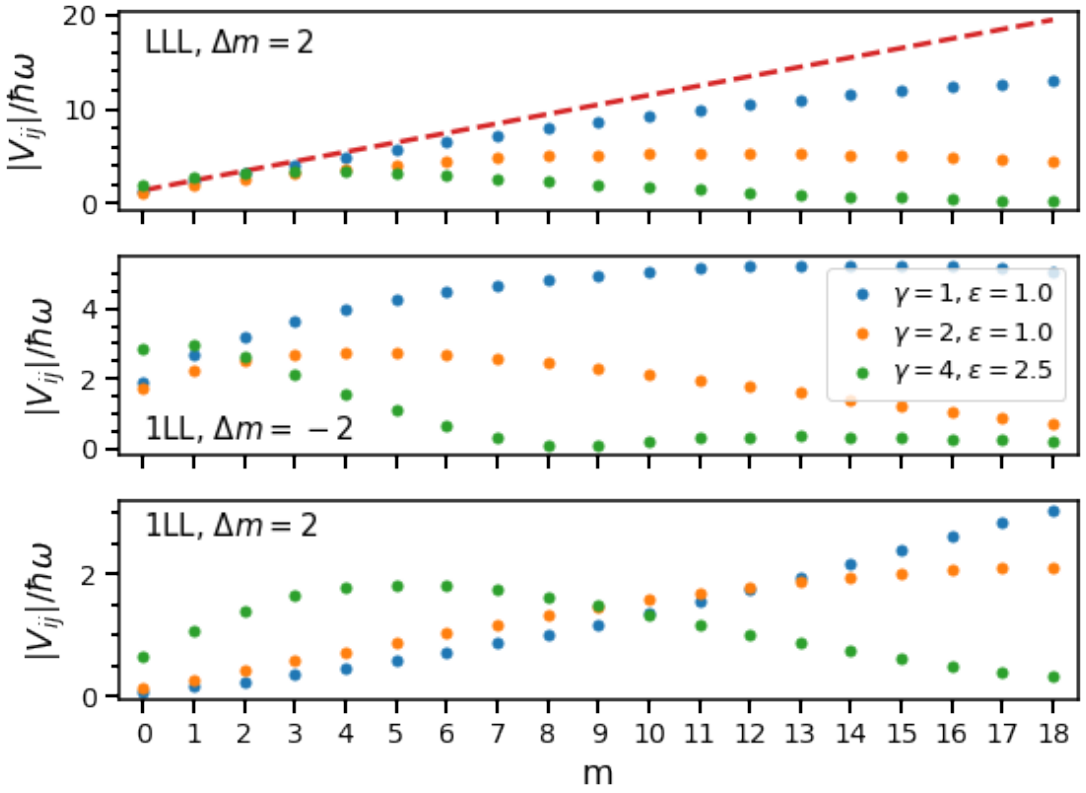

Figure A.1: **Matrix elements of the elliptic perturbation**
First row $\epsilon_{LLL} \langle m+2|V_2|m\rangle_{LLL}$, second row $\epsilon_{1LL} \langle m-2|V_2|m\rangle_{LLL}$, third row $\epsilon_{1LL} \langle m+2|V_2|m\rangle_{LLL}$, for different ratios of trap to perturbation waist $\gamma = w_0'/w_0$. The perturbation V_2 is given by eq. (4.31). Computed for a trap depth $V_0 = 20\hbar\omega$. The dashed red line represents the harmonic case. Adapting γ allows one to engineer a perturbation that is suppressed at higher angular momenta.

B Bibliography

Passfehler asphärischer linsen und strehl-verhältnis. https://www.edmundoptics.de/knowledge-center/application-notes/lasers/aspheric-lens-irregularity-and-strehl-ratio/. Accessed: 2021-10-05.

Nilab Abbas. Raman transitions with a phase locked laser system. Master's thesis, Universität Heidelberg, 2021.

S K Adhikari. Quantum scattering in two dimensions. *Am. J. Phys.; (United States)*, 54:4, 4 1986. doi: 10.1119/1.14623. URL https://www.osti.gov/biblio/6093823.

Jeeva S. Anandan and Jun Suzuki. Quantum mechanics in a rotating frame. *arXiv: Quantum Physics*, pages 361–370, 2003.

M. H. Anderson, J. R. Ensher, M. R. Matthews, C. E. Wieman, and E. A. Cornell. Observation of bose-einstein condensation in a dilute atomic vapor. *Science*, 269 (5221):198–201, 1995. doi: 10.1126/science.269.5221.198. URL https://www.science.org/doi/abs/10.1126/science.269.5221.198.

Malvin Carl Teich Bahaa E. A. Saleh. *Fourier Optics*, chapter 4, pages 108–156. John Wiley & Sons, Ltd, 1991. ISBN 9780471213741. doi: https://doi.org/10.1002/0471213748.ch4. URL https://onlinelibrary.wiley.com/doi/abs/10.1002/0471213748.ch4.

M. Bartelmann, B. Feuerbacher, T. Krüger, D. Lüst, A. Rebhan, and A. Wipf. *Theoretische Physik*. Springer Berlin Heidelberg, 2014. ISBN 9783642546181. URL https://books.google.de/books?id=YJE9BQAAQBAJ.

Luca Bayha, Marvin Holten, Ralf Klemt, Keerthan Subramanian, Johannes Bjerlin, Stephanie Reimann, Georg Bruun, Philipp Preiss, and Selim Jochim. Observing the emergence of a quantum phase transition shell by shell. *Nature*, 587:583–587, 11 2020. doi: 10.1038/s41586-020-2936-y.

Andrea Bergschneider, Vincent M. Klinkhamer, Jan Hendrik Becher, Ralf Klemt, Gerhard Zürn, Philipp M. Preiss, and Selim Jochim. Spin-resolved single-atom imaging of ^{6}Li in free space. *Phys. Rev. A*, 97:063613, Jun 2018. doi: 10.1103/PhysRevA.97.063613. URL https://link.aps.org/doi/10.1103/PhysRevA.97.063613.

H. Bethe and R. Peierls. Quantum Theory of the Diplon. *Proceedings of the Royal Society of London Series A*, 148(863):146–156, January 1935. doi: 10.1098/rspa.1935.0010.

J. H. Bruning, D. R. Herriott, J. E. Gallagher, D. P. Rosenfeld, A. D. White, and D. J. Brangaccio. Digital wavefront measuring interferometer for testing optical surfaces and lenses. *Appl. Opt.*, 13(11):2693–2703, Nov 1974. doi: 10.1364/AO.13.002693. URL http://www.osapublishing.org/ao/abstract.cfm?URI=ao-13-11-2693.

Thomas Busch, Berthold-Georg Englert, Kazimierz Rzazewski, and Martin Wilkens. Two cold atoms in a harmonic trap. *Foundations of Physics*, 28, 04 1998. doi: 10.1023/A:1018705520999.

Cheng Chin, Rudolf Grimm, Paul Julienne, and Eite Tiesinga. Feshbach resonances in ultracold gases. *Rev. Mod. Phys.*, 82:1225–1286, Apr 2010. doi: 10.1103/RevModPhys.82.1225. URL https://link.aps.org/doi/10.1103/RevModPhys.82.1225.

K. B. Davis, M. O. Mewes, M. R. Andrews, N. J. van Druten, D. S. Durfee, D. M. Kurn, and W. Ketterle. Bose-einstein condensation in a gas of sodium atoms. *Phys. Rev. Lett.*, 75:3969–3973, Nov 1995. doi: 10.1103/PhysRevLett.75.3969. URL https://link.aps.org/doi/10.1103/PhysRevLett.75.3969.

B. DeMarco and D. S. Jin. Onset of fermi degeneracy in a trapped atomic gas. *Science*, 285(5434):1703–1706, 1999. doi: 10.1126/science.285.5434.1703. URL https://www.science.org/doi/abs/10.1126/science.285.5434.1703.

Richard J. Fletcher, Airlia Shaffer, Cedric C. Wilson, Parth B. Patel, Zhenjie Yan, Valentin Crépel, Biswaroop Mukherjee, and Martin W. Zwierlein. Geometric squeezing into the lowest landau level. *Science*, 372(6548):1318–1322, Jun 2021. ISSN 1095-9203. doi: 10.1126/science.aba7202. URL http://dx.doi.org/10.1126/science.aba7202.

Mariusz Gajda, Jan Mostowski, Tomasz Sowiński, and Magdalena Załuska-Kotur. Single-shot imaging of trapped fermi gas. *EPL (Europhysics Letters)*, 115(2):20012, jul 2016. doi: 10.1209/0295-5075/115/20012. URL https://doi.org/10.1209/0295-5075/115/20012.

Nathan Gemelke, Edina Sarajlic, and Steven Chu. Rotating few-body atomic systems in the fractional quantum hall regime. 07 2010.

Stefano Giorgini, Lev P. Pitaevskii, and Sandro Stringari. Theory of ultracold atomic fermi gases. *Rev. Mod. Phys.*, 80:1215–1274, Oct 2008. doi: 10.1103/RevModPhys.80.1215. URL https://link.aps.org/doi/10.1103/RevModPhys.80.1215.

Rudolf Grimm, Matthias Weidemüller, and Yurii B. Ovchinnikov. Optical dipole traps for neutral atoms. 42:95–170, 2000. ISSN 1049-250X. doi: https://doi.org/10.1016/S1049-250X(08)60186-X. URL https://www.sciencedirect.com/science/article/pii/S1049250X0860186X.

B. I. Halperin. Theory of the quantized Hall conductance. *Helv. Phys. Acta*, 56: 75–102, 1983.

Tobias Hammel. Analytical approach to holography for robust trapping of ultracold atoms. Master's thesis, Universität Heidelberg, 2019.

M. W. Haverkort, M. Zwierzycki, and O. K. Andersen. Multiplet ligand-field theory using wannier orbitals. *Phys. Rev. B*, 85:165113, Apr 2012. doi: 10.1103/PhysRevB.85.165113. URL https://link.aps.org/doi/10.1103/PhysRevB.85.165113.

Ruth Heine. *Digital In-Line X-Ray Holographic Microscopy with Synchrotron Radiation*. PhD thesis, 01 2008.

Marvin Holten. Hamiltonian engineering in ultracold atom experi- ments using a spatial light modulator. Master's thesis, Universität Heidelberg, 2014.

Marvin Holten, Luca Bayha, Keerthan Subramanian, Sandra Brandstetter, Carl Heintze, Philipp Lunt, Philipp M. Preiss, and Selim Jochim. Observation of cooper pairs in a mesoscopic 2d fermi gas, 2021a.

Marvin Holten, Luca Bayha, Keerthan Subramanian, Carl Heintze, Philipp M. Preiss, and Selim Jochim. Observation of pauli crystals. *Phys. Rev. Lett.*, 126:020401, Jan 2021b. doi: 10.1103/PhysRevLett.126.020401. URL https://link.aps.org/doi/10.1103/PhysRevLett.126.020401.

Zbigniew Idziaszek and Tommaso Calarco. Analytical solutions for the dynamics of two trapped interacting ultracold atoms. *Phys. Rev. A*, 74:022712, Aug 2006. doi: 10.1103/PhysRevA.74.022712. URL https://link.aps.org/doi/10.1103/PhysRevA.74.022712.

C.J. Joachain. *Quantum Collision Theory*. North-Holland, 1975. ISBN 9780720402940. URL https://books.google.de/books?id=Zs3vAAAAMAAJ.

Lewis Jr, Marshall Perrin, Franck Marchis, Anand Sivaramakrishnan, Russell Makidon, Julian Christou, Bruce Macintosh, Lisa Poyneer, Marcos van Dam, and Mitchell Troy. Is that really your strehl ratio? *Advancements in Adaptive Optics*, 5490, 10 2004. doi: 10.1117/12.549115.

W. Ketterle and M. W. Zwierlein. Making, probing and understanding ultracold Fermi gases. *Nuovo Cimento Rivista Serie*, 31(5-6):247–422, May 2008. doi: 10.1393/ncr/i2008-10033-1.

Ralf A. Klemt. *Correlations from Microscopic to Macroscopic Quantum Systems: Interactions vs Indistinguishability*. PhD thesis, Universität Heidelberg, 2021.

K. v. Klitzing, G. Dorda, and M. Pepper. New method for high-accuracy determination of the fine-structure constant based on quantized hall resistance. *Phys. Rev. Lett.*, 45:494–497, Aug 1980. doi: 10.1103/PhysRevLett.45.494. URL https://link.aps.org/doi/10.1103/PhysRevLett.45.494.

R. B. Laughlin. Anomalous quantum hall effect: An incompressible quantum fluid with fractionally charged excitations. *Phys. Rev. Lett.*, 50:1395–1398, May 1983. doi: 10.1103/PhysRevLett.50.1395. URL https://link.aps.org/doi/10.1103/PhysRevLett.50.1395.

A. J. Leggett. Diatomic molecules and cooper pairs. In Andrzej Pękalski and Jerzy A. Przystawa, editors, *Modern Trends in the Theory of Condensed Matter*, pages 13–27, Berlin, Heidelberg, 1980. Springer Berlin Heidelberg. ISBN 978-3-540-38628-5.

Philippe Nozières and Stephan Schmitt-Rink. Bose condensation in an attractive fermion gas: From weak to strong coupling superconductivity. *Journal of Low Temperature Physics*, 59:195–211, 1985.

L Palm, F Grusdt, and P M Preiss. Skyrmion ground states of rapidly rotating few-fermion systems. *New Journal of Physics*, 22(8):083037, aug 2020. doi: 10.1088/1367-2630/aba30e. URL https://doi.org/10.1088/1367-2630/aba30e.

Lukas Palm. Exploring fractional quantum hall physics using ultracold fermions in rotating traps. Master's thesis, Universität Heidelberg, 2018.

Ram-Janik Petzold. A two-dimensional optical dipole trap for a system of few ultracold fermions. Master's thesis, Universität Heidelberg, 2016.

M. Popp, B. Paredes, and J. I. Cirac. Adiabatic path to fractional quantum hall states of a few bosonic atoms. *Phys. Rev. A*, 70:053612, Nov 2004. doi: 10.1103/PhysRevA.70.053612. URL https://link.aps.org/doi/10.1103/PhysRevA.70.053612.

Mohit Randeria, Ji-Min Duan, and Lih-Yir Shieh. Superconductivity in a two-dimensional fermi gas: Evolution from cooper pairing to bose condensation. *Phys. Rev. B*, 41:327–343, Jan 1990. doi: 10.1103/PhysRevB.41.327. URL https://link.aps.org/doi/10.1103/PhysRevB.41.327.

Nicholas Read and N. Cooper. Free expansion of lowest-landau-level states of trapped atoms: A wave-function microscope. *Physical Review A*, 68:035601, 2003.

C. A. Regal, M. Greiner, and D. S. Jin. Observation of resonance condensation of fermionic atom pairs. *Phys. Rev. Lett.*, 92:040403, Jan 2004. doi:

10.1103/PhysRevLett.92.040403. URL https://link.aps.org/doi/10.1103/PhysRevLett.92.040403.

V. Schweikhard, I. Coddington, P. Engels, V. P. Mogendorff, and E. A. Cornell. Rapidly rotating bose-einstein condensates in and near the lowest landau level. *Phys. Rev. Lett.*, 92:040404, Jan 2004. doi: 10.1103/PhysRevLett.92.040404. URL https://link.aps.org/doi/10.1103/PhysRevLett.92.040404.

J. Schwider, R. Burow, K.-E. Elssner, J. Grzanna, R. Spolaczyk, and K. Merkel. Digital wave-front measuring interferometry: some systematic error sources. *Appl. Opt.*, 22(21):3421–3432, Nov 1983. doi: 10.1364/AO.22.003421. URL http://www.osapublishing.org/ao/abstract.cfm?URI=ao-22-21-3421.

Friedhelm Serwane, G Zürn, T Lompe, T Ottenstein, Andre Wenz, and S Jochim. Deterministic preparation of a tunable few-fermion system. *Science (New York, N.Y.)*, 332:336–8, 04 2011. doi: 10.1126/science.1201351.

H.M. Srivastava, H.A. Mavromatis, and R.S. Alassar. Remarks on some associated laguerre integral results. *Applied Mathematics Letters*, 16(7):1131–1136, 2003. ISSN 0893-9659. doi: https://doi.org/10.1016/S0893-9659(03)90106-6. URL https://www.sciencedirect.com/science/article/pii/S0893965903901066.

David Tong. Lectures on the quantum hall effect, 2016.

Jan von Delft. Review: Superconductivity in ultrasmall metallic grains. *arXiv: Mesoscale and Nanoscale Physics*, 2001.

Steven Weinberg. *The Quantum theory of fields. Vol. 1: Foundations*. Cambridge University Press, 6 2005. ISBN 978-0-521-67053-1, 978-0-511-25204-4.

T. M. Whitehead, L. M. Schonenberg, N. Kongsuwan, R. J. Needs, and G. J. Conduit. Pseudopotential for the two-dimensional contact interaction. *Phys. Rev. A*, 93:042702, Apr 2016. doi: 10.1103/PhysRevA.93.042702. URL https://link.aps.org/doi/10.1103/PhysRevA.93.042702.

R. Willett, J. P. Eisenstein, H. L. Störmer, D. C. Tsui, A. C. Gossard, and J. H. English. Observation of an even-denominator quantum number in the fractional quantum hall effect. *Phys. Rev. Lett.*, 59:1776–1779, Oct 1987. doi: 10.1103/PhysRevLett.59.1776. URL https://link.aps.org/doi/10.1103/PhysRevLett.59.1776.

Daijiro Yoshioka. Wave function of the largest skyrmion on a sphere. *Journal of the Physical Society of Japan*, 67(10):3356–3359, 1998. doi: 10.1143/JPSJ.67.3356. URL https://doi.org/10.1143/JPSJ.67.3356.

M Zwierlein, J Abo-Shaeer, A Schirotzek, Christian Schunck, and W Ketterle. Vortices and superfluidity in a strongly interacting fermi gas. *Nature*, 435:1047–51, 07 2005. doi: 10.1038/nature03858.

M. W. Zwierlein, C. A. Stan, C. H. Schunck, S. M. F. Raupach, A. J. Kerman, and W. Ketterle. Condensation of pairs of fermionic atoms near a feshbach resonance. *Phys. Rev. Lett.*, 92:120403, Mar 2004. doi: 10.1103/PhysRevLett.92.120403. URL https://link.aps.org/doi/10.1103/PhysRevLett.92.120403.

Erklärung:

Ich versichere, dass ich diese Arbeit selbstständig verfasst habe und keine anderen als die angegebenen Quellen und Hilfsmittel benutzt habe.

Heidelberg, den (Datum) .....